INFORMATION TO USERS

This manuscript has been reproduced from the microfilm master. UMI films the text directly from the original or copy submitted. Thus, some thesis and dissertation copies are in typewriter face, while others may be from any type of computer printer.

The quality of this reproduction is dependent upon the quality of the copy submitted. Broken or indistinct print, colored or poor quality illustrations and photographs, print bleedthrough, substandard margins, and improper alignment can adversely affect reproduction.

In the unlikely event that the author did not send UMI a complete manuscript and there are missing pages, these will be noted. Also, if unauthorized copyright material had to be removed, a note will indicate the deletion.

Oversize materials (e.g., maps, drawings, charts) are reproduced by sectioning the original, beginning at the upper left-hand corner and continuing from left to right in equal sections with small overlaps. Each original is also photographed in one exposure and is included in reduced form at the back of the book.

Photographs included in the original manuscript have been reproduced xerographically in this copy. Higher quality 6" x 9" black and white photographic prints are available for any photographs or illustrations appearing in this copy for an additional charge. Contact UMI directly to order.

UMI

WAVELENGTH TUNABLE MICROMECHANICAL

VERTICAL CAVITY SURFACE EMITTING LASERS

A DISSERTATION

SUBMITTED TO THE DEPARTMENT OF ELECTRICAL ENGINEERING

AND THE COMMITTEE ON GRADUATE STUDIES

OF STANFORD UNIVERSITY

IN PARTIAL FULFILLMENT OF THE REQUIREMENTS

FOR THE DEGREE OF

DOCTOR OF PHILOSOPHY

Melissa Y. Li

MARCH 1999

UMI Number: 9924582

Copyright 1999 by
Li, Melissa Yan-Yee

UMI Microform 9924582
Copyright 1999, by UMI Company. All rights reserved.

UMI

300 North Zeeb Road
Ann Arbor, MI 48103

ii

I certify that I have read this dissertation and that in my opinion it is fully adequate, in scope and quality, as a dissertation for the degree of Doctor of Philosophy.

Professor Connie Chang-Hasnain,
Principal Adviser

I certify that I have read this dissertation and that in my opinion it is fully adequate, in scope and quality, as a dissertation for the degree of Doctor of Philosophy.
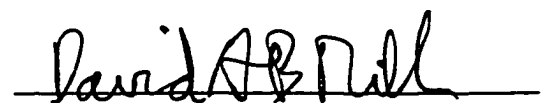
Professor Anthony Siegman,
Associate Adviser

I certify that I have read this dissertation and that in my opinion it is fully adequate, in scope and quality, as a dissertation for the degree of Doctor of Philosophy.

Professor Thomas Lee

I certify that I have read this dissertation and that in my opinion it is fully adequate, in scope and quality, as a dissertation for the degree of Doctor of Philosophy.

Professor David A.B. Miller

Approved for the University Committee on Graduate Studies:

iii

Abstract

There is a true need today for a compact, inexpensive, reliable, and simple-to-use tunable laser for applications ranging from wavelength-division multiplexed optical transmission to spectroscopy. The micromechanical tunable vertical cavity surface emitting laser (VCSEL) is a well suited candidate for these applications.

This thesis discusses the design, fabrication, performance, and analyses of a micromechanical wavelength tunable VCSEL with one mirror in the shape of a cantilever. Tuning is achieved electrostatically through the actuation of the cantilever by reverse-biasing a pn-junction. The wavelength-dependent properties of the tunable VCSEL are presented in examples and comparison studies. Across the tuning range, the modal gain confinement factor in the longitudinal direction can vary by at least a factor of three. In addition, the use of only one dielectric mirror in the tunable VCSEL structure is found to provide little advantage in enhancing the tuning range. Furthermore, this tuning range is limited by a one-third rule, which is explained in this thesis. Device fabrication details are given and summarized.

The first monolithic top-emitting tunable VCSEL demonstrates 20nm of continuous tuning with sub-milliamp threshold and peak powers in excess of 1mW across most of the tuning range. A record tuning range of 31.6nm has also been achieved with another device. Active wavelength stability to within one nanometer is

demonstrated over a change of 35°C. Due to the temperature-insensitivity of the refractive index in the air gap, the rate of wavelength change with temperature in a tunable VCSEL can be substantially smaller than that in a regular VCSEL.

Electromechanical and optical analyses on this tunable VCSEL are performed. Three electrostatic tuning models and their results are shown. Inclusion of the fringing fields in the cantilever geometry is found to provide only a 4% correction to the results that neglect those field lines in the analysis. Optical modal analysis in the tunable VCSEL serves to address the cost for wavelength tunability. Moreover, tilt and diffraction losses inherent to our VCSEL are quantified. In the smaller devices, diffraction loss through the air gap dominates optical loss while tilt loss is the culprit in a larger device. Good agreement between our analyses and experimental data is achieved and presented.

v

Acknowledgements

This thesis would not come into being if it weren't for the many people whose encouragement, friendship, and love has sustained me throughout my graduate journey. To them I am forever indebted:

My advisor, Professor Connie Chang-Hasnain, for her enthusiasm, dedication, energy, insights, lessons, and example;

Past and present fellow research "groupies" from Stanford and Berkeley: Chih-Hao Chang, Steve Chase, Lukas Chrostowski, Dan Francis, Giorgio Giaretta, Jacob Hernandez, P.C. Ku, Kevin Lascola, Rashit Nabiev, Yae Okuno, Robert Stone, Jeff Waite, Marianne Wu, and Yongan Wu for the comradeship. Special thanks go to Gabriel Li, Sui Lim, and Wupen Yuen for their fraternity and many hours of laughs; and Ed Vail, for his candor and advice;

Dr. Dubravko Babic, whose acquaintance I have been privileged to make; The analysis in chapter six of this thesis is based on his previous work. The combination of his openness and technical expertise is inspiring to me;

Members on my defense and reading committees at Stanford for their accommodation: Professors Tony Siegman, David Miller, Len Tyler, and Tom Lee. I am certain that I hold the record of having the easiest time scheduling my defense and getting my thesis read. Special thanks go to Professor Siegman, my associate advisor, for his advice and example;

The staff at UC Berkeley, who have collectively adopted me into their family: The Microlab, with special thanks to Charles H. Williams, III and Robert Hamilton for keeping the equipment up, and along with that, my sanity; Professor John Whinnery,

for his help directing me to the appropriate references for the fringing field discussion in chapter five; the EECS and ERL staff in Cory Hall; and Hilton, the first floor custodian in Cory Hall, whose steady smile never fails to energize me for the trip home at the end of the day, no matter how late it is;

The AT&T (Lucent) Graduate Research Program for Women, for a graduate fellowship and Dr. Martin Nuss of Lucent Technologies-Bell Labs, my mentor, for starting me off down this wonderful path;

DARPA Ultra contract N00014-96-1-1267 for funding this project;

Julie Sheridan-Eng and Lars Eng, for their advice, encouragement, and friendship;

My buddies, drinking and otherwise, from my college days, whose friendship all these years has been crucial to my remaining sane: Robert B. Lee, Yun and Nancy Loh, Karen Hong, Pete Sturdza, Leonard Chen, Kevin Kan, and Todd Gustafson;

The Larson family, for their constant love and encouragement since my high school days: Kristen, Mom and Dad, and Sarah;

My family: my parents, for their strength, fortitude, unending faith, and example; Uncle N.C. and Aunt Hoi, for starting me down this path of learning; my brother, for his kindness in deciding not to avenge for past misdeeds on the part of his big sister; my grandma and the memory of my grandpa, who held my hand as I wrote my first words;

And lastly but most importantly, Roger, who never ceases to amaze me everyday with his love and support, for showing me that compassion alone makes the man.

Table of Content

List of Tables

x

List of Illustrations

List of Acronyms

CD	compact disc
DVD	digital versatile disc
VCSEL	vertical cavity surface emitting laser
LAN	local area network
WDM	wavelength division multiplexing
GCSR	grating coupler with sampled reflector
InP	indium phosphide
AlGaAs	aluminum gallium arsenide
FSR	free spectral range
FP	Fabry-Perot
EM	electromagnetic
MBE	molecular beam epitaxy
RIE	reactive ion etch
HeNe	Helium-Neon (gas laser)
STP	standard temperature (300K) and pressure (1 atm)
CPD	critical point dryer
CO_2	carbon dioxide
psi	pounds per squared inch
CW	continuous wave
DQE	differential quantum efficiency
TIR	total internal reflection
fft	fast Fourier transform
ifft	inverse fast Fourier transform

Chapter 1

Introduction

Emission wavelength tunability in lasers allows an extra degree of freedom that opens new doors in the lasers' applications. The first tunable organic dye lasers were aimed at spectroscopy of materials.[1] With the advent of the semiconductor diode laser, vastly different arenas have opened up for applications requiring miniature lasers. Those that permeate our daily lives range from sources for telecommunications applications and data storage (CD's and DVD's) lasers all the way to the checkout scanners at our neighborhood grocery stores. Through the years, there has also been a concerted effort to develop a miniature version of the tunable dye and solid state lasers as well, although the journey has not yet proved as successful as in the examples mentioned above. In this chapter, some of the many applications for compact tunable sources will be discussed first. As the in-plane diode laser has had a longer history than its vertical cavity counterpart, so is the case for the tunable diode laser. Therefore, we will briefly mention the performance and results obtained thus far with the tunable in-plane diode laser. We will put our own research on the tunable vertical cavity surface emitting laser (VCSEL) in its proper context. Finally, a cursory review of earlier works in this field is given to conclude this introduction and render in perspective the work described in this thesis.

1

I Applications for compact tunable sources

A host of applications springs to mind for a compact tunable source. Spectroscopy remains a strong driving force. The popularization of the internet and the subsequent explosion of its traffic over the last five years has also formed a catalyst to drive the demand for tunable semiconductor diode lasers. Newly installed local area data communication networks are hard-pressed to meet the exponentially increasing traffic and bandwidth demand. Borrowing a lesson from the experiences of long-haul fiber optic communications carriers, local area network (LAN) planners seek to increase the available bandwidth of their existing fibers through wavelength division multiplexing (WDM). Because photons of different wavelengths at sufficiently low powers do not interact with each other in the fiber, the same optical fiber can be used to carry many channels of electrical signals embedded onto these different wavelengths of light. WDM is a cost-effective way to increase the aggregate bandwidth of a fiber already in the ground.[2] Provided that component costs and their associated power penalties are sufficiently low[1], it is far more economical to use multiple laser sources with each at a different emission wavelength and a wavelength-combiner[2] at the transmitting end of a link than to dig trenches in the ground to lay new, parallel fiber cables.

---

[1] This could be a very big assumption at times. Very frequently, viable component costs and performance specifications are driven by the economics that are governed simply by the number of end users on the network. If more end users can be served so that each pays a negligible amount towards the initial capital investment, costs and power penalties are not serious issues. On the other hand, one would be hard-pressed to find customers willing to pay for a WDM upgrade on their existing network if they are to foot the majority of the bill!

[2] A wavelength combiner is usually a passive element that treats optical carrier wavelengths much like freeway on-ramps to cars. The multiple input wavelengths from the inputs of the combiner get merged into one output waveguide that carries a smaller version (power-wise) of each input. Usually the combiner consists of a family tree of 2-to-1 splices. Each splice nominally comes with a 3dB power loss from input to output.

2

In light of the economics of WDM communications, the tunable diode laser can pose a formidable enabling force. Its compact size and potentially low cost make it very attractive for WDM applications. If readily manufactured, the tunable semiconductor laser can revolutionize WDM systems in ways that affect both their manufacturing and implementation.

With regards to the manufacturing of WDM transmitters, there is plenty of room for improvement in today's technology: The WDM transmitter is assembled by handpicking the laser for each wavelength channel. Each of these lasers is well characterized. This means that the emission wavelength as a function of both the injection current and the substrate temperature is thoroughly mapped out before the laser is placed onto a thermoelectric (TE) cooler. Before the transmitter box is shipped, each TE cooler is individually set to provide a precise substrate temperature with its resident-on-board programmed to run at a fixed current level. This is no trivial task when there are 80 channels in each box![3] The amount of labor and "art" involved in delivering only the transmitter not only keeps the cost out of reach for the short-distance market[4] but also poses substantial problems in terms of reliability and contingency parts for the product.

Now, let us explore what would happen if a tunable diode laser could be readily manufactured. Not only is it no longer necessary to keep an inventory of 80 bins of lasers, it is also a lot simpler to assemble a transmitter box together. Instead of

---

[3] At the time of this writing, Lucent Technologies has announced their "Wave Star" product that uses 80 WDM channels at 50GHz spacing in the 1.55μm low-loss band of the optical fiber, which would be ready for release some time in 1999.

[4] WDM is only used in the long-haul market these days, which typically span distances of 500km or so. Smaller scale markets, such as that for metropolitan areas (~50km) or local areas (~5km), have fewer subscribers that WDM has not proved economical yet.

individualizing each channel with its operating current and temperature, all that is necessary with a tunable source is feedback circuits to actively control each channel's wavelength.

Already there are tunable diode laser products available in the marketplace today for WDM testing and spectroscopy applications. However, these modules tend to come in big boxes and are fairly expensive because they involve external cavity configurations. Consequently, a fair amount of fine-tuning in the assembly of each module as well as the alignment of a few critical bulk optics components is required.[5] Though extremely useful for testing and instrumentation, their bulkiness and their price tag present significant hurdles that prevent these lasers' inclusion in any realistic, practical WDM systems. For the moment though, let us explore the possibilities in the event that a tunable laser could be miniaturized to the size of a speck of dust, following the trail blazed by the diode laser in other applications.

First of all, let us take a step back and examine how WDM is defined today and how this definition can expand if tunable lasers and detectors became a widely available enabling technology. Today's WDM networks refer to those whose optical signals are multiplexed and transmitted via a single fiber. Simply put, the single strand of optical fiber acts as an express highway that connects two specific geographic locations for vast amounts of optical-domain information without allowing any merging or exiting traffic en route. This definition of WDM networks can be

---

[5] For example, the New Focus Catalog this year (1998/99) boasts a product line of tunable diode lasers with narrow linewidths. This includes the 6300 Velocity series and the 6000 Vortex series. Each laser comes in a sturdy well-designed package and a hefty price tag from $7,900 to $25,000. Hewlett-Packard also has a tunable laser product, the HP8168 series, that comes in a box the size of a stack of four or five large pizza boxes at an even heftier price range of $29,000 to $65,000!

expanded if a cost-effective tunable source/receiver is available. For example, let us

consider a WDM local area computer network like that shown in figure 1.1 below, in

which each node is receptive to only a specific wavelength. Equipped with a tunable

source, each node can address any other independently. With the restriction that a

receiver node cannot be addressed by more than one transmitting node at the same

time, as many as N/2 connections can be handled simultaneously, where N is the total

number of nodes in the network.[6]
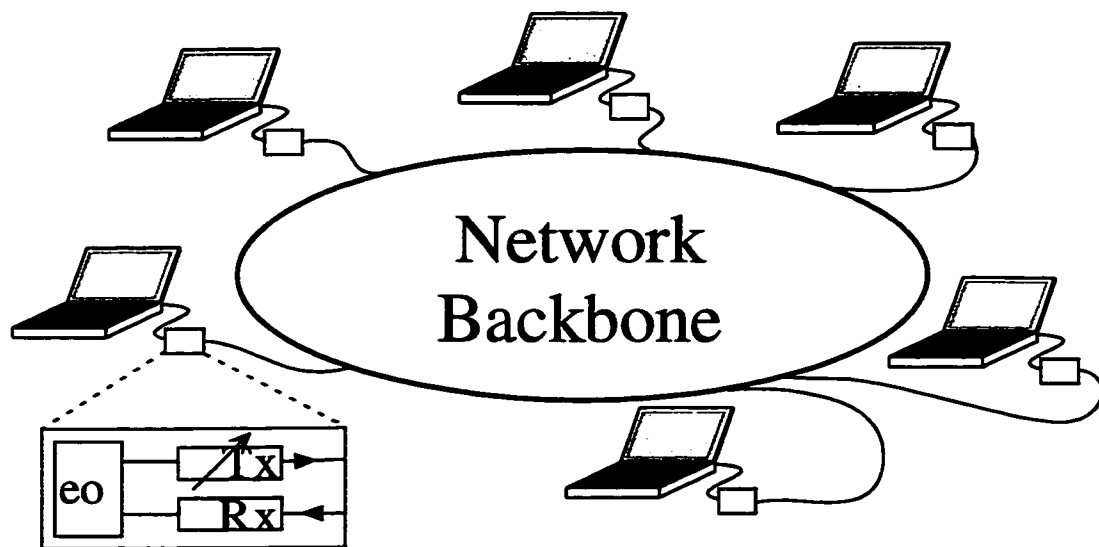
Figure 1.1 WDM high-speed computer network using tunable lasers and fixed wavelength photo-detectors
In this example, each node is connected to the centralized optical backbone of the network through a "box" that handles the electrical-optical conversion. This box contains a tunable laser (Tx) capable of addressing any other node on the network and a fixed wavelength photo-detector (Rx) for receiving messages.

Although the scheme shown in figure 1.1 allows extra nodes to be added onto

the existing network without having to lay extra cables in the backbone, its main

limitation lies in the fact that there can only be as many nodes (computers) as channels

(wavelengths). No two computers can share the same channel due to their fixed

---

[6] Clever schemes can be implemented to avoid this problem, such as setting priorities of messages for real time arbitration or further multiplexing the messages using code-division multiple access (CDMA), etc.

5

receiving wavelength. In other words, this network is not very scalable. To make such a network scalable and reconfigurable, tunable sources and receivers have to play a more central role. Instead of a prescribed static assignment of nodes to wavelengths as in figure 1.1, real-time configurable mapping of wavelengths-to-nodes provides the distinct advantage that endpoint-to-endpoint links can be optimized based on service criteria like minimum delay, load, or number of hops[7]. Once the traffic pattern of the network or the congested nodes has been surveyed and assessed in real-time, a central controller can automatically configure the wavelength-to-node map of the network to provide better overall performance for the entire network. Thus, cost-effective tunable sources with good performance could make a solid contribution towards bringing such networks into reality.

II   Background on tunable in-plane diode lasers

Thus far we have established the applications that demand a compact, cost-effective and simple-to-use tunable source. Semiconductor diode lasers suit the size and ease-of-use requirements for these applications. Indeed, much research effort has been devoted into bringing such a laser into reality. To put the tunable VCSEL work described in this thesis into its proper context, it is important to survey its edge-emitting counterparts' performance to render a fair comparison between the two.

Shown in figure 1.2 is a plot of the normalized tuning ranges ($\Delta\lambda/\lambda$ or $\Delta v/v$) of tunable edge-emitting lasers in the literature. Each distinct symbol represents a different scheme. These range from the use of vertical cavity couplers [3],[4], Y-

---

[7] The number of hops refers to the number of nodes a message encounters en route from the source node to the destination node, discounting the latter.

junctions[5],[6], various schemes using "superstructure gratings"[7],[8], to plain temperature tuning[9]. The record demonstrated to date is a Grating Coupler laser with Sampled Reflectors (GCSR) from the Royal Institute of Technology in Sweden, which spans 114nm at 1.55μm[10]. Given this spectacular result, one may wonder, quite naturally, why there is still room for ongoing research on tunable diode sources.
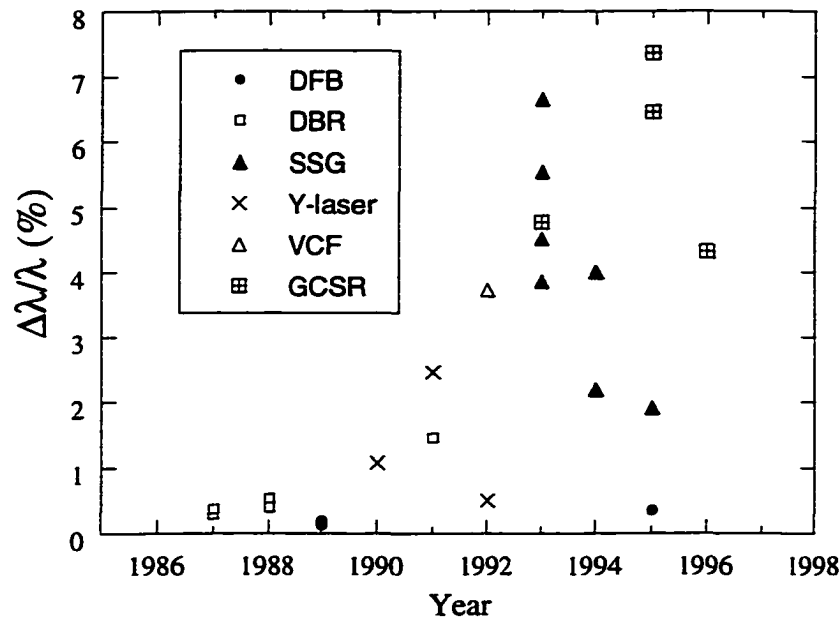
Figure 1.2 Normalized tuning ranges of tunable edge-emitting lasers reported in the literature over the years
The reported tunable lasers include various schemes that range from simple temperature tuning (DFB, DBR), use of superstructure gratings (SSG), vertical cavity filters (VCF), and a combination of those (GCSR).

As it turns out, there are quite a few undesirable features in the performance of tunable edge-emitting diode lasers. These range from complicated tuning schemes, high required tuning power, and difficult fabrication. To demonstrate the first point, shown in figure 1.3 below is the tuning curve, i.e. the lasing wavelength plotted against tuning input parameter which happens to be input current in this case, for the record-holding tunable laser. An overriding characteristic in the tuning curves of edge-emitting lasers that boast large or extended tuning ranges is the staircase feature

7

obvious in figure 1.3. Not every wavelength is equally accessible. To obtain the wavelengths buried into the vertical jumps in the staircase, extra tuning contacts are added to the lasers, further complicating both the tuning scheme and device fabrication.
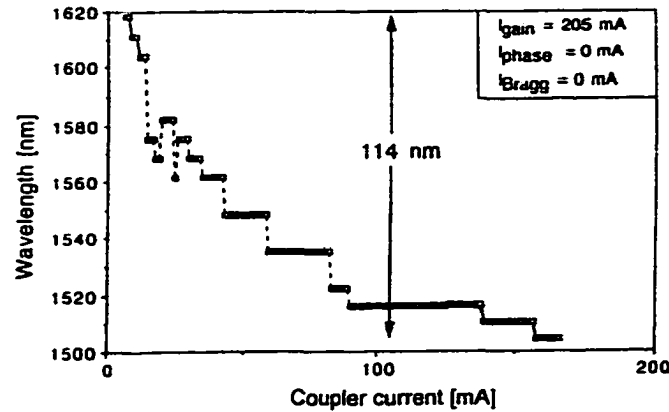
Fig. 3. Coarse tuning of the GCSR laser.

Figure 1.3 Tuning curve for record-holding GCSR diode laser with the widest tuning range to date
After reference [10]

Another undesirable feature in the edge-emitting tunable diode lasers is the fact that the predominant tuning mechanism is through current-induced temperature changes within the laser structure. Very often a large amount of current is required. Note that in figure 1.3, ~100mA is necessary to achieve tuning over a significant range of wavelengths.[8] Because of the multiple tuning contacts in each laser, one can imagine the amount of current and consequently, tuning power, necessary to achieve sufficient changes in the emission wavelength.

A further problem for tunable edge-emitting diode lasers is the very complicated fabrication scheme necessary to realize them. More often than not,

---

[8] Note that this is the current into *only* one of the four tuning contacts in this particular device.

8

multiple regrowths of material are necessary to accommodate the many grating photolithography steps, transparent wave-guide materials used in the structure, as well as isolation between the multiple tuning contacts. As an example, fabrication of the GCSR laser whose characteristics are shown in figure 1.3 includes four regrowths on top of the original epitaxial layer. Such a complex fabrication scheme has several important consequences for the viability of the device in practical applications. First, the quality of the regrown material is usually not as good as that in the original epitaxial layer, although the indium-phosphide (InP) material system is more forgiving with regards to regrowths than those that contain aluminum. Specifically for lasers, the quality of the gain material is of paramount importance to the performance of the device, which can be compromised if the gain material was regrown. Second, increasing the number of steps and fabrication complexity lowers the yield for these devices. Last, and perhaps most important, low yield manufacturing processes preclude cost-effective components. Exorbitant component cost can preclude the widespread implementation of new and revolutionary applications such as those mentioned earlier in this chapter.

All these complications associated with the tunable edge-emitting diode laser arise from the simple fact that its free spectral range is narrow, spanning at most a few (~2) nanometers. The staircase feature described earlier is caused by the uncontrollable mode-hopping between adjacent Fabry-Perot (FP) modes of the

resonant cavity.[9] Consequently, all these complex tuning schemes are carried out to combat and control this mode-hopping behavior.

III   Background on tunable VCSELs

In contrast to its edge-emitting counterpart, the tunable VCSEL has a few inherent properties that prove advantageous. First, the VCSEL's short cavity length, which is on the order of 3λ's, compared to at least 100λ's in a short edge-emitting laser as sketched in figure 1.4(a), renders a much wider free spectral range (FSR) through which continuous tuning can be obtained. Sketched in figure 1.4(b) as a comb of delta functions is the set of resonant frequencies of the two respective lasers. Note that the FSR is the separation from one resonant frequency, also called a Fabry-Perot (FP) mode of the cavity, to its nearest neighbor. This spacing can be found simply:

$\dfrac{c}{nL}$; where c is the speed of light, n the refractive index of the cavity medium and L the roundtrip cavity length. The FSR in a VCSEL is large due to the small L. Therefore, the longitudinal modes of the VCSEL cavity are spaced far enough apart that very often only one overlaps with the gain spectrum. This point is illustrated in figure 1.4(b) as well, where the gain spectrum of the lasers is superposed over the comb of FP modes. Mode hopping between adjacent FP modes is minimized in the VCSEL because usually only one FP mode would fit within the spectral gain bandwidth. Sketched in figure 1.4(c) are the resultant oscillation frequencies from the two cavities. Because both the available gain and the comb of FP-modes govern these

---

[9] The cavity simply selects its proper resonant frequency given its boundary conditions determined by the profile temperature, refractive index and length. More often than not these parameters cannot be controlled absolutely. Thus researchers go through great lengths to prevent mode hopping.

10

oscillation frequencies, the lasing modes tend to be more stable in the VCSEL cavity than in the edge-emitting laser when the gain profile shifts due to changes in the operation condition.
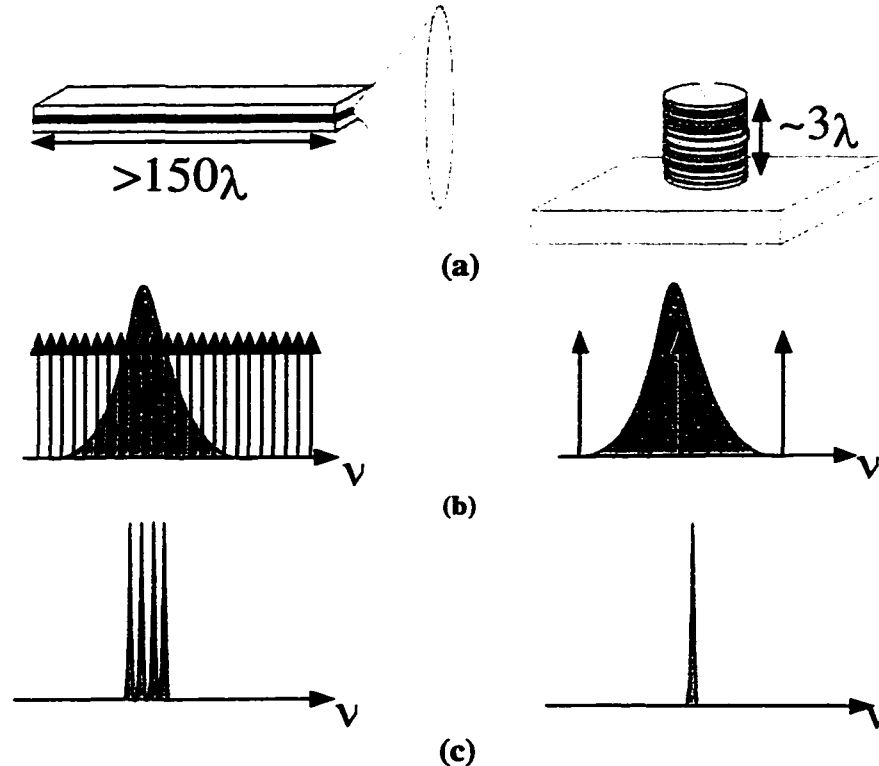
Figure 1.4 Main differences between VCSELs and edge emitting diode lasers
The main difference between a VCSEL and its edge-emitting counterpart is its short cavity length. Because the VCSEL cavity is only about 3λ's long versus the more than 150λ's in the edge-emitting laser, as drawn in part (a), the resonant wavelengths in the VCSEL are spaced farther apart. When superposed upon the gain spectrum as shown in part (b), one can see that only one longitudinal mode can experience sufficient gain for laser operation. This is drawn in part (c).

The second aspect inherent in a tunable VCSEL that gives it an advantage over its edge-emitting counterpart lies in its structure that readily renders mechanical tuning feasible. As will be explained in detail later on in this thesis, mechanical tuning is an effective and power efficient means of achieving wavelength shift. Only one tuning contact is required. And since this tuning contact is a reverse biased pn-junction, only the leakage current contributes to the tuning power, which is on the order of a few microwatts. A significant utility of a single tuning junction lies in a simply

implemented tuning scheme. Furthermore, the tunable VCSEL is monolithic, its fabrication process requiring no regrowths. As discussed earlier, a simple high-yield manufacturing process can ultimately translate into lowering the hurdles for device implementation into more applications.

Of course, there are other advantages that the VCSEL holds over the edge-emitting diode laser. These include the symmetric, circular output mode shape for ease of fiber coupling (figure 1.4a), a geometry that renders the VCSEL ready for two-dimensional integration for batch testing and manufacturing, and its small optical volume that makes it ideal for operations requiring low input powers.

Given the tremendous potential for a tunable VCSEL when compared to its edge-emitting cousin, it is not surprising that much effort has been concentrated in its research. This thesis constitutes a continuing effort in this area in Professor Chang-Hasnain's research group. To preface this work, previous approaches and some background in the tunable VCSEL are discussed first.

There have been two main competing schemes to realize the mechanically tuned VCSEL. While both are similar in principle, there are subtle distinctions as well as strengths and weaknesses to each. We shall briefly discuss these differences in the following section.

The first tunable VCSEL was demonstrated in 1995 [11], which forms the basis for the work presented in this thesis. The entire VCSEL structure was monolithically grown. Mechanical tuning was achieved through a singly-supported cantilever structure. Another tunable VCSEL structure soon followed suit.[12] It used dielectric top mirrors and a mechanically movable structure that has multiple

supports, like a trampoline. Both schemes rendered devices that demonstrated 19.1nm

of continuous tuning around 950nm.[13],[14],[15]. Recently, another tunable VCSEL

using a similar trampoline mechanical structure demonstrated 25nm of tuning.[16]

Although the differences between these two schemes may seem fairly subtle, the

consequences in terms of their feasibility and manufacturability are substantial, as we

shall see. We thus will briefly present these distinctions and their ensuing advantages

and disadvantages in the following section.

As discussed before, the main differences in the two existing schemes for a

monolithic tunable VCSEL[10] lie in the materials used in the top mirror and the number

of supports used in the movable mechanical structure. These two distinctions address

two interrelated concerns. First, a multiply-supported structure, if all supports are

balanced evenly, ensures that less tilt is incurred when the mechanical structure

moves. However, as we will see in chapter five, more applied force is necessary to

actuate a multiply-supported structure than an otherwise equivalent singly-supported

structure. Also to be shown in chapter five, there exists a tradeoff between the applied

voltage and the thickness, t, of a mechanical structure. The thicker the structure, the

higher the applied voltage, which goes as $t^{3/2}$. For low enough tuning voltages to be

used, a thinner movable multiply-supported structure is realized through the use of

dielectric materials. The subsequent device design and fabrication advantages and

disadvantages are discussed in detail in chapters two and three.

If one can safely assume that substantial tilt would not be incurred during the

normal operation of a tunable VCSEL even when a singly-supported mechanical

---

[10] There are ways to make tunable diode sources as hybrids somewhere between an external cavity tunable laser and a monolithic tunable VCSEL. The interested reader is referred to [17].

13

structure like the cantilever is used, then everything else is quite straightforward. The entire structure, including the two mirrors, can be monolithically grown. There is no need for dielectric mirrors to keep the tuning voltage realistically low. Furthermore, a great deal of complexity in the device design and fabrication can be sidestepped.

It is noteworthy to report that recently a tunable VCSEL based on the trampoline structure, but with an added novel aspect of a curve mirror, demonstrated 30nm of tuning near 850nm[11][18]. Obviously, the concern for mirror tilt is genuine enough that great lengths have been gone over to avoid the use of a cantilever structure. Chapter six of this thesis discusses the optical losses associated with the tilt in a cantilevered tunable structure. Our findings may surprise those who don't believe the cantilever would work as a mirror.

IV   Overview of thesis

This thesis describes the latest work on the tunable VCSEL using micro-mechanically tuned cantilevers. As we would like to give an account of the whole story, the design issues, fabrication, performance and analyses of these VCSELs are to be given in detail.

To provide a sufficient background detailing the optical, electrical, and mechanical constraints and criteria, chapter two provides some design examples and considerations. Since device fabrication is as important as its design, chapter three is devoted to the details in the fabrication process. Some tunable VCSELs' performance is outlined and presented in chapter four. The limitations on their performance will be explained and discussed as well. Although we can understand a great deal of the

---

[11] Although this device worked only in pulsed mode, the technology looks very promising nevertheless.

behavior of these devices through experimental observation, it is also of paramount importance that we understand the constraints inherent in our devices. Consequently, two subsequent chapters are devoted to analyses of the mechanical tuning and the optical properties of these VCSELs. Chapter five gives the background and analysis regarding the electromechanical tuning of our cantilever structure to show the tradeoffs in tuning voltage and geometry. Good agreement is obtained between our analytical results and experimental observation. Detailed analysis of the optical modal behavior within the cavity in our VCSEL is given in chapter six. A good qualitative agreement is found between the results of our analysis and our experimental data as well. From these exercises, we find the performance tradeoffs between the tunable VCSEL and that of a conventional VCSEL.

Finally, we will conclude with some observations arising from our experiments and calculations. Directions and implications for the future of this work will be discussed.

V   References

[1]   A. Goldstein and F. H. Dacol, "A reliable flashlamp pumped tunable organic dye laser," *Review of Scientific Instruments*, vol. 40, pp. 1597-8, 1969.

[2]   B. Mukherjee, *Optical Communication Networks*. San Francisco: McGraw-Hill, 1997.

[3]   R. C. Alferness, U. Koren, L. L. Buhl, B. I. Miller, M. G. Young, T. L. Koch, G. Raybon, and C. A. Burrus, "Broadly tunable InGaAsP/InP laser based on a vertical coupler filter with 57-nm tuning range," *Applied Physics Letters*, vol. 60, pp. 3209-3211, 1992.

[4]   M. Oberg, S. Nilsson, K. Streubel, J. Wallin, L. Backbom, and T. Klinga, "74 nm wavelength tuning range of an InGaAsP vertical grating assisted codirectional coupler laser with a rear sampled grating reflector," *IEEE Photonics Technology Letters*, vol. 5, pp. 613-615, 1993.

[5]   M. Schilling, H. Schweizer, K. Dutting, W. Idler, E. Kuhn, A. Nowitzki, and K. Wunstel, "Widely Tunable Y-Coupled Cavity Integrated Interferometric Injection Laser," *Electronics Letters*, vol. 26, pp. 243-244, 1990.

[6]   W. Idler, M. Schilling, D. Baums, G. Laube, K. Wunstel, and O. Hildebrand, "Y-Laser with 38nm Tuning Range," *Electronics Letters*, vol. 27, pp. 2268-2269, 1991.

[7]   Y. Tohmori, Y. Yoshikuni, H. Ishii, F. Kano, T. Tamamura, and Y. Kondo, "Over 100nm Wavelength Tuning in Superstructure Grating (SSG) DBR Lasers," *Electronics Letters*, vol. 29, pp. 352-354, 1993.

[8]   V. Jayaraman, A. Mathur, L. A. Coldren, and P. D. Dapkus, "Extended Tuning Range in Sampled Grating DBR Lasers," *IEEE Photonics Technology Letters*, vol. 5, pp. 489-491, 1993.

[9]   M. Oberg, S. Nilsson, T. Klinga, and P. Ojala, "A Three-Electrode Distributed Bragg Reflector Laser with 22nm Wavelength Tuning Range," *IEEE Photonics Technology Letters*, vol. 3, pp. 299-301, 1991.

[10]   P.-J. Rigole, S. Nilsson, L. Backbom, T. Klinga, J. Wallin, B. Stalnacke, E. Berglind, and B. Stoltz, "114-nm Wavelength Tuning Range of a Vertical Grating Assisted Codirectional Coupler Laser with a Super Structure Grating Distributed Bragg Reflector," *IEEE Photonics Technology Letters*, vol. 7, pp. 697-699, 1995.

[11]   M. S. Wu, E. C. Vail, G. S. Li, W. Yuen, and C. J. Chang-Hasnain, "Tunable micromachined vertical cavity surface emitting laser," *Electronics Letters*, vol. 31, pp. 1671-2, 1995.

[12]   M. C. Larson, A. R. Massengale, and J. S. Harris, Jr., "Continuously tunable micro-electromechanical vertical-cavity surface-emitting lasers," *International Journal of Optoelectronics*, vol. 10, pp. 401-8, 1995.

[13]   E. C. Vail, G. S. Li, W. Yuen, and C. J. Chang-Hasnain, "High performance micromechanical tunable vertical cavity surface emitting lasers," *Electronics Letters*, vol. 32, pp. 1888-9, 1996.

[14]   M. C. Larson, A. R. Massengale, and J. S. Harris, "Continuously tunable micromachined vertical cavity surface emitting laser with 18 nm wavelength range," *Electronics Letters*, vol. 32, pp. 330-2, 1996.

[15]   F. Sugihwo, M. C. Larson, and J. S. Harris, Jr., "Low threshold continuously tunable vertical-cavity surface-emitting lasers with 19.1 nm wavelength range," *Applied Physics Letters*, vol. 70, pp. 547-9, 1997.

[16]   F. Sugihwo, M. C. Larson, C. C. Lin, W. Martin, and J. S. Harris, Jr., "25nm wavelength range tunable vertical cavity lasers," presented at No.97TH8279 1997 55th Annual Device Research Conference Digest, Fort Collins, CO, USA, 1997.

16

[17]   K. Hsu, C. M. Miller, D. Babic, D. Houng, and A. Taylor, "Continuously tunable photopumped 1.3- mu m fiber Fabry-Perot surface-emitting lasers," *IEEE Photonics Technology Letters*, vol. 10, pp. 1199-201, 1998.

[18]   P. Tayebati, W. Peidong, D. Vakhshoori, L. Chih-Cheng, M. Azimi, and R. N. Sacks, "Half-symmetric cavity tunable microelectromechanical VCSEL with single spatial mode," *IEEE Photonics Technology Letters*, vol. 10, pp. 1679-81, 1998.

Design of Micromechanical Tunable VCSELs

The previous chapter briefly introduced the applications for which an inexpensive, easy-to-use tunable VCSEL would be desirable. In this chapter, the design issues for these devices are outlined. We shall include considerations for the electrical, optical, and processing properties in the VCSEL structure as well as the wavelength dependence of such a device's expected performance across its tuning range.

There are two predominant schemes in which the micromechanical tunable VCSEL is realized[1],[2]. While the tunable section in one scheme [1] is a monolithic AlGaAs structure in the form of a cantilever, the other [2] uses a multiply-supported dielectric mirror stack. The results reported in this thesis come from a structure very similar to those in [1]. As hinted in chapter one, there are clear advantages and disadvantages to each scheme. In this chapter, we shall delve into a detailed explanation of the tradeoffs between the two. Depending on the requirements as specified by an application, one should choose the scheme capable of rendering devices that meet those specifications.

The first section of this chapter outlines the mirrors and cavity issues that are incorporated into the design of a conventional VCSEL. We will then describe in detail

18

the principle of operation for the tunable VCSEL and proceed to its epitaxial design. This chapter will close with a few sections delineating the tradeoffs when the different components composing the entire tunable VCSEL structure were varied, followed by the wavelength-dependent parameters of the resultant VCSEL structure and a discussion on how these variables would ultimately affect the VCSEL's performance.

I   Basic VCSEL structure

As any laser that requires positive feedback of light for its coherent amplification to occur, a VCSEL consists of two mirrors sandwiching a gain region in which the internal optical field is amplified. As described in the previous chapter, a VCSEL's short cavity length is an important property that allows it to tune across a broad wavelength range without any mode hopping. However, there are some built-in design constraints attributed to the short cavity. Therefore it is important that an overview of the mirrors and fundamental VCSEL cavity design be given before we embark into the details for the tunable VCSEL.

A   Mirrors

As discussed previously, an advantage of the VCSEL, which will be elaborated upon in this section, over its edge-emitting counterparts is the short cavity length. There is no free lunch, of course. An obvious shortcoming[1] is that the gain region would have to be short also. Typically, it is made up of several (1-5) quantum wells with each being on the order of a hundred angstroms thick. The resultant amplification per pass is typically on the order of ~1%. Since the roundtrip gain must equal the roundtrip loss for stable, sustained operation, i.e. lasing, to occur, a

---

[1] No pun intended, honest!

19

VCSEL's mirrors would have to be highly reflective (with power reflectance greater than 99.0%) to compensate for the ~2-3% roundtrip gain. Metallic coatings simply cannot deliver such high reflectance levels. Therefore, VCSEL mirrors are distributed Bragg reflectors (DBR) consisting of quarter wavelength thick layers with alternating refractive indices. As shown schematically in figure 2.1 the reflections of a normal incident wave at the design wavelength off each interface in the stack constructively interfere so that the reflection coefficient of the entire stack is very close to unity. Plane wave power reflection coefficients over 99.9% can be achieved by increasing the number of layers in the mirror stack or by choosing materials with large refractive index differences, i.e. large contrasts (Δn).
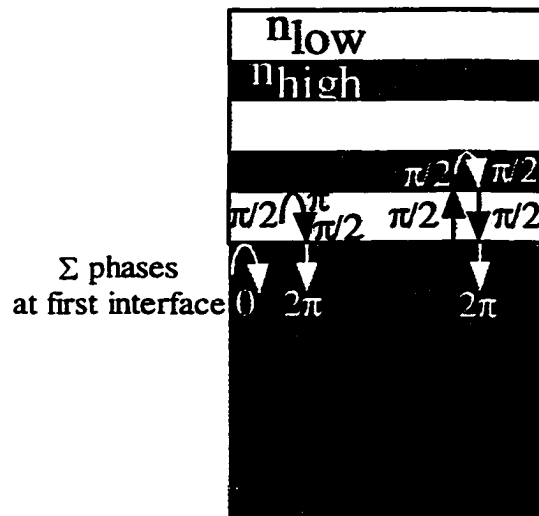
Figure 2.1 Quarter-Wave Distributed Bragg Reflector (DBR)
Each layer is a quarter of an optical wavelength thick. For a normal incident plane wave at the design wavelength of the DBR stack, its reflections at each subsequent interface all interfere constructively back at the first interface. In effect, the DBR forms a highly reflective mirror. Shown here is how the DBR works: Every time a plane wave is incident from a medium with a lower refractive index (n_{low}) upon a material with a higher index (n_{high}), its reflection experiences a π-phase shift. No phase shift occurs if the plane wave was incident from the n_{high} medium upon the n_{low} medium. Plane waves transmitted after each interface experience phase shifts due to the traversed distance, which is $\pi/2$ per layer. The phase of any reflection that returns to the first interface always adds up to multiples of 2π.

Material	n_{low}	n_{high}
$Al_xGa_{(1-x)}As$	~3.0 (AlAs, x=1.0)	~3.6 (GaAs, x=0)
$ZnSe/MgF_2$	1.37 (MgF_2)	2.48 (ZnSe)
$ZnSe/CaF_2$	1.43 (CaF_2)	2.48 (ZnSe)
Si_3N_4/SiO_2	~1.5 (SiO_2)	~2.0 (Si_3N_4)
$Al_xGa_{(1-x)}As/Al_xO_y$	~1.6 (Al_xO_y)	3.0-3.6 (AlGaAs)

Table 2.1 Refractive indices of materials commonly used for DBRs
Shown in this table are a few commonly used materials for VCSEL DBRs in the near infrared.

(a)   (b)
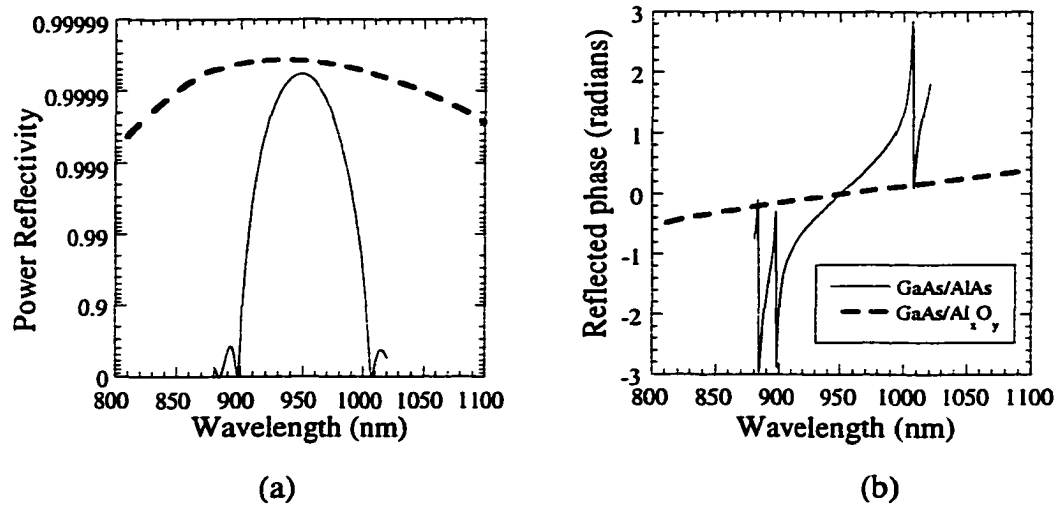
Figure 2.2 Power reflectance and phase for GaAs/AlAs and GaAs/Al$_x$O$_y$ DBRs
(a) The calculated power reflectivity and (b) phase of reflection (in radians) as a function of the normal incident plane wave's wavelength. The solid line represents a 30.5-pair GaAs/AlAs DBR and the dashed line is a 6.5-pair GaAs/Al$_x$O$_y$ DBR designed at 950nm. Both incident and exit media are GaAs.

Figure 2.2 shows the power reflectance and the reflected phase of normal incident plane waves for DBRs composed with two sets of the materials indicated in table 2.1. For ease in comparison, the power reflectance (y-axis) is plotted in reverse log scale so that each "higher" decade asymptotically approaches unity. The first point to make is that the power reflectance rolls off for wavelengths away from the design wavelength of the DBR. There are two reasons for this. First, the wavelength becomes detuned from the design wavelength (or the center wavelength) of the DBR so that each layer ceases to be exactly a quarter wavelength long. And secondly, the

21

refractive index for the AlGaAs material system is not constant with wavelength. The former, which can be seen in figure 2.2(b), accounts for most of the decrease from the maximum reflectance as the wavelength is detuned, while the latter causes a secondary dispersion effect, as can be seen in the non-constant slope of the plot in figure 2.2(b). Another notable characteristic is that both the reflection bandwidth and the maximum power reflectance are larger for the DBRs composed of materials with a larger Δn even though fewer layers are involved. This is because the magnitude of the reflection off each interface, r, is:

$$|r| = \frac{|n_1 - n_2|}{n_1 + n_2} = \frac{\Delta n}{2n_{ave}},$$

(2.1)

where n_{ave} is the average of the refractive indices of the two materials. (2.1) shows that for large Δn, each interface gives a stronger reflection and thus fewer interfaces are necessary to reach a target reflectance level required by the small cavity gain. For a thorough discussion on multi-layered structures, the reader is referred to [3] and [4].

The foregoing discussion on DBR design thus far has been concerned with only normal incident plane waves. In reality, since our three-dimensional (3D) VCSEL structures have finite sizes, the output eigenmodes are not simple 1D plane waves but also 3D vector entities. A detailed analysis and discussion of the reflection characteristics of these DBRs for the cavity eignemodes will be deferred until chapter six. For the express purpose of discussion on the design of micromechanical tunable VCSELs, it suffices to use the plane wave approximated DBR characteristics.

B   Cavity design

As we briefly mentioned earlier in this chapter, the internal electromagnetic (EM) field in a VCSEL has to see enough gain to counterbalance the loss it suffers

22

through one round trip for stable, self-sustained oscillation. Furthermore, the roundtrip phase of the complex EM-field has to be an even number of π radians such that this field replicates itself both in amplitude and phase after one transit around the cavity. Shown in figure 2.3 are the individual components this internal EM field sees in one cavity roundtrip. Mathematically they are summarized in (2.2):
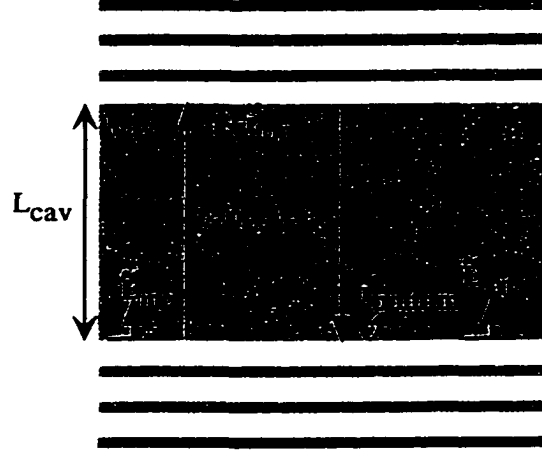
Figure 2.3 Phase and amplitude changes experienced by an internal EM-field in one roundtrip of the resonant cavity

The factors in equation (2.2) are denoted in this figure. $\tilde{E}_{inc}$ is the initial field, $e^{(g-jn_{cav})L_{cav}}$ is the gain and phase shift this internal field experiences through each trip down the cavity length L_{cav} with refractive index n_{cav}, and $\tilde{r}_{top}$ and $\tilde{r}_{bottom}$ represent the change in both amplitude and phase the field experiences upon reflection off the top and bottom mirrors, respectively. $\tilde{E}_{irt}$ is the resultant EM-field after one roundtrip in the cavity.

$$\tilde{E}_{Irt} = \tilde{E}_{inc} e^{(g-jn_{cav})L_{cav}} \tilde{r}_{top} e^{(g-jn_{cav})L_{cav}} \tilde{r}_{bottom} \equiv \tilde{E}_{inc} e^{j2m\pi}, \qquad (2.2)$$

where g is the one pass gain per unit length, n_{cav} the index of refraction for the material in the cavity, L_{cav} the cavity length, $\tilde{r}_{top}$ and $\tilde{r}_{bottom}$ the field reflectivity of the top and bottom mirror, respectively. The quantities $\tilde{A}$ indicate complex fields.

From the discussion in the previous section, we know that the DBR is not like a hard, discrete mirror well defined in space. As the name implies, it is a distributed

23

reflector by nature, and several complications therefore arise. The first is that since the $\tilde{r}_{top}$ and $\tilde{r}_{bottom}$ terms in equation (2.2) are complex numbers, designing a VCSEL with a fixed resonant wavelength requires that one take due account of the phases associated with these two mirrors at the design wavelength. Another arises from the fact that the refractive indices of most semiconductor materials are temperature-dependent so that the $\tilde{r}$'s are, too. Therefore, designing a tunable VCSEL requires that both the wavelength-dependent DBR phase and the temperature-dependent refractive indices be taken into account for all wavelengths within the tuning range of the laser.

The gain element is yet another critical component in the cavity. The standard definition of modal gain, g_{modal}, is as follows[5]:

$$g_{modal} = \frac{<\psi\,|\,g\,|\,\psi>}{<\psi\,|\,\psi>} = \frac{\int \psi^*(x,y,z)g(x,y,z)\psi(x,y,z)dV}{\int |\psi(x,y,z)|^2\,dV}, \qquad (2.3)$$

where g is the material gain[2] and ψ is the localized electric field. Equation (2.3) can be further simplified to (2.4) below if the longitudinal direction (z) is separable from the transverse dimensions (x and y) and if g is spatially independent:

$$g_{modal} = \Gamma_{xy}\Gamma_z g. \qquad (2.4)$$

Here Γ_{xy} and Γ_z are the 2D-transverse and 1D-longitudinal integrals, respectively, decomposed from the 3D-volume integral in (2.3).

---

[2] The material gain is simply the amount of optical amplification achievable from passing through the material, for the most general case of plane waves. The modal gain accounts for the amplification of a specific optical mode.

24

The transverse dimensions in a VCSEL are usually defined through photolithography and do not vary as the emission wavelength is tuned. Thus Γ_{xy} should remain relatively constant over the tuning range. Γ_z is more troublesome and needs further consideration. Ordinarily in the design of a conventional VCSEL, one would adjust the longitudinal position of the quantum wells and the cavity length until the calculated modal gain in (2.4) is maximized. This scenario is depicted in figure 2.4(a) below.

Gain→

(a)   (b)   (c)
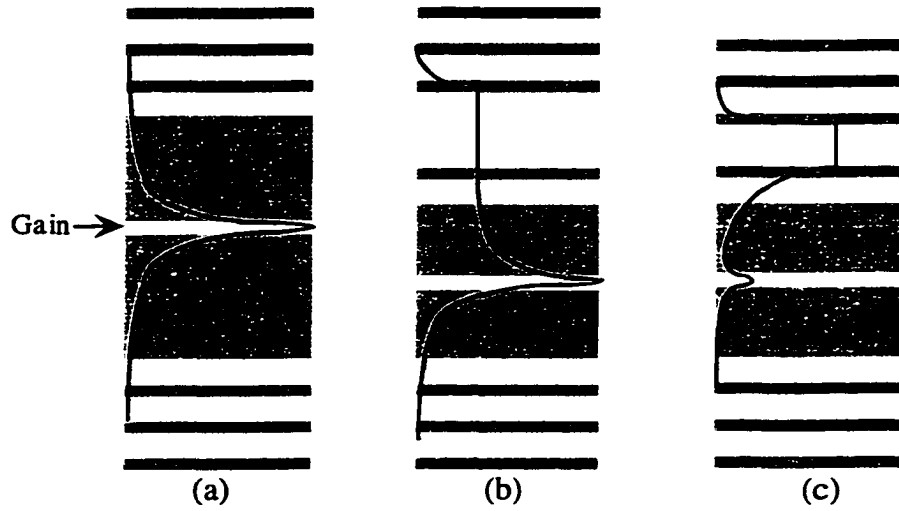
Figure 2.4 Standing wave envelope in VCSELs

In these figures, the standing wave pattern that describes the envelope of $\left|\psi(z)\right|^2$ in equation (2.3) is sketched in black lines. a) In a conventional VCSEL, g_{modal} is maximized through matching the peak of the standing wave envelope with the gain region. b) In a tunable VCSEL, g_{modal} is maximized only for a specific wavelength, but c) not at other wavelengths because the top mirror has moved relative to the gain region and the bottom mirror.

We will explain in the next section that wavelength tuning in the tunable VCSEL is achieved by physically changing the length of the cavity through the movement of one mirror. Thus, the resultant standing wave pattern inside the cavity, $|\psi(z)|^2$, also varies as one mirror moves relative to the other. This is the scenario depicted in figures 2.4(b) and (c). Since the position of the quantum wells in the cavity is fixed at all times, the modal gain in the longitudinal direction,

25

$$\Gamma_z g = \frac{g \int_{QWs} \psi^*(z)\psi(z)dz}{\int_{-\infty}^{\infty} |\psi(z)|^2 \, dz},$$ (2.5)

is also wavelength-dependent, as shown in figures 2.4(b) and (c). In section IV A below, we will quantify how much this factor varies across the tuning range.

Before moving onto the actual epitaxial design of the tunable structure, we digress slightly and discuss the tunable VCSEL's principle of operation. Familiarity with the tuning operation is crucial to understanding the steps taken in the final design of the device.

II   Principle of operation

The basic principle of operation of a tunable VCSEL is very similar to that of a scanning Fabry-Perot (FP) interferometer, illustrated in figure 2.5(a).[6] Two mirrors form the resonant cavity. When the distance between these mirrors changes, the transmitted wavelength of the cavity changes also. In our case, actuation is achieved electrostatically by reverse biasing a pn-junction sandwiched between a movable mirror and a stationary mirror. See figure 2.5(b).[7-9] The reverse-biased junction acts as a capacitor, the electrostatic attraction between whose charged plates causes the movable mirror to lower towards the stationary mirror. This effectively shortens the cavity length and thus blue-shifts the transmission wavelength of the structure, as in the classical FP-interferometer shown in figure 2.5(a). The two mirrors in figure 2.5(b) are shown as DBRs. Note that the tuning junction is sandwiched between the two mirrors.

(a)　　　　　　　　　　　　(b)
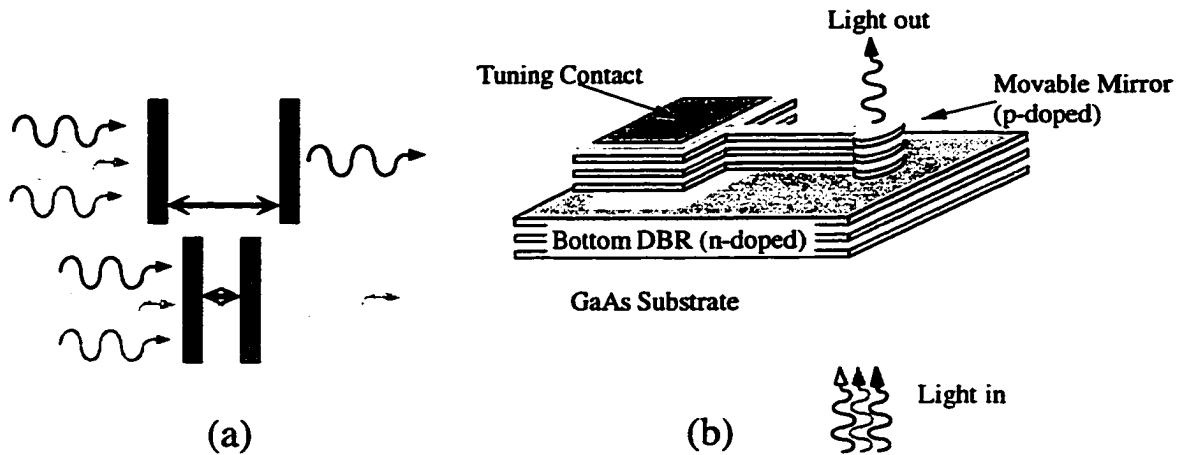
Figure 2.5 Principle of operation—Scanning FP-interferometer
(a) A scanning FP-interferometer is simply composed of two mirrors with a variable distance between them. (b) A micromechanical version of the scanning FP-interferometer has two DBRs with a variable distance between them. This distance is adjusted through a capacitor whose capacitance can be changed through a reverse-biased pn-junction. After [7-10].

A tunable VCSEL structure, shown in figure 2.6, is very similar to a scanning FP-interferometer. The main difference is that a gain element is added to the cavity. A more subtle difference is that the pn-junction is not situated between the two mirrors. Rather, it is located inside the top mirror, which happens to include a thick layer of air amongst the many layers that make up the DBR. The section of this top mirror that lies below the air gap serves to provide electrical contact to the gain region.

(a)　　　　　　　　　　　　(b)
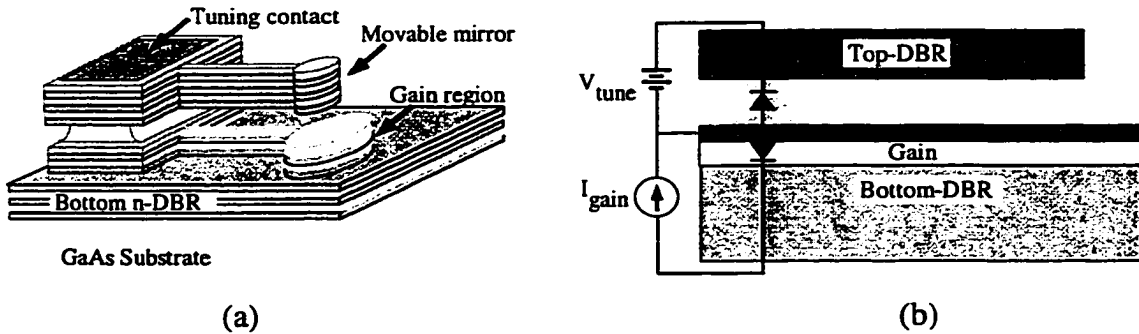
Figure 2.6 Principle of operation—Tunable VCSEL
(a) A 3D schematic of the tunable VCSEL. Like the scanning interferometer in figure 2.5(b), the tunable VCSEL has a movable and a stationary mirror. The main difference is that a gain element is inserted between the two. Also note that the tuning capacitor is now embedded into the top mirror instead of inside the cavity as in figure 2.5(b). (b) Side view of the VCSEL showing the electrical connections.

An important implication of the fact that the actuation occurs between sections of the same mirror is that the cavity length is not directly modulated. Rather, it is the phase of the reflection that is directly affected when the air gap is tuned. This is illustrated in figure 2.7(a), which schematically shows a DBR stack with an air layer of variable thickness in the middle.

(a)

(b)   (c)
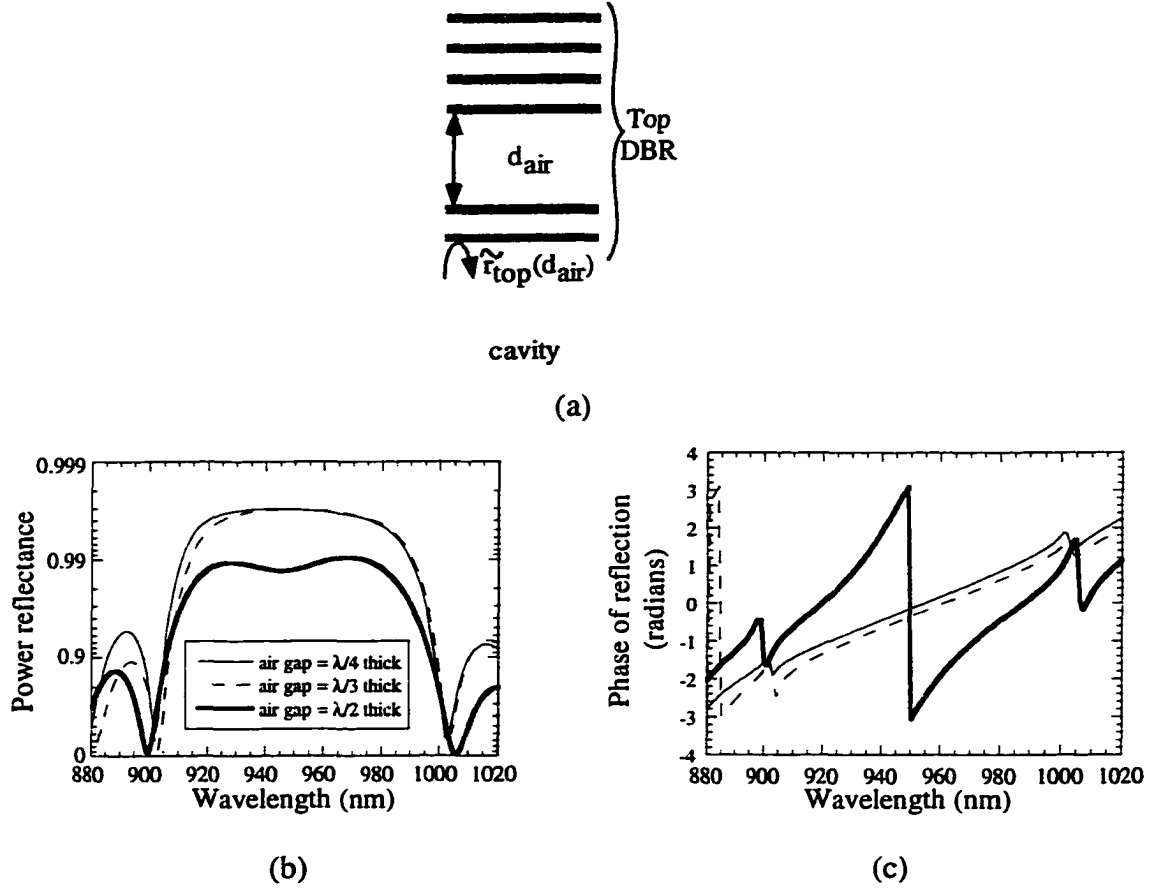
Figure 2.7 Top DBR in tunable VCSEL
a) The top DBR in a tunable VCSEL includes an air layer with adjustable thickness.
b) Power reflectivity and (c) reflected phase of a DBR plotted as a function of wavelength, for three different d_{air}: $\lambda/4$ (thin solid line), $\lambda/3$ (thin dashed line), and $\lambda/2$ (thick solid line); λ being the center wavelength at 950nm. The 2π-jump in phase for the $d_{air}=\lambda/2$ case in (c) is an artifact of the calculation. These calculations are for a DBR with 25 pairs of $Al_xGa_{(1-x)}As$ layers (x=0.1, 0.9).

As before, for ease in comparison, the power reflectance level has also been plotted in reverse log scale. From figure 2.7(b), the maximum power reflectance rolls off when the air layer deviates from a quarter of the center wavelength (i.e. 950nm in

28

the case of figure 2.7) for which the rest of the other layers have been optimally designed. More dramatically shown in figure 2.7(c) is the change in the phase of the reflected plane wave when the air gap thickness is at the anti-resonant condition (d_{air} = $\lambda/2$).[3] Referring to (2.2), $\tilde{r}_{top}$ now has amplitude and phase that are dependent on both the air gap thickness and the FP-wavelength. Since the entire bottom DBR is fixed to the substrate, $\tilde{r}_{bottom}$ in (2.2) is only a function of the incident wavelength. Equation (2.2) can now be recast as:

$$\tilde{E}_{lrt} = \tilde{E}_{inc}\tilde{r}_{top}(\lambda, d_{air})\tilde{r}_{bottom}(\lambda)e^{2\{g+jn_{cav}(\lambda)\}L_{cav}} \equiv \tilde{E}_{inc}e^{j2m\pi}, \qquad (2.6)$$

where λ indicates the wavelength variable, d_{air} the air gap thickness, and $\tilde{r}_{top}$, $\tilde{r}_{bottom}$ and n_{cav} have their respective dependencies on λ and d_{air} explicitly written out. As in (2.2), the second equality in (2.6) is the resonant condition. Therefore, the FP-wavelength of the structure with an air gap thickness of d_{air} is the wavelength at which the resonant condition is satisfied, i.e.:

$$\tilde{r}_{top}(\lambda, d_{air})\tilde{r}_{bottom}(\lambda) = e^{2\{j[m\pi-n_{cav}(\lambda)L_{cav}]-gL_{cav}\}}, m = 1,2,3,... \qquad (2.7)$$

A direct consequence of figure 2.7(c) and equation (2.7) is that the FP-wavelength shifts when d_{air} is varied. A more intuitive and less mathematical picture is that when d_{air} is increased, the part of the internal field that reaches the air gap (without being reflected by the previous interfaces) sees a longer path to the next interface and back, therefore the cavity would appear longer. Thus, wavelength-tuning here involves an indirect change of the cavity length through the direct adjustment of the reflected

---

[3] Note that the 2π-phase jump at 950nm for the $d_{air}=\lambda/2$ case in figure 2.7(c) is just an artifact of the calculation. The phase shift with wavelength should always be continuous.

phase from the top DBR. The FP-wavelength as a function of the air gap thickness for several tunable structures will be given in section IV below.

III   Tunable VCSEL structure

Having considered the mirrors and cavity that comprise a VCSEL and the principle behind the tunable VCSEL, we can put these ideas together into a design. Both the optical and electrical behavior of the materials making up the mirrors and cavity should be considered. In addition, details that would ease fabrication of these devices should be incorporated.
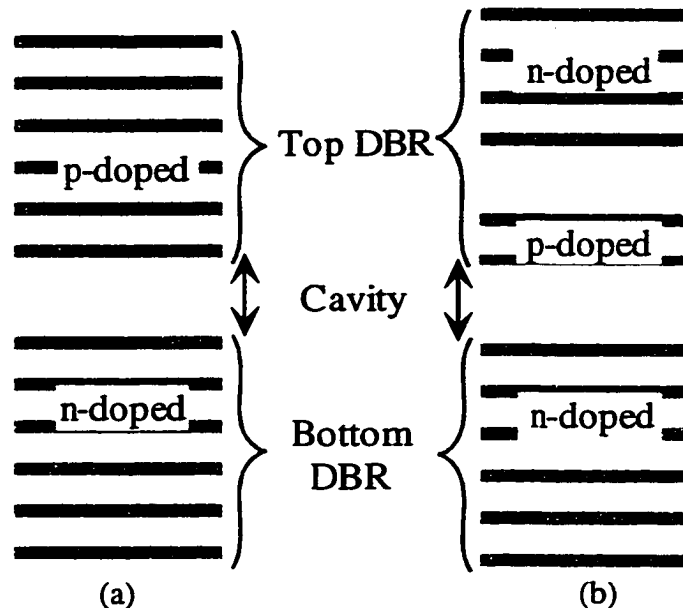
Figure 2.8 Comparison of layer structures of a conventional VCSEL and a tunable VCSEL
The differences between the layer structures of (a) a conventional (fixed-wavelength) VCSEL and (b) its tunable counterpart are the extra tuning pn-junction and the thick intracavity layer of air in the top mirror.

Shown in figure 2.8 are the epitaxial layers for a conventional VCSEL and a tunable VCSEL. Below we will outline the major differences between the two in their electrical and optical terms as well as aspects relating to their fabrication.

30

A Fabrication considerations

One blatant difference of the tunable structure from its non-tunable counterpart is the inclusion of an air gap. Our scheme requires a monolithically grown device, including the top DBR. This is because the precision of in-situ monitored growth in our molecular beam epitaxy (MBE) system is much better than any post growth deposition monitoring system our facilities offer. A sacrificial layer is used to form the air gap. The choice of this sacrificial material is dependent on the material system used in our VCSEL structure. As we are interested in demonstrating tunable VCSELs in the near infrared, AlGaAs layers and InGaAs quantum wells are the appropriate material choices for the mirrors and gain element. The important trick in getting the air gap to form lies in the wise selection of an etchant that would only attack the sacrificial layer. In the AlGaAs material system, many selective etches exist for attacking AlAs or GaAs against AlGaAs.[4] Specifically in our case, AlAs is to be used as an indispensable layer for gain confinement in the VCSEL structure. We thus have chosen to use GaAs for the sacrificial layer. Therefore a GaAs-specific selective etch is necessary to form the air gap. Fabrication details will be discussed in the next chapter.

B Differences in optical properties

The two comparable structures in figure 2.8 have very similar optical properties. The only major difference, again, is the air gap in the top mirror structure. If we recall (2.1), the strength of the two reflections off the two air-semiconductor

---

[4] There exist many good etchants that specifically attack either GaAs against any AlGaAs (including AlAs) layers or AlAs against any AlGaAs (including GaAs) layers. Far fewer etchants with high selectivity exist for the removal of AlGaAs layers against either AlAs or GaAs layers.

interfaces in the top DBR in figure 2.8(b) is seven times stronger ($\Delta n \sim 2.3$, $\Sigma n \sim 4.3$) than any reflection off any other interface in the wholly AlGaAs DBR ($\Delta n \sim 0.5$, $\Sigma n \sim 6.5$) shown in figure 2.8(a). For the same target DBR reflectivity and ignoring any optical absorption due to the presence of dopants (which will be discussed in the next section), fewer layers would be required in a tunable DBR than a wholly AlGaAs DBR simply because of the embedded air layer. This point is illustrated figure 2.9. The power reflectivity of two AlGaAs DBRs is shown. One DBR is composed entirely of AlAs/GaAs layers while the other has one AlAs layer replaced by an air gap.
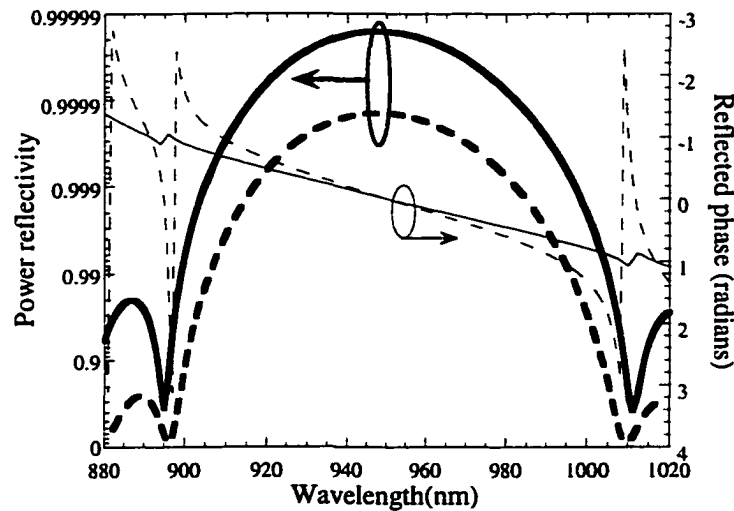
Figure 2.9 Reflectivity of two AlGaAs DBRs
Plane wave, normal incident (at the design wavelength) reflectivity and phase of two DBRs. Dashed lines show the reflectivity and phase for a DBR with 24.5 pairs of AlAs/GaAs layers while solid lines indicate likewise for the same DBR with one AlAs layer replaced by an $\lambda/4$ thick air layer. The design wavelength is 950nm. The incident medium is GaAs while the exit medium is air.

(For this calculation, the placement of this air gap within the DBR stack is not critical. However, the position of the air gap within the top DBR is important for another figure of merit for the tunable VCSEL, the tuning range. In section IV, we will quantify this tuning range as a function of the placement of the air gap from the

32

cavity.) We can see that the replacement of an AlAs layer with an air gap can enhance the peak reflectance by an order of magnitude!

C   Doping scheme

The doping scheme used in the growth of VCSELs is important because it has a large impact on the devices' electrical, thermal and optical properties. Good VCSEL performance is always a result of employing a doping scheme that strikes a good balance between the three. Most GaAs substrates come either doped n+ or semi-insulting from the manufacturer. For most AlGaAs VCSELs, the bottom DBR is n-doped while the top DBR is p-doped such that when the pn-junction is forward-biased, injected electrons and holes would recombine in the middle intrinsic gain region to generate photons.

In a conventional etched post VCSEL as depicted in figure 2.8(a), not enough dopants can cause high resistance across every heterojunction down the two DBRs. This high resistance in turn can cause the device to heat up and adversely affect the gain spectrum, which is very temperature sensitive: GaAs and InGaAs quantum wells' gain peak shifts at the rate of $\sim 3\text{\AA}/^{\circ}C$[11]! On the contrary, having too much dopant in the mirror could decrease the DBR's reflectance due to the increased free-carrier optical absorption.[12] Added to this mess of a situation is the complication that beryllium, a common p-dopant for AlGaAs in solid source MBE systems, does not incorporate into host sites as readily as silicon, the common n-dopant. Often VCSEL designs are compromised through the use of doping only the 3000Å of material that is closest to the p-contact high ($\sim 2e18/cm^3$) while doping the rest of the p-DBR and n-DBR to only half of that.

33

This is actually not a bad solution. Most of the photon energy is confined to within the first five pairs of the two DBRs closest to the cavity[13] so that free-carrier optical absorption due to the presence of the dopants is minimized. Figure 2.10(a) shows the standing wave pattern and dopant concentration profile in the longitudinal direction of the VCSEL. Equation (2.3) is also useful for the modal loss here. It is desirable to position large absorption losses where there is no substantial field, which is the case shown in figures 2.10(a) and 2.10(b). At the same time, the first 3000Å of semiconductor from the contact layer facilitates uniform current spreading into the tall DBR stack. By the time the carriers reach the gain region, the injection current would be such that spatially uniform gain can be achieved for the internal circulating field. A uniform current injection profile is sketched in figure 2.10(c).

(a)   (b)   (c)
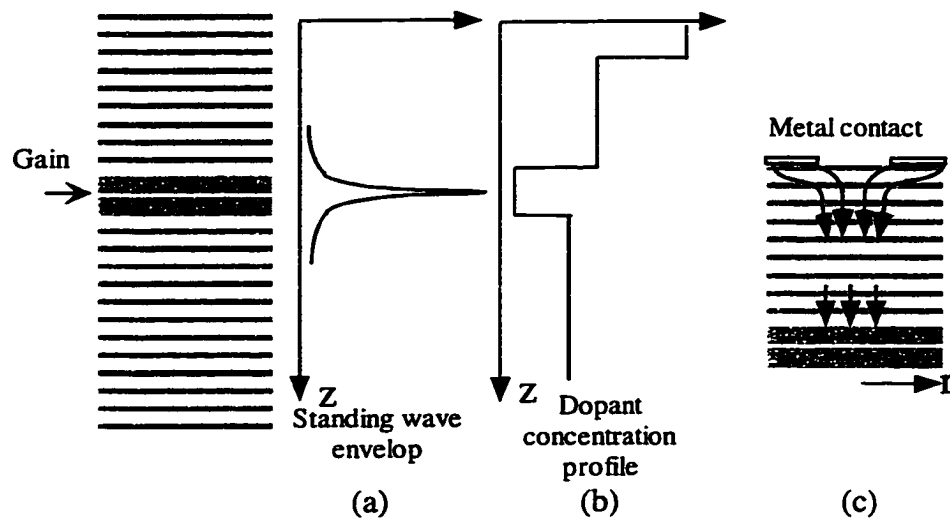
Figure 2.10 Doping scheme in conventional VCSELs that minimizes free carrier absorption while maximizing current injection uniformity simultaneously.
a) Standing wave pattern in a conventional VCSEL plotted against the epitaxial growth direction. b) Doping profile that minimizes absorption where the standing wave amplitude is high. It is also plotted against the epitaxial growth direction. c) The resultant injected current profile. The 3000Å of highly doped contact layer serves to spread out the injected current into subsequent layers.

The major difference in the doping schemes between the tunable and the regular VCSEL structure lies in the fact that there are two pn-junctions in the structure

34

depicted in figure 2.8(b) rather than the one in figure 2.8(a). The bottom half is the same for both. From the substrate up, the fixed DBR next to the substrate is n-doped while the cavity region above that is intrinsic, followed by a p-doped DBR. Here the similarities between the two end because the tuning pn-junction is formed in figure 2.8(b). Over the short section of the p-doped DBR, there comes an air gap, followed by a section of lightly doped (1e18/cm^2) n-DBR for the cantilever, with the last 500Å being more heavily doped (2e18/cm^2) for good electrical contact.

The good news is that in this tunable structure, fewer layers are p-doped compared to the conventional VCSEL. Thus the problem with beryllium incorporation does not affect the tunable VCSEL as much. The bad news is that because of the presence of the air gap, the short stack of p-DBRs will have to be doped as heavily as any contacting layers would have to be. This causes essentially the same pitfalls that intracavity contacted VCSELs face[14-16]: Because of such heavy doping near the center of the cavity where the photon density is high, optical loss from free carrier absorption can be expected to be high also. This extra absorption loss from an intracavity contact configuration could be as high as 0.1% per roundtrip, not an insignificant amount considering that the maximum roundtrip gain is only on the order of 2%.

D   Final structure

Now that we have briefly described the major optical, electrical and fabrication differences between the tunable VCSEL structure and the conventional fixed wavelength VCSEL, a general epitaxial layer structure is offered below in figure 2.11. (It should be noted here that Wupen Yuen and Gabriel Li, my coworkers in Professor

Chang-Hasnain's research group, have been responsible for the MBE growths of all the VCSELs reported in this thesis. For details of the growths, the reader is referred to their doctoral dissertations.[17],[18])

20.5 pairs n-DBR
(x=0.1/0.9)

1.4μm thick sacrificial layer

4 pairs p-DBR (x=0.1/0.5)

30 pairs n-DBR
(x=0.1/0.9)
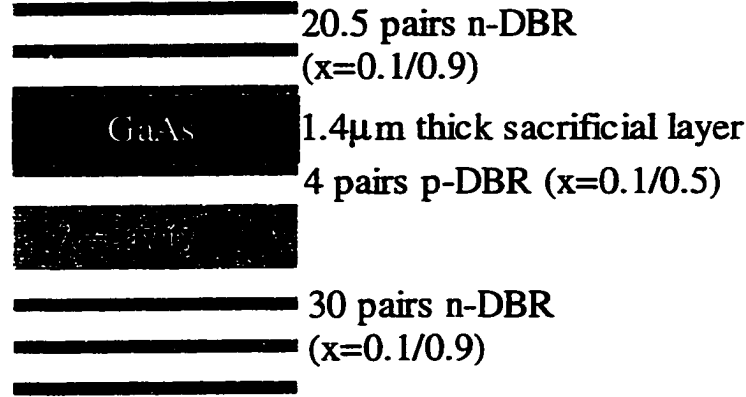
Figure 2.11 Tunable VCSEL epitaxial layer structure
The details of the layer structure are given in table 2.2 below. A 300Å thick AlAs layer is grown right above the cavity to provide device definition in the transverse directions through an oxidation process. Details of the oxidation process are given in the next chapter.

DBRs	n-DBR (movable section)	p-DBR	n-DBR (fixed section)
Number of pairs	~20	~3	30
Dopant concentration (bulk), in 1e16/cm^3	100	200	100
Dopant concentration (contact), in 1e16/cm^3	200	600	Contacted through n+ substrate
Material Composition	$Al_{0.1}Ga_{0.9}As/Al_{0.9}Ga_{0.1}As$		$Al_{0.1}Ga_{0.9}As/AlAs$
Cavity	Cladding	Quantum Wells	Barriers
Material Composition	$Al_{0.5}Ga_{0.5}As$	$In_{0.15}Ga_{0.85}As$	GaAs
Other characteristics	one-λ long	3 wells at 80Å thick	100Å thick
Sacrificial layer			
Material Composition	GaAs		
Dopant concentration	MBE background dopant (~1e16/cm^3)		
Thickness	1.4 μm		

Table 2.2 Summary of the epitaxial layers in the tunable VCSEL structure sketched in figure 2.11

Table 2.2 above lists the properties of the epitaxial layers in the structure.

Minor deviations from the table are adjusted in the final design for optimized

36

performance. We will discuss further the tradeoffs in these design adjustments in sections IV and V. Note that this design is put forth with a top-emitting VCSEL in mind. That's why the bottom DBR has higher reflectivity (and more mirror pairs) than the top DBR. This will not affect the results in our design tradeoff discussions in sections IV and V.

IV   Tuning range

Perhaps the most important figure of merit in a tunable VCSEL is the span of wavelength over which the device can lase. This section is devoted to the discussion of the tuning range in our device. Among the issues to be taken up are the factors that affect the tuning range in our structure, possible solutions to combat some of the shortcomings, the tradeoffs associated with a large tuning range, and its absolute maximum physical limit.

A   Tuning range as a function of number of pairs in the p-DBR stack

We saw in figure 2.9 that the power reflectance of the top DBR can be increased through the replacement of a low index layer by an air gap within the DBR. This is because each of the two air-semiconductor interfaces bordering the air gap has a field reflectivity at least six times stronger (40 times if the power reflectance is compared) than any other interface in the structure. The closer these interfaces are to the cavity, the larger is the fraction of the total optical energy in the structure that reaches the air gap. Consequently, increasingly efficient tuning can be achieved because more of the field experiences the phase change. This is illustrated in figure 2.12 below, where the resonant wavelengths of three tunable structures are plotted

37

against the thickness of the air gap. The only difference between the structures is the placement of the air layer within the stack.
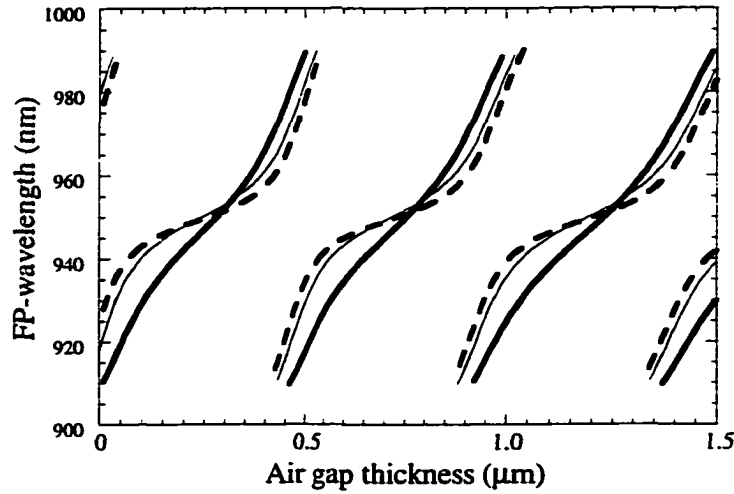
Figure 2.12 FP-wavelength plotted against air gap thickness for three VCSEL structures
The placement of the air gap within the top DBR is the only variable amongst the three sets of lines. The thick solid line is the unrealistic case where the air layer is placed immediately next to the cavity. The thin solid line indicates the case when the air gap is placed two AlGaAs pairs (i.e. four $\lambda/4$-layers) away from the cavity, while the dashed line is the case for which the air gap is placed four pairs (eight $\lambda/4$ layers) from the cavity.

Each set of curves associated with the specific structure above represents a solution of equation (2.7) given the specific top- and bottom-DBR. An obvious feature in the plot is that sometimes there are two possible solutions for the same air gap thickness. These two solutions actually come from the two adjacent longitudinal orders of Fabry-Perot (FP) modes depicted in figure 1.4(c). As mentioned in section III of chapter 1, the resonant modes of a linear cavity are separated by its free spectral range Δv_{fsr}, defined by:

$$\Delta v_{fsr} = \frac{c}{2n_{cav}L_{cav}}, \qquad (2.8)$$

where n_{cav} and L_{cav} are the refractive index and length of the cavity, respectively. Even though the VCSEL cavity is on the order of one wavelength long physically, two

longitudinal orders appear because the mirrors are distributed in nature: It takes approximately 5 pairs to reflect most of the optical energy[13]. The extra distance needed to completely reflect the field in each DBR lengthens the actual cavity on both sides. This is the reason that the actual VCSEL cavity is about three times its physical length.

Another notable feature in figure 2.12 is that as the air gap decreases, the adjacent longitudinal modes of the structure grow further apart. (Compare the difference in wavelength, for any curve, between the two modes when the air gap is 9500Å and that when the air gap is 4750Å.) This can be explained using (2.8). A smaller air gap contributes to a shorter cavity, therefore the free spectral range increases for decreasing air gap size.

As an instructive but unrealistic[5] example, one of the DBRs (the thick solid line) in figure 2.12 above includes an air layer that is immediately next to the cavity. It can be seen that this structure's tuning curve does not straighten out: The first air-semiconductor interface immediately reflects ~50% of the incident field. Therefore, at maximum, only half of the internal field reaches the air gap. To increase tuning efficiencies beyond this example, a broadband phase-matching layer can be grown between the air and the cladding material to enhance the coupling of the internal field into the air gap. Of course, an immediate and obvious drawback of utilizing such a phase matching layer is that the actual length of the cavity has been increased to include both the phase-matching layer's and the air gap's thicknesses. This longer

---

[5] It is an unrealistic example because contact layers are necessary to facilitate current injection. A thick (>5000Å) contact layer is preferred to ensure uniform current injection into the gain region for spatially uniform gain.

39

cavity may reduce the free spectral range to nullify any coupling enhancement of the internal field.

Another tradeoff lies in the fabrication of a tunable VCSEL that does not have a p-DBR section. If the selective etch does not leave behind a smooth air-semiconductor interface, any light that reaches the air layer would experience scattering loss on the surface. The internal field would require extra gain to counter-balance this extra scattering loss for lasing to occur. Therefore, even if the phase-matching layer can effect a wider tuning range, its stringent fabrication requirement and low yield may ultimately doom the device from realization.

B Tuning range for different DBRs

Figure 2.2 in section I A pointed out the characteristics of two sets of DBRs with different contrasts (Δn). We found that for the case of large Δn, fewer pairs are necessary in the stack to reach a target reflectivity because a larger Δn effects a stronger reflection at each interface. Does it actually matter what kind of DBR we use to maximize the tuning range? In this section, we will investigate how the tuning range is influenced by the choice of Δn in the movable mirror.

Table 2.3 lists the characteristics of two DBRs used for the movable mirror in a tunable VCSEL structure. Using these two DBRs, we find the resonant wavelength for each tunable VCSEL as the air gap thickness varies. For ease in comparison, the power reflectance of the two top DBRs at the center wavelength of 950nm has been adjusted to be the same to within 0.0001. Every other aspect of the two tunable structures from the air gap down to the substrate remains the same for the two

structures. Figure 2.13 displays the map of the two structures' resonant wavelengths as their air gap thickness varies.

	AlGaAs	Dielectric
Movable part (above air layer) High index material Low index material Number of pairs $\|R\|^2$ at center wavelength of 950nm	$Al_{0.1}Ga_{0.9}As$ (n = 3.472) $Al_{0.9}Ga_{0.1}As$ (n = 3.011) 19.5 0.99836	ZnSe (n=2.484) MgF_2 (n=1.374) 5.5 0.99827
Fixed part (below air layer) High index material Low index material Number of pairs	$Al_{0.1}Ga_{0.9}As$ (n = 3.472) $Al_{0.9}Ga_{0.1}As$ (n = 3.011) 3.5	

Table 2.3   Details of the two top DBRs used to calculate the FP-wavelength shown in figure 2.13 below
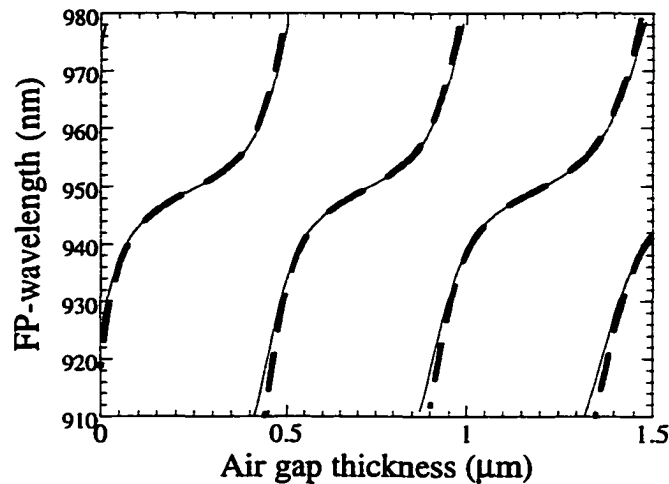
Figure 2.13 FP-wavelength plotted against air gap thickness for the two very similar VCSEL structures shown in table 2.3 above
Solid line shows the resonant wavelength for the AlGaAs movable mirror while the dashed line indicates the case for the ZeSn/MgF$_2$ dielectric mirror. The bottom DBR for both structures is the same, given in table 2.2.

One can see that the air-gap dependent tuning curve is very similar for the two cases. In fact, except at the edges of the plotted range (around 910nm and 980nm), the two lines lie right on top of each other. This result is not surprising. The resonant wavelength of a tunable VCSEL structure is dominated by the DBR with a smaller Δn.

41

From figure 2.2(b), the reflected phase of a low contrast (Δn) DBR varies more rapidly with wavelength than a DBR with a large Δn. In our example above, the AlGaAs DBR is the limiting factor. But since the bottom DBR for both structures in figure 2.13 is already an AlGaAs DBR (see table 2.2), a dielectric movable DBR won't boost the tuning range. Therefore, unless one decides to abandon low-Δn semiconductor DBRs altogether for a tunable VCSEL, not much of an advantage can be gained by adopting only one broadband mirror to increase the tuning range.

In addition, there are three shortcomings to the use of dielectric mirrors. Since each reflection off a dielectric interface in a DBR is so strong, it does not take very many interfaces to reach a high target reflectivity of 99.9%. This is advantageous only if a high reflector is desired. But what if we wanted a reflector that could effectively couple useful amounts of the internal field to the outside world instead? Then the dielectric DBR may not be appropriate. For example, while 6.5 pairs of material in a dielectric DBR yield an ultra high reflectivity of 99.95%, paring down the number of layers by two to only 5.5 pairs would give a lower power reflectance of 99.83%. This might not seem much when we look at the *power reflectance*. However, if we consider the transmitted power through this DBR stack, i.e. one minus the power reflectance, we see a 227% increase in the transmitted power from a 5.5 pair stack compared to a 6.5 pair stack! In the case of the semiconductor DBR, decreasing the stack by one pair from 20.5 pairs to 19.5 pairs yields an increase in the transmitted power of only 29%. This more gradual rate of change in transmission is manageable, especially for output couplers. Illustrated in figure 2.14 is the power reflectance of normal incident plane waves onto the same two kinds of DBR shown in table 2.3, as a

42

function of the number of layers in each DBR. From the slope of each curve in figure 2.14, we can see that while the ZnSe/MgF$_2$ DBR's reflectivity increases by an order of magnitude about every 2 pairs, that from the AlGaAs DBR does so much more gradually at a rate less than one decade every 9 pairs.
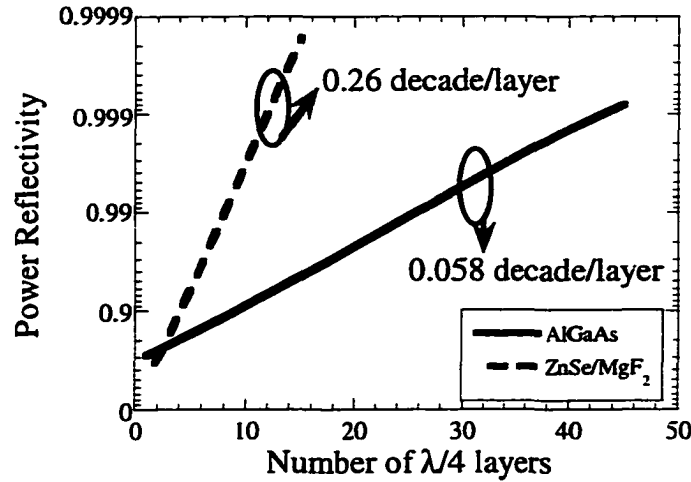
Figure 2.14 Power reflectance of normal incident plane waves onto the two DBRs listed in Table 2.3
The power reflectance at the center wavelength of 950nm is plotted against the number of layers in each respective DBR stack. Solid line indicates the Al$_x$Ga$_{(1-x)}$As (x=0.1,0.9) while dashed line indicates ZnSe/MgF$_2$ DBR. Both the incident and exit media of the DBR have refractive index of 1(air).

We can get an idea how the reflectance of a mirror affects the output power from one mirror (labeled 1, the other mirror is labeled 2) with the following relationship:[5]

$$P_1 = \frac{t_1^2}{\left(1 - r_1^2\right) + \frac{r_1}{r_2}\left(1 - r_2^2\right)}.$$

(2.9)

t_i^2 and r_i^2 are related such that power conservation holds for each mirror (i=1,2), i.e. the sum of its reflection, transmission and absorption is unity:

$$r_i + t_i + \alpha_i = 1.$$

(2.10)

From a practical standpoint, the output power required by a specific application may place a ceiling on the maximum reflectivity allowed of the output coupler. Unless the tunable VCSEL is bottom-emitting, the use of a dielectric DBR as the top movable mirror could present some difficulties.

The second drawback to dielectric DBRs is their electrical insulating nature. The dielectric mirror shown in table 2.3 is not fully realizable in a tunable VCSEL because an electrically conducting contact layer has to lie underneath the dielectrics to electrostatically effect motion for the whole stack. Therefore, a layer of semiconducting material is necessary in the movable mirror stack anyway. The third disadvantage is a fabrication issue. Deposition accuracy of dielectric materials cannot be monitored as closely as the growth of epitaxial layers, making the process extremely difficult to control, low-yield, and difficult to reproduce. All these reasons cited above limit the use of the dielectric DBR in the tunable VCSEL structure because it undermines both device fabrication and flexibility of device performance.

C   Physical limit to tuning range

In the two previous sections, tuning curves were given as functions of air gap thickness. Provided that large enough gain over the relevant wavelength span is available, every possible wavelength should be accessible. Where two solutions exist for the same air gap size, the mode that sees the larger gain would dominate. This process sounds fairly simple, at least on paper. Furthermore, from figure 2.12 it appears that all the available wavelengths within the tuning range can be reached with the air gap thinner than 4800Å (approximately half of the center wavelength, which is 950nm). Perhaps the question of why we would care to plot over the region where the

44

air gap thickness is greater than 4800Å has crossed the reader's mind. As it turns out,

not all of the air gap thickness is realizable. Subsequently not all wavelengths plotted

in figures 2.12 and 2.13 are accessible. In this section, we will give a physical picture

to the limit placed on this realizable air gap range as well as the compromise this limit

presents us in the design of a tunable VCSEL.

Let us first examine the electrical and mechanical forces involved in a tunable

VCSEL structure such as ours. Illustrated in figure 2.15 is a schematic that includes

the variables involved in our discussion below. These definitions are given in table

2.4 as well.
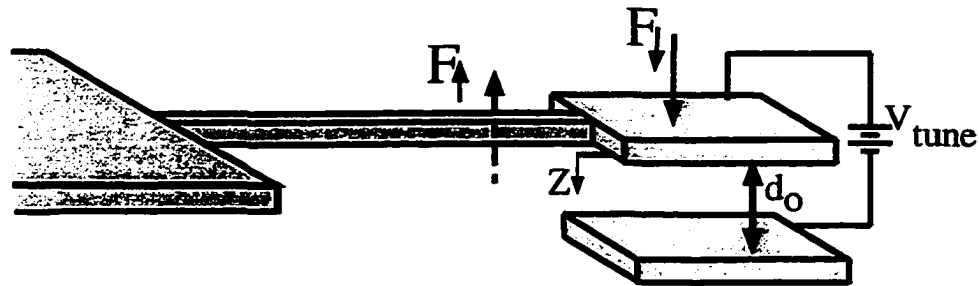
Figure 2.15 Force diagram in a tunable VCSEL
The definitions of the labeled variables in this figure are listed in table 2.4 below.

Variable	Definition/Explanation
$F_\downarrow$	Electrostatic attractive force that pulls the movable section down
E_{cap}	Stored energy in capacitor
C	Capacitance
V	Voltage applied across capacitor plates
z	Variable in z-direction, perpendicular to capacitor plates
d_o	Initial separation of the capacitor plates (without any applied bias)
ε	Permittivity of material between capacitor plates ($=\varepsilon_o$ in this case)
A	Area of one capacitor plate (assume symmetric)
$F_\uparrow$	Mechanical restoring force for the movable section that pulls it back up
k	Spring constant of the movable section, geometry dependent

Table 2.4 Definitions and explanations of variables shown in figure 2.15

In terms of the electrostatic forces in a capacitor, one could derive the attractive force that a plate experiences towards the other from the stored energy in a capacitor, neglecting any fringing fields:

$$F_{\downarrow} = \frac{\partial}{\partial z}(E_{cap}) = \frac{\partial}{\partial z}\left[\frac{CV^2}{2}\right] = \frac{\partial}{\partial z}\left[\frac{\varepsilon A V^2}{2(d_0 - z)}\right]. \qquad (2.11)$$

If we bear in mind that the applied voltage is actually a function of z as well, (2.11) seems very complex and difficult to solve. For a clear physical picture, we would disregard the dependency V(z) for now and assume that V is independent of z. Equation (2.11) would then be:

$$F_{\downarrow} = -\frac{\varepsilon A V^2}{2(d_0 - z)^2}. \qquad (2.12)$$

The mechanical restoring force within the mechanical structure tends to pull the movable section back to its unperturbed state and acts as the counterbalancing force against the downward electrostatic attraction. For small perturbations, this upward force can be modeled with a linear spring constant:

$$F_{\uparrow} = -kz. \qquad (2.13)$$

Note that in our notation the z-axis points downward and that its origin rests at the movable mirror in its unperturbed state. The negative signs in front of the expressions in (2.12) and (2.13) can be neglected as long as we keep track of the positive sense for each force.

For a finite applied voltage V_0, if we plot the magnitude of both $F_{\downarrow}$ and $F_{\uparrow}$ against the z-variable, we would get a branch of a hyperbola for $F_{\downarrow}$ (see (2.12)) and a straight line for $F_{\uparrow}$. For a different applied voltage $V_1 > V_0$, the hyperbola for $F_{\downarrow}$

46

would shift upward while the straight line for $F_\uparrow$ remains the same because this

upward force is mechanical in origin and not dependent on the applied voltage across

the capacitor. In this fashion, we could construct a family of curves for different

applied voltages: $V_o<V_1<V_2<...$, etc. Such a family of curves for $F_\downarrow$ as well as the

straight line (for an arbitrary k) for $F_\uparrow$ is shown in figure 2.16.
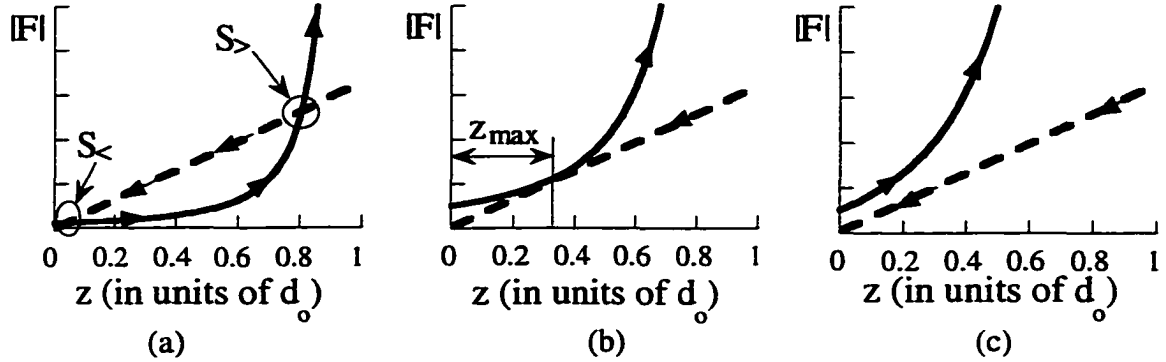
Figure 2.16 $F_\uparrow$ and $F_\downarrow$ plotted against the displacement variable z

In this series of figures, $F_\downarrow(z)$ is shown in the solid line while $F_\uparrow(z)$ is indicated in the dashed line. It should be noted that $F_\downarrow(z)$ acts in the positive z-direction. Thus the arrows associated with this force are pointing to the right. And $F_\uparrow(z)$ acts in the negative z-direction. The arrows associated with the dashed curve are all pointing to the left. At any z-value, the force with the larger magnitude would push the cantilever head in its direction. So in (a), for $V<V_c$, two solutions $S_>$ and $S_<$ exist. Both are shown, but only one of them in (a) is stable. (b) For $V=V_c$, $S_>$ and $S_<$ have merged into a single solution at z_{max}. (c) For $V>V_c$, the two forces don't intersect. There is no solution.

The cantilever head will rest at the z-value where the two opposing forces are

equal in magnitude. From figure 2.16, for applied biases less than some critical value,

V_c, the two opposing forces have two intersections. At $V=V_c$, the two intersections

merge into one, and for $V>V_c$, no solution exists. This seems to suggest that two

solutions exist for $V<V_c$. First of all, let's call the solution that occurs at the smaller

value of z $S_<$ and the other $S_>$. Now let us examine the region to the right of $S_>$: For

$z > S_>$, $|F_\downarrow| > |F_\uparrow|$. The cantilever would move to the right along the direction of $F_\downarrow$

47

until it is stuck at the substrate.[6] Following the same line of logic in examining the region to the left of $S_>$, we would find that $|F_\uparrow| > |F_\downarrow|$ there and conclude that $S_>$ is quite impossible to reach as a solution from the left as well. Therefore, $S_>$ is simply an unstable equilibrium from a mathematical standpoint.

That is the bad news. The good news is that $S_<$ is a stable equilibrium solution. We can reach this conclusion by following a similar line of reasoning for the regions to the left and to the right of $S_<$. In both regions, the dominant force is in the direction such that the movable plate is pulled towards $S_<$. Thus $S_<$ is truly stable and the observed solution in our experiments.

Because $S_>$ is an unstable operating point, the movable plate cannot reach certain z-values. We are now interested in finding the maximum z-value which the movable plate can travel. This z-value will ultimately present the limit of the tuning range in the tunable VCSEL.

From figure 2.16(b), we see that for $V > V_c$, no stable equilibrium exists. This would imply that V_c is the applied voltage at which the z-value for $S_<$ is maximized. Simple calculus has us solve the following two equations for this maximum z-value which we denote z_{max} below:

$$|F_\downarrow(z_{max})| = |F_\uparrow(z_{max})|; \qquad (2.14a)$$

$$\frac{\partial}{\partial z}|F_\downarrow(z)|_{z_{max}} = \frac{\partial}{\partial z}|F_\uparrow(z)|_{z_{max}}. \qquad (2.14b)$$

Plugging (2.12) and (2.13) into (2.14) and letting $V=V_c$, these two equations become:

---

[6] Due to our previous definition of the origin and direction of the z-axis, an increase in z indicates a decreased separation between the two plates. The maximum z-value is d_0 since the separation cannot be negative.

$$\frac{\varepsilon A V_c{}^2}{2(d_o - z_{max})^2} = kz_{max}; \text{and} \tag{2.15a}$$

$$\frac{\varepsilon A V_c{}^2}{(d_o - z_{max})^3} = k. \tag{2.15b}$$

Substituting the expression for k in (2.15b) into (2.15a), crossing out like terms, and simplifying the resultant expression further, we arrive at the answer:

$$2z_{max} = d_o - z_{max}; \text{thus}$$
$$z_{max} = \frac{d_o}{3}. \tag{2.16}$$

Note that the result of (2.16) is completely general: z_{max} is independent of k and thus also of geometry. The only assumptions we've made are that V is independent of z and that the restoring force is linearly proportional to displacement. We shall see later on that this "one-third" rule, as we will call it, holds even when the z-dependence of V is considered in the case of deformable solids.

Equation (2.16) tells us that only about a third of the original air gap thickness can be accessible by the movable mirror. It is certainly undesirable that two thirds of the plots in figures 2.12 and 2.13 is unusable. This physical limit to the tuning range forces us to incorporate an air layer that is three times longer than what we actually want. Since the longer air layer makes for a longer cavity and a shorter free spectral range, a narrower tuning range results. In chapter six, our analysis will show that this physical limit placed on the minimum air gap thickness represents a design tradeoff between tuning range and some key performance figures of merit when comparing our tunable VCSEL to a conventional VCSEL.

49

V   Wavelength-dependent properties

Now that we have gone over the tuning range limit of the mechanical tunable VCSEL, the next step is to include a discussion on how the performance of such a VCSEL is varied across this wavelength range. Ideally, one would want uniform performance figures of merit such as threshold current and output power over as much of the entire tuning range as possible. However, reality dictates that both the mirror reflectivity and gain spectrum be wavelength-dependent. These dependencies should be considered in optimizing performance uniformity across most of the tuning spectrum for the tunable VCSEL.

A   Gain confinement factor

In section II B, the discussion on gain in a VCSEL briefly alluded to a quantity called the modal gain, $\Gamma_{xy}\Gamma_z g$. Γ_{xy} is relatively constant across the tuning range since a VCSEL's transverse mode is defined by the fabrication process. In a tunable VCSEL such as ours where only one mirror moves, Γ_z as defined in (2.5) would not be constant with wavelength. Illustrated in figures 2.17(a) and (b) are the calculated longitudinal field distributions of a tunable VCSEL's FP-wavelength with the air gap at the resonant and anti-resonant conditions, respectively.

50
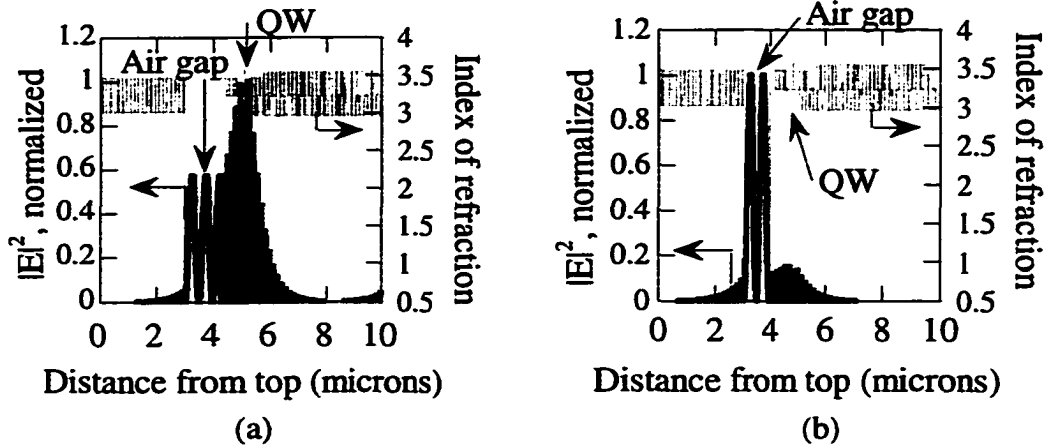
Figure 2.17 Field distribution in the cavity of a tunable VCSEL at two different air gap thicknesses

The field distribution is critically dependent on the thickness of the air layer. Shown here is the longitudinal standing wave pattern superposed on the physical layers of the structure, with the topmost layer on the left side and the GaAs substrate to the right. The air gap is the thick layer shown above with index = 1. The location of the quantum wells within the VCSEL has been denoted with QW above as well. In (a), the air gap is at the resonant condition so that the FP-wavelength of the structure is 950nm. In (b), the air gap is antiresonant with the rest of the structure that the FP-wavelength is 931nm. Notice the amount of field present in the air gap relative to that in the QW region is drastically different in these two cases.

Comparing the amount of field in the air gap, we can see that the field distribution is drastically different when the FP-wavelength is at the center wavelength of the structure, as in figure 2.17(a), and when it is only offset by about 20nm as shown in figure 2.17(b). Γ_z in equation (2.5) is the quantitative measure of how well overlapped the intracavity field is with the gain region. Plotted in figure 2.18 is Γ_z as a function of the air gap thickness. It can vary by a factor of two over the tuning span. From this figure, yet another disadvantage of the one third tuning limit found in (2.16) is quite obvious: The longer the air gap, the smaller is Γ_z and the harder the gain region has to be pumped to achieve a comparable modal gain, $\Gamma_z g$.

51
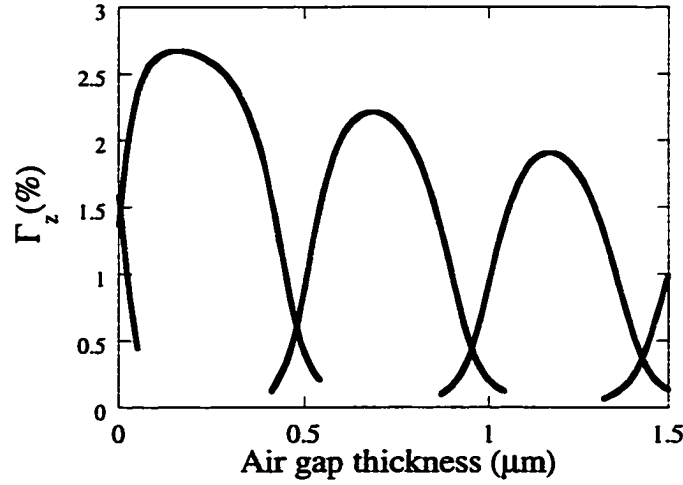
Figure 2.18 Γ_z as a function of the thickness of the air gap

Γ_z steadily decreases with increasing air gap thickness due to the increasing amount of field occupying the thicker air gap. The different humps here represent adjacent longitudinal FP-modes.

B   Mirror loss

We have seen in figure 2.3 of section I that the reflectance of a DBR is wavelength-dependent. Following the same train of thought, we find the power reflectance of the mirrors in the two structures showcased in table 2.3 and take the magnitude squared of (2.7) to get:

$$\left| r_{top}(\lambda, d_{air}) r_{bottom}(\lambda) \right|^2 = e^{G_{rt} - \alpha_{mirror}}, \tag{2.17}$$

where G_{rt} is the roundtrip power gain and α_{mirror} is the roundtrip power loss through the non-unity reflectance of the two DBRs. Since we are specifically interested in the wavelength-dependent α_{mirror} term, we now set G_{rt} to zero and find the following expression for α_{mirror}:

$$\alpha_{mirror} = -2\ln\left[\tilde{r}_{top}(\lambda, d_{air}) \tilde{r}_{bottom}(\lambda)\right] \tag{2.18}$$

Shown in figure 2.19 is the roundtrip power loss (in percent) through the mirrors in the two VCSEL structures listed in table 2.3. Note that the results have already taken into account the change in air gap thickness and FP-wavelength shift.

52
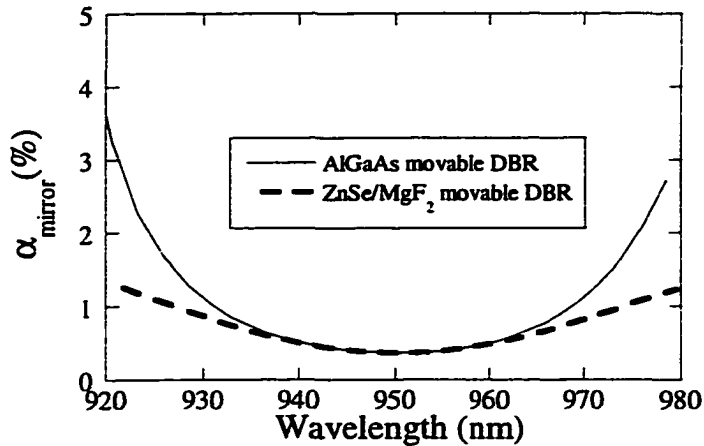
Figure 2.19 $\alpha_{mirror}(\lambda)$ **for two tunable VCSEL structures employing different movable DBRs**

The solid line indicates the roundtrip mirror loss for the entirely AlGaAs structure listed in table 2.3 while the dashed line shows α_{mirror} for the other that contains a movable, top dielectric DBR. As expected from the results shown in figure 2.13, the only significant difference between these two is the loss towards the edges of the tuning spectrum. Thus, employing a dielectric movable section is useful when the free spectral range is broad. This would require that both DBRs be dielectric.

Employing the dielectric DBR can lower the overall mirror loss at the edges of the tuning spectrum. This is useful when the VCSEL's free spectral range (FSR) is wide enough to cover the bandwidth where the AlGaAs DBR begins to decrease in its reflectivity. However, as discussed in section IV B, the FSR is critically limited by the DBR that has the narrower reflection bandwidth. Therefore, the advantage of using a dielectric DBR is realized only if both DBRs are dielectric. Furthermore, accurate e-beam evaporation of dielectrics, in practice, is difficult to achieve in terms of thickness and refractive index control. From our ensuing discussion surrounding figure 2.14, output power level also varies drastically with the number of layers in dielectrics. Thus, quite a few obstacles have to be overcome before the use of dielectric DBRs can realize enhancement in a tunable VCSEL's performance.

C   Gain

In section A, the longitudinal gain confinement factor Γ_z was shown to vary as the cavity is shortened. Throughout that discussion, the wavelength dependence of the material gain, denoted simply by g in the previous discussion, was not mentioned. As it happens, material gain in quantum wells is constant neither with wavelength nor with current density. For a thorough discussion of gain spectra in InGaAs or GaAs quantum wells, the reader is referred to [5] and [19].

Although the gain picture is more complicated now, the fact that g is not constant with wavelength is actually a blessing in disguise. We could use $g(\lambda)$ to compensate for $\Gamma_z(\lambda)$ so that the quantity $\Gamma_z g$ remains relatively constant with wavelength. This can be gleamed by explicitly expressing the wavelength dependence of g and $\psi(z)$ in equation (2.5):

$$\Gamma_z g = \frac{g(\lambda) \int\limits_{QWs} \Psi^*(\lambda, z)\Psi(\lambda, z)dz}{\int\limits_{-\infty}^{\infty} |\Psi(\lambda, z)|^2 dz}.$$

(2.19)

Achieving a more uniform modal gain over a wide spectral range involves the strategic placement of quantum wells with different widths (and thus different gain peak wavelengths) in the cavity such that the overlap of $\psi(\lambda,z)$ and $g(\lambda,z)$ is optimized for spectral uniformity. This scenario is sketched in figure 2.20 below. For detailed gain calculations and a thorough discussion, the reader is referred to [17].
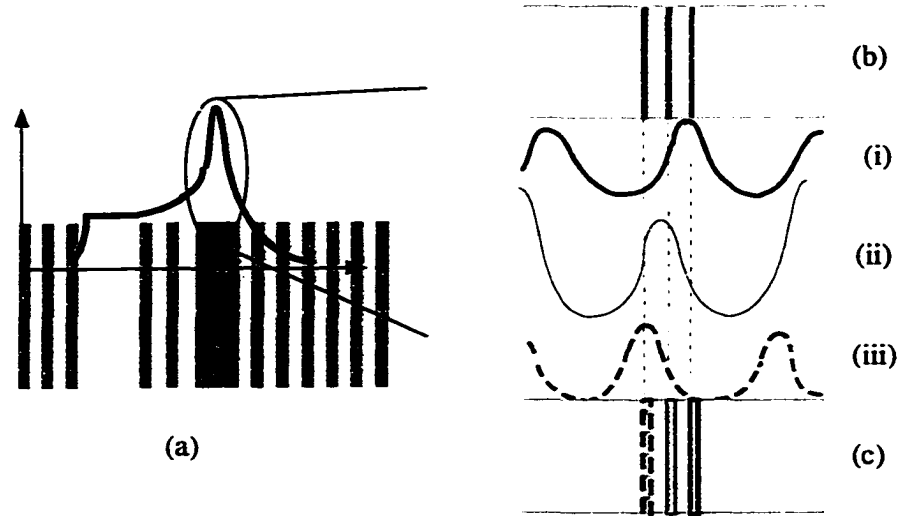
Figure 2.20 Strategic placement of quantum wells with different gain peaks in the cavity

(a) The overall standing wave envelope superposed onto the tunable VCSEL structure. The envelope of the standing wave pattern in the cavity region is magnified in lines (i), (ii), and (iii) for three air gap thicknesses (and three FP-wavelengths). In (b), all three quantum wells depicted are identical. In (c), the three quantum wells are such that each has its peak gain at a different wavelength. As the standing wave pattern $\psi(z)$ shifts from (i) to (iii) for an increasing air gap thickness, the appropriate quantum well would cater to each $\psi(z)$ that gain at the appropriate wavelength be supplied. This scheme is advantageous in that when the standing wave pattern shifts during tuning of our structure, the appropriate slice of the gain bandwidth is excited.

VI   Summary

A lot of ground has been covered in this chapter. Some basic concepts in the design of a conventional VCSEL were first discussed. This includes considerations for the mirrors and the cavity. The principle of operation for the tunable VCSELs is covered. Fundamental differences between a conventional VCSEL and a tunable VCSEL in terms of their optical, electrical and epitaxial structures as well as some fabrication issues were elaborated. Several design examples have been offered to outline the effects of the reflectivity in the p-DBR stack and different DBR materials have on the tuning range. A zeroth order analysis has been put forth to give the one-third rule that limits the tuning range for electrostatic tuning. We further quantify wavelength-dependent variables like $\alpha_{mirror}(d_{air})$ and $\Gamma_z(d_{air})$ in a tunable VCSEL and

55

outline means of achieving uniform wavelength performance in such a device.

Through these examples and comparisons, we hope that the reader gains a sense of the

performance tradeoffs when the different choices of materials and doping schemes are

employed in the final design of a tunable VCSEL structure.

VI   References

[1]   M. S. Wu, E. C. Vail, G. S. Li, W. Yuen, and C. J. Chang-Hasnain, "Tunable micromachined vertical cavity surface emitting laser," *Electronics Letters*, vol. 31, pp. 1671-2, 1995.

[2]   M. C. Larson, A. R. Massengale, and J. S. Harris, Jr., "Continuously tunable micro-electromechanical vertical-cavity surface-emitting lasers," *International Journal of Optoelectronics*, vol. 10, pp. 401-8, 1995.

[3]   M. Born and E. Wolf, *Principles of Optics*, Sixth (corrected) ed. New York: Pergamon Press, 1980.

[4]   A. Yariv and P. Yeh, *Optical Waves in Crystals*. New York: John Wiley & Sons, 1984.

[5]   L. A. Coldren and S. W. Corzine, *Diode Lasers and Photonic Integrated Circuits*. New York: John Wiley & Sons, Inc., 1995.

[6]   E. Hecht and A. Zajac, *Optics*, Second ed. Menlo Park: Addison-Wesley, 1987.

[7]   E. C. Vail, M. S. Wu, G. S. Li, L. Eng, and C. J. Chang-Hasnain, "GaAs micromachined widely tunable Fabry-Perot filters," *Electronics Letters*, vol. 31, pp. 228-9, 1995.

[8]   M. S. Wu, E. C. Vail, and C. J. Chang-Hasnain, "Widely tunable micromachined optical filters," presented at Summaries of the Papers Presented at the Topical Meeting, Integrated Photonics Research. 1996 Technical Digest Series. Vol.6 Proceedings of Integrated Photonics, Boston, MA, USA, 1996.

[9]   M. S. Wu, G. S. Li, W. Yuen, and C. J. Chang-Hasnain, "Widely tunable 1.5 mu m micromechanical optical filter using AlO/sub x//AlGaAs DBR," *Electronics Letters*, vol. 33, pp. 1702-4, 1997.

[10]   M. S. Wu, E. C. Vail, G. S. Li, L. Eng, and C. J. Chang-Hasnain, "Speed and polarization characteristics of widely tunable micromachined GaAs Fabry-Perot filters," presented at Summaries of Papers Presented at the Conference on Lasers and Electro-Optics IEEE Cat. No. 95CH35800 CLEO '95. Conference on Lasers and Electro-Optics. papers in summary form only received, Baltimore, MD, USA, 1995.

[11] G. Hasnain, K. Tai, L. Yang, Y. H. Wang, R. J. Fischer, J. D. Wynn, B. Weir, N. K. Dutta, and A. Y. Cho, "Performance of gain-guided surface emitting lasers with semiconductor distributed Bragg reflectors," *IEEE Journal of Quantum Electronics*, vol. 27, pp. 1377-85, 1991.

[12] J. I. Pankove, "Chapter 3 Absorption," in *Optical Processes in Semiconductors*. New York: Dover Publications, Inc., 1971.

[13] D. I. Babic, Y. Chung, N. Dagli, and J. E. Bowers, "Modal Reflection of Quarter-Wave Mirrors in Vertical-Cavity Lasers," *IEEE Journal of Quantum Electronics*, vol. 29, pp. 1950-1962, 1993.

[14] S. F. Lim, J. A. Hudgings, L. P. Chen, G. S. Li, Y. Wupen, K. Y. Lau, and C. J. Chang-Hasnain, "Modulation of a vertical-cavity surface-emitting laser using an intracavity quantum-well absorber," *IEEE Photonics Technology Letters*, vol. 10, pp. 319-21, 1998.

[15] S. F. Lim, G. S. Li, W. Yuen, and C. J. Chang-Hasnain, "Intracavity resonant quantum-well photodetection of a vertical-cavity surface-emitting laser," *Electronics Letters*, vol. 33, pp. 597-8, 1997.

[16] J. W. Scott, R. S. Geels, S. W. Corzine, and L. A. Coldren, "Modeling temperature effects and spatial hole burning to optimize vertical-cavity surface-emitting laser performance," *IEEE Journal of Quantum Electronics*, vol. 29, pp. 1295-308, 1993.

[17] W. Yuen, "Multiple wavelength vertical cavity surface emitting laser arrays for high speed local area networks," in *Electrical Engineering*. Stanford, CA, USA: Stanford University, 1999.

[18] G. S. Li, "Wavelength Selective Detectors for Fiber Optic Communications," in *Applied Physics*. Stanford, CA, USA: Stanford University, 1998, pp. 130.

[19] J. Singh, *Physics of Semiconductors and Their Heterostructures*. San Francisco: McGraw-Hill, Inc., 1993.

Device Fabrication

Fabrication of the tunable VCSELs has evolved to be quite an elaborate process that this chapter is specifically devoted to the various processing issues involved to realize the final device. An overview of the process steps is first given. The critical steps will then be detailed in the following sections. In addition, design constraints for the layout geometry and process parameters will also be presented.

I   Fabrication steps

Summarized in figures 3.1 and 3.2 is the flow of the process steps taken to turn a bare wafer fresh from the MBE into a working tunable VCSEL. Although the 3D-schematic of a tunable VCSEL back in figure 2.6(a) may seem very complicated, the actual fabrication is surprisingly simple, involving four masks and only one critical alignment step. Shown in figure 3.1 below is the procedure involving the first three masks. The cross section view in each step is shown in the left column while the view from the top of the VCSEL wafer is in the right column.

Shown in figure 3.1(a) is the first lithography step that defines the contact pad for the tuning bias. This is followed by metal evaporation on the n-doped contact layer using nickel, germanium, and gold. After liftoff and annealing of the metal, a

second photolithography step defines the cantilever. In-situ monitoring is used during the ensuing SiCl₄ reactive-ion etch (RIE) to carve out the cantilever shape until the GaAs sacrificial layer is exposed.

(a)

(b)
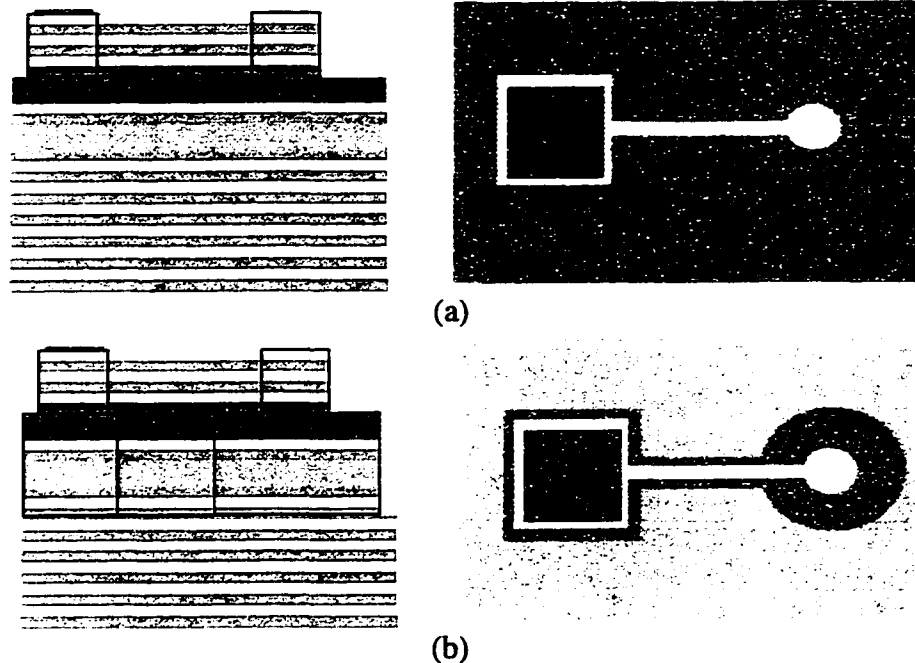
Figure 3.1 Fabrication steps of the tunable VCSEL involving the first three masks

(a) The first step is simply the lithography of the tuning contact, denoted as the dark square from the top view on the right hand side. After metal evaporation and liftoff, the cantilever is defined. A reactive ion etch (RIE) follows to carve out the cantilever until the sacrificial layer is exposed. This is shown as the background in the top view. In (b), another lithography step follows to define the VCSEL mesa to provide device isolation. Another RIE follow to expose the AlAs layer for oxidation.

After removal of the photo-resist from the cantilever definition step, another lithography follows. A thicker photo-resist (~3μm) is used at this time to define the base mesa over which the cantilever hovers. This presents the only critical alignment step throughout the entire fabrication process. Again the sample is carved using a vertical SiCl₄ etch in the RIE chamber until the AlAs layer is exposed. This layer is to be exposed so that after having been oxidized laterally, the resultant layer becomes an aluminum-oxide ring that acts as a current confinement region surrounding an

59

unoxidized AlAs region in the center. This process is discussed further in section III below.

Upon removal from the ultra high vacuum of the etch chamber, the thick photoresist is immediately removed and the sample cleaned before it is inserted into the oxidation furnace at 425°C. After a calibrated amount of oxidation duration that yields unoxidized AlAs regions, which we call apertures, less than 10μm across, the sample is removed from the furnace.

(a)

(b)
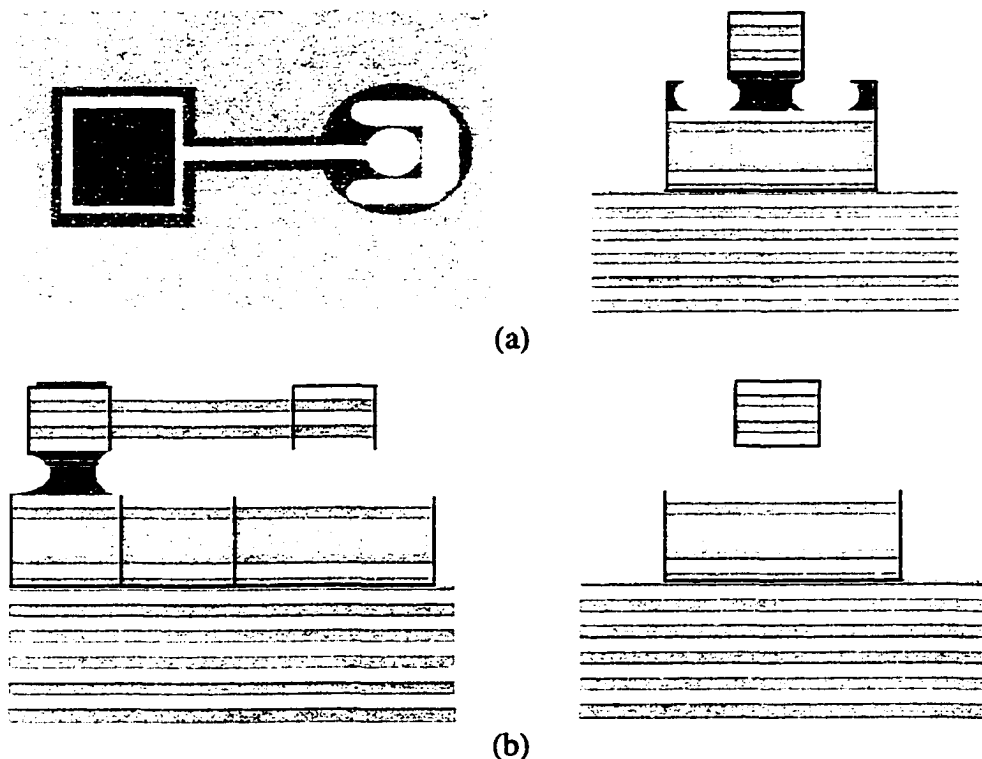
Figure 3.2 Fabrication steps of the tunable VCSEL involving the last mask
(a) After oxidation, another lithography step is necessary to define the contact through which current is injected. A selective etch is used to etch off the exposed GaAs until the AlGaAs contact layer underneath is exposed. Metal contacts are subsequently evaporated. After liftoff of the contact metals (b), a final selective etch is used to release the cantilever beam from the mesa.

After oxidation, another thick lithography step defines the contact pad for the pump region. At this time, the sample is inserted into the RIE chamber again. However, a small amount of SF_6 is added into the predominantly $SiCl_4$ gas mixture.

60

This GaAs-selective etch removes the exposed GaAs but leaves any exposed AlGaAs surface intact. A more thorough discussion of this GaAs-selective etch follows in section IV.

When the entire p-doped AlGaAs contact area is exposed, the sample is removed from the RIE chamber and evaporated with titanium and gold. See figure 3.2(a). After liftoff of this p+ contact, the sample is reinserted into the RIE chamber to have most of the GaAs sacrificial layer removed (except for the area underneath the anchor). This concludes the entire fabrication process of the tunable VCSEL.

Having summarized the entire procedure, it is important for us to include the details associated with the steps outlined above. Specifically, parameters or setups that are deemed unusual for device fabrication with III-V compounds are discussed. In the following sections, the in-situ monitoring of etch rates, the AlAs oxidation, the GaAs-selective etch, and a critical point drying step are elaborated upon. Scanning electron micrographs of the finished tunable VCSELs are also shown at the end of this chapter.

II In-situ etch monitor

In-situ monitoring of etch depths turns out to be a significant time- and sample-saver. Not only are the etch rates for GaAs, AlAs and AlGaAs different from one another, but they are also temperature-dependent. Therefore, precise control of etch depths in a VCSEL structure is normally very difficult. An in-situ monitor setup takes the guesswork out of etching. Rather than taking the sample out of the RIE chamber once every few minutes to check the etch depth, it can be monitored in real time and controlled to within 2000Å. An added advantage is that the vacuum is never broken

throughout the entire process. This is especially important because in our VCSEL

structure, layers with high aluminum content like AlAs easily react with air.

Premature exposure to air and moisture would pose problems for process

reproducibility and ultimately compromise device performance.

Installation of an in-situ etch monitor system is quite straightforward. The

only requirement is that the sample has to be multi-layered and optically reflective that

interference fringe patterns emerge and change as the topmost layer is removed.

Figure 3.3 below is a schematic of the homemade [1] in-situ etch monitor system we

have at the micro-fabrication facilities at UC Berkeley.
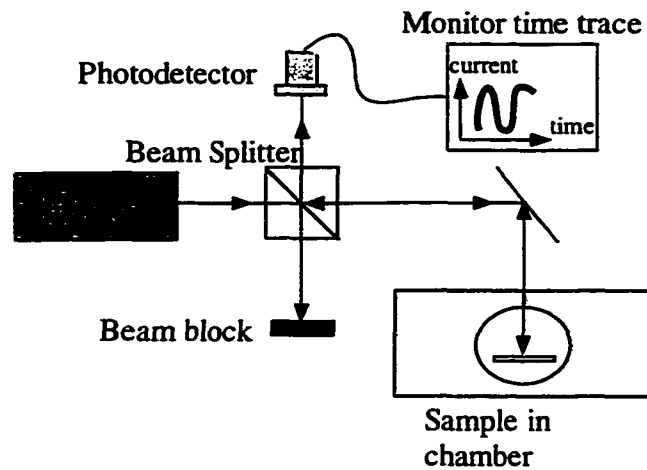
Figure 3.3 In-situ etch etch monitor setup
A HeNe beam impinges on and is reflected from the surface of the etch sample. The
reflection is monitored by a photodetector. The photodetector current is continuously
monitored. The resultant time trace of the photo-detector current shows the etch
depth in real time.

A Helium-Neon (HeNe) laser beam impinges on the sample through a window

in the RIE chamber. Very much after the fashion of light impinging upon a DBR, the

beam is then reflected. After a beam splitter directs this reflected beam past an iris to

separate it from other spurious reflections in the system, a photodetector picks up the

intensity of the reflected beam. Shown in figure 3.3 is the etch signature of an entire
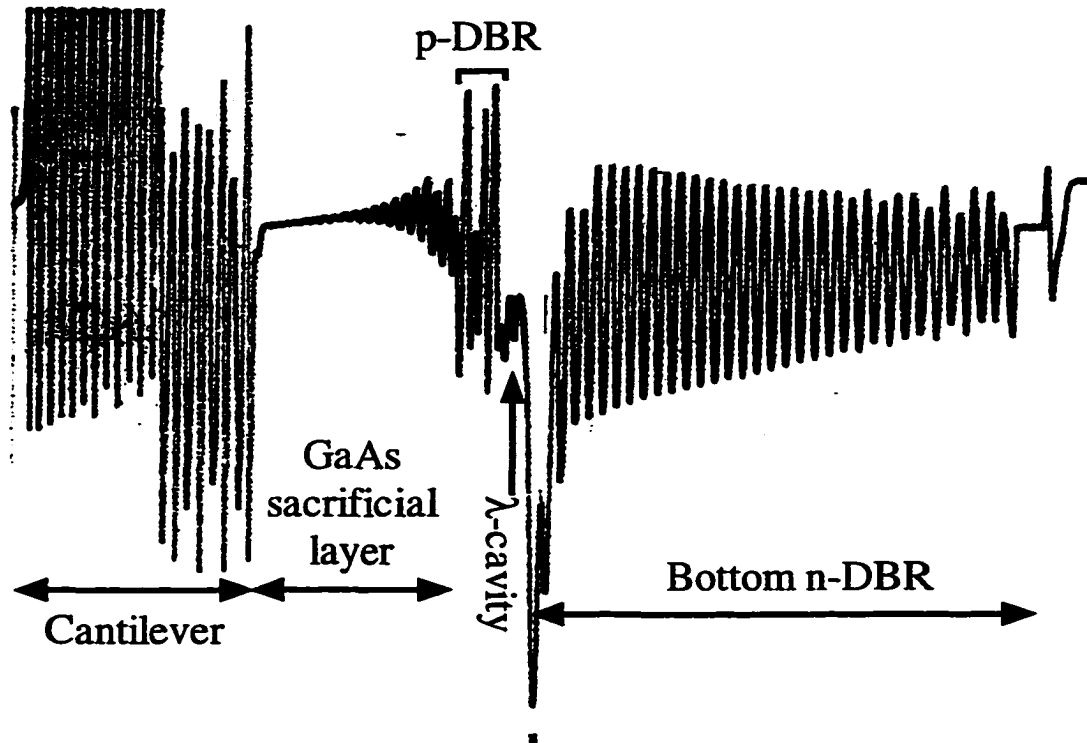
tunable VCSEL.

Figure 3.4 Etch signature of an entire tunable VCSEL structure
The various sections within the tunable VCSEL structure in figure 2.11 are well delineated. For the cantilever definition step shown in figure 3.1(a), this etch is stopped when the plateau at the GaAs sacrificial layer is reached.

It is surprising how closely the tunable VCSEL's etch signature follows the device structure despite the fact that the HeNe beam should see depths of only a few layers at any time. Each period of high and low undulation in the signature represents one DBR pair consisting of a high index and a low index AlGaAs layer. Also noteworthy is the obvious signature indicating when the sacrificial layer is reached. The plateau from the exposure of the GaAs sacrificial layer helps tremendously in determining when to stop the first vertical etch in figure 3.1. As to when the second vertical etch should stop, it is less obvious. After a piece of the wafer has been completely etched and the signature of the wafer obtained, we can count from the substrate back up towards the cavity to deduce the signature of the AlAs oxidation layer. Once the signatures of both the sacrificial layer and the AlAs oxidation layer

63

are in place, accurate etching in a tunable VCSEL is easily achievable to within a DBR pair (~2000Å).

III   Lateral oxidation

Lateral oxidation of a thin AlGaAs layer with high aluminum concentration (usually > 95%) into aluminum oxide (Al_xO_y) takes place in the super saturated water-vapor ambience of a 400°C furnace. Shown in figure 3.5 is how the converted Al_xO_y acts as a current blocking layer for the injection current.
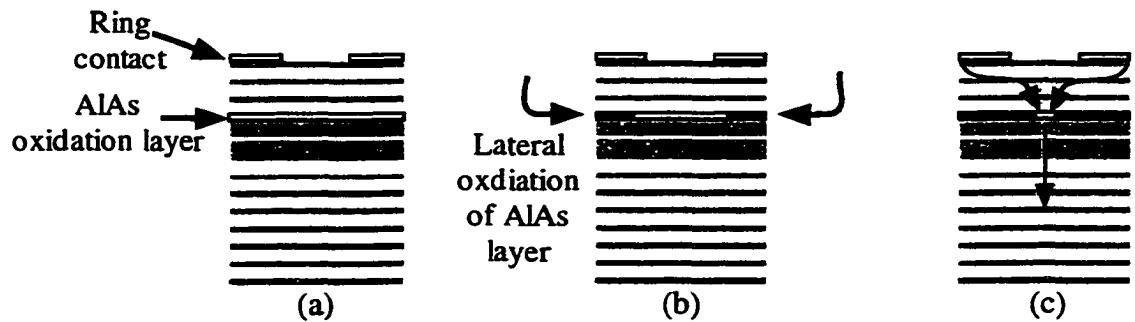
Figure 3.5 Lateral oxidation of high aluminum-content AlGaAs layers
(a) An as-grown VCSEL structure with a high aluminum content AlGaAs layer (shown as AlAs in this figure); (b) Under a high temperature (~400°C) and super-saturated water vapor ambience, the exposed outer ring of the AlAs layer is converted into aluminum oxide (Al_xO_y) in a lateral oxidation process. (c) The resultant Al_xO_y ring keeps the injected current confined in the center region where the unconverted AlAs layer can still conduct current. The unconverted AlAs region in the center is called the oxide aperture.

In many ways, oxidation is a perfect way to define the transverse dimensions of the VCSEL structure, especially since it is highly non-planar (the cantilever section stands some 4μm above the p+ current injection contact). At the same time a laser with transverse dimensions much smaller than the width of the cantilever head (~20μm wide) is desired. Thus a buried mode-confining region formed from the side rather than one formed from the top is preferred. Other than providing more effective electrical pumping of the laser, the oxide aperture also provides lateral optical guiding of the optical mode. This is because Al_xO_y has a much lower refractive index (n~1.55

64

in the near infrared) than the unconverted AlAs (n~3.0) so that the optical mode stay confined to the center region, very much after the fashion of an optical fiber as a waveguide.

Unlike the RIE etch, real-time monitoring of the oxidation rate is not as easily implemented due to the hot (>400°C) and steamy[1] (water vapor saturated) environment in which the process takes place. Timed calibration tests are used to determine the oxidation rate for each wafer. This rate is dependent on several factors: the temperature in the furnace, as well as the thickness, aluminum composition, and surface treatment of the layer to be oxidized. In general, the larger the first three factors, the higher the lateral oxidation rate. Many references on this oxidation process are available in the literature, and the interested reader is referred to [2-10] for the detailed analysis and applications. It is important to note here that each individual oxidation system should be calibrated for reproducibility before implementation. In our case, it is also common practice to run trial samples before oxidizing the real devices.

A standard furnace temperature of 425°C was chosen to ensure a high enough oxidation rate that reasonably short oxidation duration (<30 minutes) is possible. A constraint in the lateral oxidation of the tunable VCSEL is that the AlAs layer underneath the anchor be completely oxidized while that beneath the cantilever end is not. A region 5μm to 10μm across of unoxidized AlAs is desirable to facilitate current injection under the cantilever head. If the AlAs layer under the anchor were not completely converted, the pumping efficiency into the VCSEL would be decreased

---

[1] Now how often would the phrase "hot and steamy" appear in a Ph.D. thesis?

due to the extra path available to the injected current. This scenario is shown in figure 3.6. As a consequence, we have a restriction on the geometry that the lateral dimension of the mesa underneath the anchor be smaller than the mesa under the head of the cantilever beam.
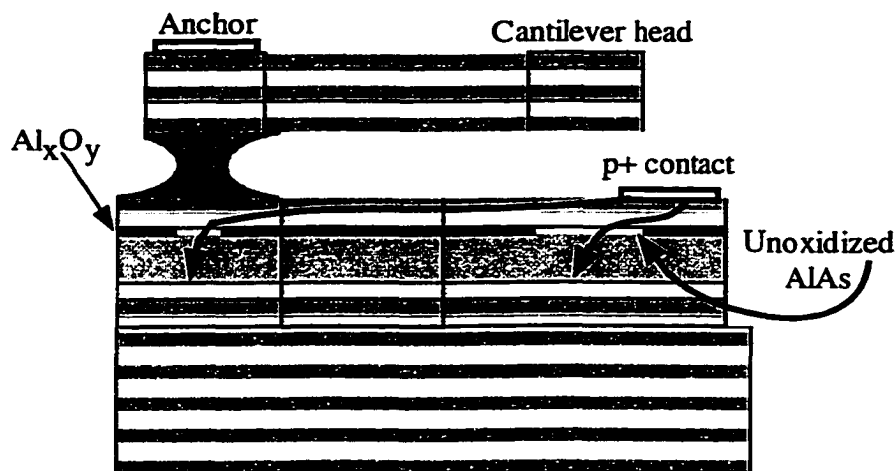
Figure 3.6 Current paths as a result of incomplete oxidation beneath the anchor
If the AlAs layer underneath the anchor were not completely oxidized, there would be two paths for the current injected through the p+ contact, thereby reducing the pump efficiency of the VCSEL. Therefore, one design constraint in the layout of the tunable VCSEL is that the dimension of the mesa underneath the cantilever head be larger than that under the anchor.

IV   GaAs-selective etch

It was mentioned in chapter 2 section III A that several choices are available in the selective etch process. In general for AlGaAs materials, it is easier to find etch recipes that selectively remove either AlAs (no gallium) or GaAs (no aluminum) against AlGaAs (with both Al and Ga). Since an AlAs layer is necessary for the transverse mode definition in our VCSEL, incorporating AlAs sacrificial layers is out of the question for us. GaAs is the next logical choice for a sacrificial layer. An extra advantage to using GaAs rather than AlAs is that GaAs is stable under standard temperature and pressure (STP) compared to AlAs. AlAs layers that only need be

66

about 1000Å in thickness have a tendency to oxidize and flake off after a couple of days [11, 12].

The selective etch we chose to use has been reported in the literature [13-15].[2] It is very similar to the vertical etch used to define the cantilever in section II. A small amount of SF_6 gas is added to $SiCl_4$ in the RIE chamber. Under plasma excitation, two counteractive forces are at work.[18] The etching action of the $SiCl_4$ plasma attacks the AlGaAs material while the SF_6 plasma passivates the exposed etched surfaces. The fluorine ions in the SF_6 plasma and the dangling bonds of the exposed Al-atoms on the sample's surface form a passivating, stable layer of AlF_3. This AlF_3 layer protects the AlGaAs material underneath from being etched further by the chlorine ions in the $SiCl_4$ plasma. A successful selective etch requires the careful balance between these two opposing forces.

The important figure of merit in this etch, of course, is the ratio of etch rates of GaAs relative to that of the neighboring AlGaAs layers. This selectivity depends on several parameters such as the aluminum content in the surrounding AlGaAs layers, the $SiCl_4/SF_6$ flow rate ratio, process gas pressure, RF power, and the surface quality and geometry of the sample. In our experience, the optimal etch conditions for different machines can be very different. Bringing up a new RIE with numerous pump swaps along the way has taught us that even the same vacuum chamber backed by different pumps can behave very differently. Therefore, before any selective etch recipe is used in any etcher, a thorough, systematic calibration of GaAs etch rates relative to the surrounding AlGaAs layers should be pursued.

---

[2] There are other selective etches available as well. See [16, 17] for details. For reasons of etch profiles and etch rate selectivity, we did not choose to use those.

We have performed these systematic calibrations on our system with the epitaxial structure shown in figure 3.7(a). Thin, buried AlGaAs layers with different aluminum composition are sandwiched by thick GaAs layers. Timed etches are performed on the sample under various etch conditions. The resultant etch depths are measured with profilometers. For each set of process parameters, we would get a plot very similar to figure 3.7(b), from which etch rates for the GaAs and each AlGaAs layers are then deduced. The staircase feature outlined by the dashed line in figure 3.7(b) shows us the huge difference in the amount of time it takes to etch 3000Å of GaAs against that for only 100Å of AlGaAs.
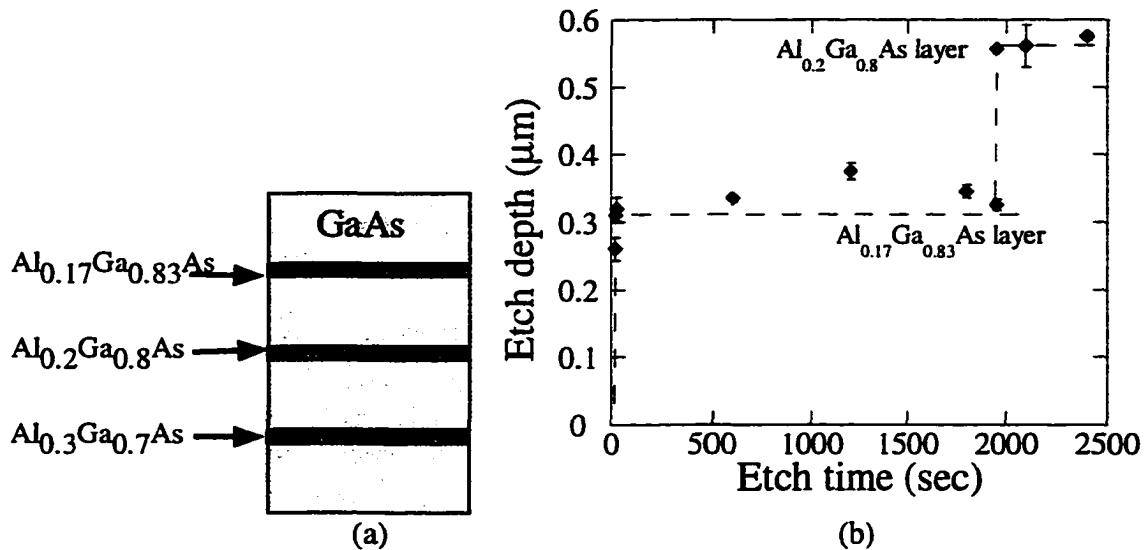
Figure 3.7 Selective etch calibration
(a) Shown here is the layer structure of the calibration wafer used to find the optimal selective etches parameters. Thick (~3000Å) GaAs layers sandwich 100Å thick AlGaAs layers containing different aluminum compositions as indicated. (b) Etch depth of the structure in (a) plotted against etch time. The $Al_{0.2}Ga_{0.8}As$ layer is impervious to this particular selective etch so that it remains intact even after 40 minutes.

The plateaus in the staircase shown in figure 3.7(b) indicate the successive AlGaAs etch stop layers that are exposed. The duration of these plateaus go into the determination of the AlGaAs etch rates while the initial slope of the plot indicates the

68

etch rate for the GaAs layers. Shown in table 3.1 is a summary of our calibration runs

with various parameters.

Etch parameters	Selectivity ratio of GaAs against $Al_{0.175}Ga_{0.825}As$	Selectivity ratio of GaAs against $Al_{0.2}Ga_{0.8}As$
50mT, 20W		
$SiCl_4/SF_6$ flows ratio = 7	11	2307
$SiCl_4/SF_6$ flows ratio = 5	193	2610
$SiCl_4/SF_6$ flows ratio = 3	1715	N/A
$SiCl_4/SF_6$ flows ratio = 2	>3374	N/A
$SiCl_4/SF_6$ flows ratio = 3		
50mT, 20W	1715	N/A
50mT, 30W	2185	N/A
80mT, 30W	6270	N/A

Table 3.1 Etch selectivity for GaAs and AlGaAs under various etch conditions
In figure 3.7(b), we found that the $Al_{0.2}Ga_{0.8}As$ layer is quite impervious to some of the etch parameters we tried, even after a long time. Those are indicated with N/A in the column on the right.

We can infer several trends from the data shown in the table 3.1. Obviously,

AlGaAs layers containing higher aluminum concentrations are more resistant to this

selective etch.[3] Secondly, a higher fraction of SF_6 in the plasma gas mixture

unilaterally improves the selectivity ratio. Both of these results are a consequence of a

higher concentration of Al- bonds and F ions to enhance the formation of AlF_3. The

set of data on the bottom of table 3.1 indicates that increasing the RF power only

increases the selectivity minimally, whereas a slight increase in the process chamber

pressure could enhance the selectivity ratio tremendously.

We should reiterate that the exact values for these parameters would depend

heavily on the chamber geometry, etcher hardware and device geometry. Calibration

---

[3] The discerning reader may ask why high aluminum-content AlGaAs layers are not used to sandwich the sacrificial layer in the tunable VCSEL structure. It turns out that dopants are not as readily incorporated into AlGaAs layers for increasing aluminum concentration.

69

tests were run until we had found the optimal conditions that best suit our chamber and our devices.

Other than timed etches, there are other ways to take the guesswork out of this process. We usually incorporate a set of release dummies on our masks. These release dummies are simply a set of circles with varying diameters. They are fabricated the same way as the movable cantilevers. When release dummies of diameters comparable to that of the cantilever heads fall onto the substrate, we know that the GaAs under these dummies have been completely etched away. We can see this with the help of any good optical microscope. This provides a means to warn us that the cantilevers themselves are close to being completely released from the substrate.

V   Critical point dryer

Nominally dry etching such as the RIE leaves behind such a clean surface on the samples that one may immediately proceed to the next fabrication step. However, we always find a thin wet film on our samples after the selective etch. To remove this film, we rinse the samples in a buffered oxide etch solution before the film has a chance to dry. This rinsing poses an additional problem. After the rinsing, our released mechanical structures are stuck onto the substrate from the surface tension of the water. Blow-drying the samples can distort the shape of these mechanical structures.

To get around this problem, we resort to a solution pioneered by biologists who wanted to preserve their specimens with a sublimation process using carbon dioxide(CO_2). In the critical point drying (CPD) [19] process, high pressure

(>1055psi) liquid CO_2 enters a methanol soaked chamber in which the sample is held. After the methanol in the chamber is completely replaced by the CO_2 liquid, the temperature of the chamber is increased until a critical point transition is reached where the liquid CO_2 sublimes into gaseous carbon dioxide. This critical point occurs at 1055psi and 33.1°C, which can be readily achieved simply with hot plates. Out of the CPD chamber, the cantilevers in our samples would automatically be released in their final form. No further handling or processing of these structures is necessary before testing.

VI   Scanning electron micrograph

Figure 3.8(a) below shows a scanning electron micrograph of the finished device. An enlarged version of the head has also been included in figure 3.8(b).

71

(a)

(b)
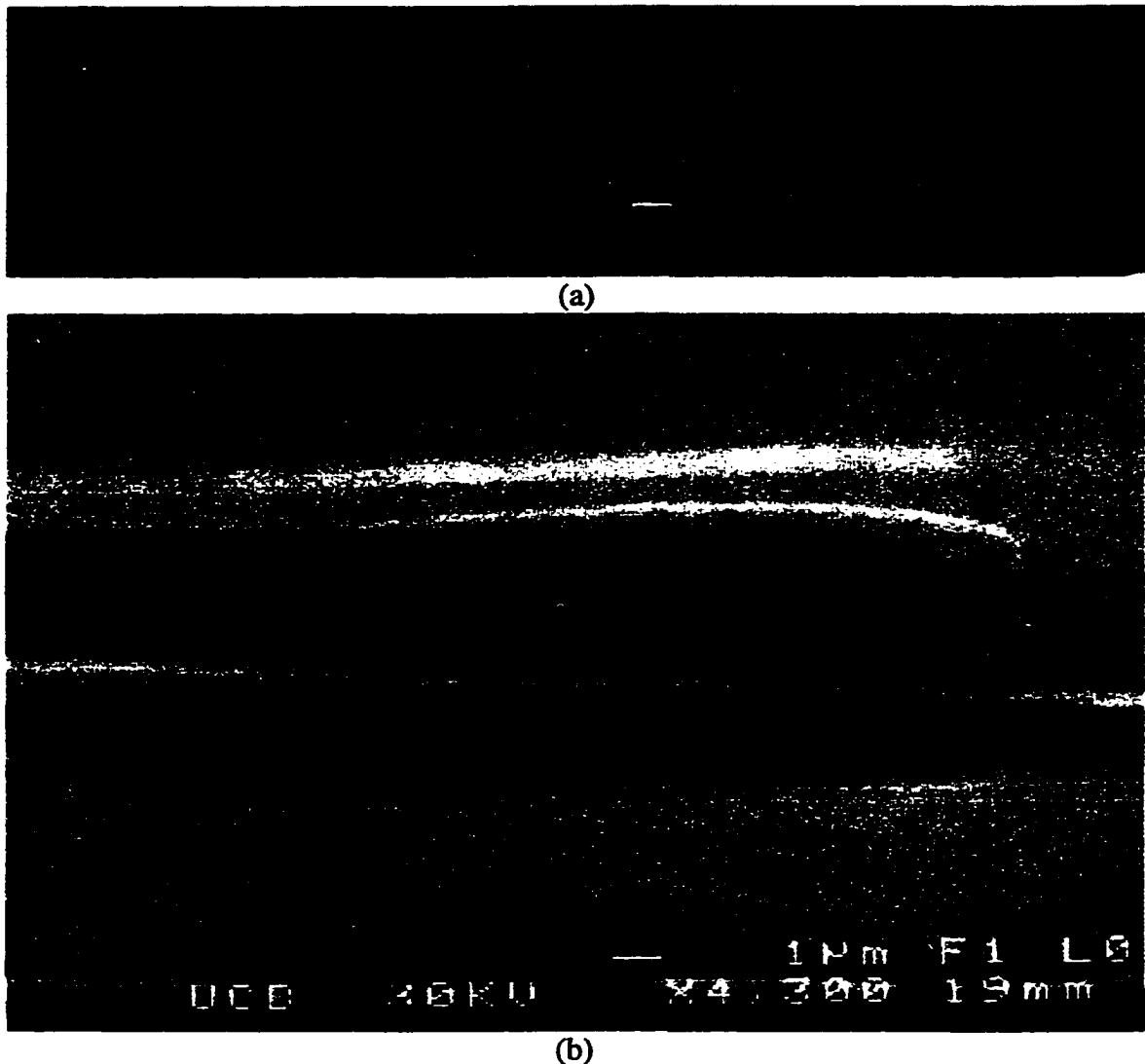
Figure 3.8 Scanning electron micrographs of the finished tunable VCSEL
(a) The device shown here has a 100μm long by 4 μm wide cantilever beam. The circular head is 20μm across in diameter. (b) Shown here is the enlarged view near the head. The beam has been completely released from the substrate.

Judging from these pictures, it may seem that the cantilever is quite fragile. It should be pointed out here that GaAs on the scale of a few hundred microns is extremely flexible. The free end of the narrow beam can be pulled aside up to ~10° without breaking. When freed, it bounces back to the original position like a rubber band. Although the idea seems counter-intuitive, the small size of these mechanical structures renders them quite robust.

72

VII   Summary

In this chapter, we have gone over the fabrication process of the tunable VCSEL in this chapter. It is quite simple and straightforward, requiring four masks with only one critical alignment. Procedures that are unusual for III-V device processing have been outlined. Extremely helpful is an in-situ etch monitor system. Lateral oxidation of the AlAs layer in the tunable VCSEL provides a simple and convenient means of achieving transverse mode definition in the device. Process parameters of the GaAs-selective etch we use are presented and summarized. As a result of the release etch, our sample needs to be cleaned in liquid and dried in a critical point sublimation apparatus using CO_2. These available tools all contribute to the simple fabrication process capable of delivering high device yield in a manufacturing environment.

VIII   References

[1]   G. S. Li, "Wavelength Selective Detectors for Fiber Optic Communications," in *Applied Physics*. Stanford, CA, USA: Stanford University, 1998, pp. 130.

[2]   T. H. Oh, M. R. McDaniel, D. L. Huffaker, and D. G. Deppe, "Cavity-induced antiguiding in a selectively oxidized vertical-cavity surface-emitting laser," *IEEE Photonics Technology Letters*, vol. 10, pp. 12-14, 1998.

[3]   D. L. Huffaker, L. A. Graham, H. Deng, and D. G. Deppe, "Sub-40 mu A continuous-wave lasing in an oxidized vertical-cavity surface-emitting laser with dielectric mirrors," *IEEE Photonics Technology Letters*, vol. 8, pp. 974-6, 1996.

[4]   C. I. H. Ashby, J. P. Sullivan, K. D. Choquette, K. M. Geib, and H. Q. Hou, "Wet oxidation of AlGaAs: the role of hydrogen," *Journal of Applied Physics*, vol. 82, pp. 3134-6, 1997.

[5]   P. W. Evans and N. Holonyak, Jr., "Planar anisotropic oxidation of graded AlGaAs for high resolution vertical-wall current and light guiding in laser diodes," *Applied Physics Letters*, vol. 71, pp. 261-3, 1997.

[6]   K. D. Choquette, K. M. Geib, C. I. H. Ashby, R. D. Twesten, O. Blum, H. Q. Hou, D. M. Follstaedt, B. E. Hammons, D. Mathes, and R. Hull, "Advances in selective wet oxidation of AlGaAs alloys," *IEEE Journal of Selected Topics in Quantum Electronics*, vol. 3, pp. 916-26, 1997.

[7]   K. D. Choquette, K. M. Geib, H. C. Chui, B. E. Hammons, H. Q. Hou, T. J. Drummond, and R. Hull, "Selective oxidation of buried AlGaAs versus AlAs layers," *Applied Physics Letters*, vol. 69, pp. 1385-7, 1996.

[8]   F. Reinhardt, B. Dwir, and E. Kapon, "Oxidation of GaAs/AlGaAs heterostructures studied by atomic force microscopy in air," *Applied Physics Letters*, vol. 68, pp. 3168-70, 1996.

[9]   K. D. Choquette, K. M. Geib, R. Hull, H. Q. Hou, K. L. Lear, H. C. Chui, B. E. Hammons, and J. A. Nevers, "Wet oxidation of AlGaAs vs. AlAs: A little gallium is good," presented at LEOS '96 9th Annual Meeting. IEEE Lasers and Electro-Optics Society 1996 Annual Meeting Cat. No.96CH35895 Conference Proceedings LEOS'96 9th Annual Meeting IEEE Lasers and Electro-Optics Society, Boston, MA, USA, 1996.

[10]   K. D. Choquette, H. Q. Hou, K. M. Geib, and B. E. Hammons, "Selectively oxidized vertical-cavity laser performance and technology," presented at No.98TH8339 1998 IEEE Aerospace Conference. Proceedings, Snowmass at Aspen, CO, USA, 1998.

[11]   E. C. Vail, "Micromechanical Tunable Vertical Cavity Surface Emitting Lasers," in *Electrical Engineering*. Stanford, CA, USA: Stanford University, 1997, pp. 177.

[12]   M. S. Wu, "Micromachined Wavelength Tunable Optoelectronic Devices and Applications in All-Optical Networks," in *Electrical Engineering*. Stanford, CA, US: Stanford University, 1997, pp. 165.

[13]   C. B. Cooper, S. Salimian, and H. F. MacMillan, "Reactive Ion Etch Characteristics of Thin InGaAs and AlGaAs Stop-Etch Layers," *Journal of Electronic Materials*, vol. 18, pp. 619-622, 1989.

[14]   S. Salimian and C. B. Cooper, "Selective dry etching of GaAs over AlGaAs in $SF_6/SiCl_4$ mixtures," *Journal of Vacuum Science and Technology B*, vol. 6, pp. 1641-1644, 1988.

[15]   S. Salimian, C. B. Cooper, R. Norton, and J. Bacon, "Reactive ion etch process with highly controllable GaAs-to-AlGaAs selectivity using SF_6 and $SiCl_4$," *Applied Physics Letters*, vol. 14, pp. 1083-1085, 1987.

[16]   T. Kitano, S. Izumi, H. Minami, T. Ishikawa, K. Sato, T. Sonoda, and M. Otsubo, "Selective wet etching for highly uniform $GaAs/Al_{0.15}Ga_{0.85}As$ heterostructure field effect transistors," *Journal of Vacuum Science and Technology B*, vol. 15, pp. 167-170, 1997.

[17]   C. Juang, K. J. Kuhn, and R. B. Darling, "Selective etching of GaAs and $Al_{0.3}Ga_{0.7}As$ with citric acid/hydrogen peroxide solutions," *Journal of Vacuum Science and Technology B*, vol. 8, pp. 1122-1124, 1990.

[18]   K. L. Seaward, N. J. Moll, and W. F. Stickle, "The role of aluminum in selective reactive ion etching of GaAs on AlGaAs," *Journal of Vacuum Science and Technology B*, vol. 6, pp. 1645-1649, 1988.

[19]   M. Houston and G. Mulhern, "CO_2 critical point drying procedures," in *UC Berkeley Microlab manual*. Berkeley, CA, USA, 1996, pp. 3.

Device Performance

In this chapter, we will review the performance of our top-emitting micromechanical tunable VCSELs. Specifically, the performance characteristics of two devices with different aperture sizes will be highlighted. We have demonstrated the first top-emitting micromechanical tunable VCSEL with a continuous tuning range of 20nm.[1] This device has an aperture size of $5\mu m$ and is the first topic of our discussion in this chapter. The other device whose performance we will highlight has demonstrated complete wavelength coverage across 31.6nm, which is a record to date for a monolithic VCSEL.[2]

As discussed in the oxidation section in chapter 3, the aperture size of a device is determined through a lateral oxidation process that converts AlAs to aluminum oxide, which acts as a lateral current block within the VCSEL. The aperture sizes quoted here are determined visually under a microscope when the devices are pumped and spontaneous emission is given off. These sizes are approximately the same as that which defines the lateral extent of gain in each device.

In addition to the performance of these two devices, we will also discuss the wavelength change of the tunable VCSEL with temperature in the absence of any

76

active feedback. A simple application utilizing the tunability of these devices to

achieve active wavelength stabilization will also be presented at the end of this

chapter.

I   5μm aperture device

In this section we will discuss the smaller device's tuning spectra as well as its

figures of merit under pulsed and continuous wave (CW) operations at room

temperature. The mechanical cantilever beam for this particular laser is a 100μm long

by 3μm wide.
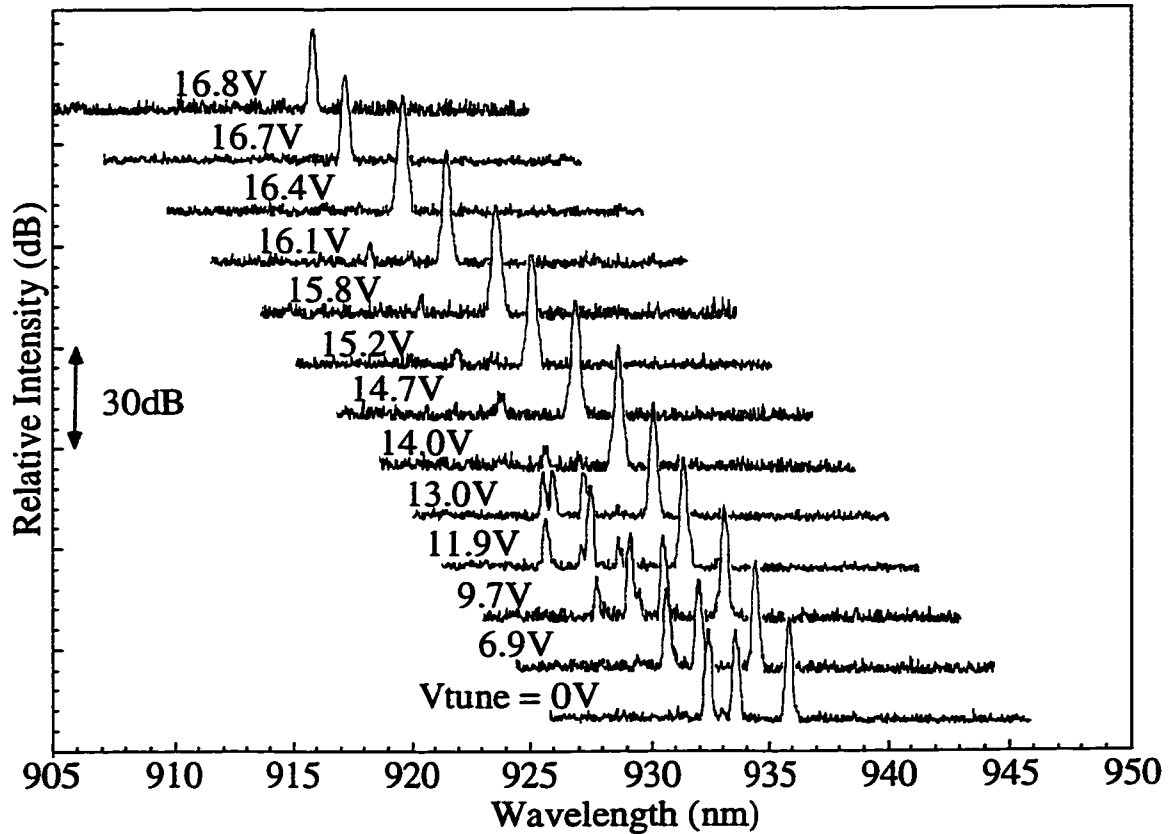
Figure 4.1 Tuning spectra of a 5μm wide tunable VCSEL.
20nm of continuous coverage is demonstrated with this first top-emitting
micromechanical tunable VCSEL. Due to the small transverse dimensions of this
device, good side-mode suppression is achieved. See the discussion below for an
explanation of the satellite peaks in the spectra at the lower tuning voltages.

77

Shown in figure 4.1 above are the continuous wave (CW) tuning spectra of this VCSEL operating at a constant pump current of 2.5mA at room temperature. For the spectra that show multiple transverse modes at the lower tuning voltages, we should pay special attention to the reddest mode, the one with the longest wavelength, as this is the fundamental transverse mode. When there is no bias across the tuning junction, lasing occurs at 936nm. As the tuning bias is increased, the cantilever bends towards the substrate, and subsequently, the FP-wavelength of the cavity blue-shifts. It continues to do so until it reaches 916nm, beyond which point there is insufficient optical gain to support lasing.

The evolution of this device's emission spectra at different wavelengths also gives us a hint as to the location of the gain peak.[1] As the tuning bias increases, the strength of the higher order satellite peaks decreases. When the satellite peaks disappear, only the fundamental mode remains, which continues to blue-shift as the tuning bias is increased. The relative strength of the higher order transverse modes compared to that of the fundamental mode is a telltale sign of the position of the gain peak at the given pump condition, which is 2.5mA in this case. Consequently, from the spectra alone, we can deduce the gain peak to be near 927nm when the device is pumped at a constant current of 2.5mA.

---

[1] The transverse mode profiles at the lower tuning voltages are typical of VCSELs with oxidized AlAs current confinement layers and small apertures. One often sees the fundamental transverse mode accompanied by a pair of bluer satellite modes. Sometimes when the size of the aperture is small enough, one would see two, even three pairs of these satellite peaks situated further and further to the blue side of the fundamental mode.[3]
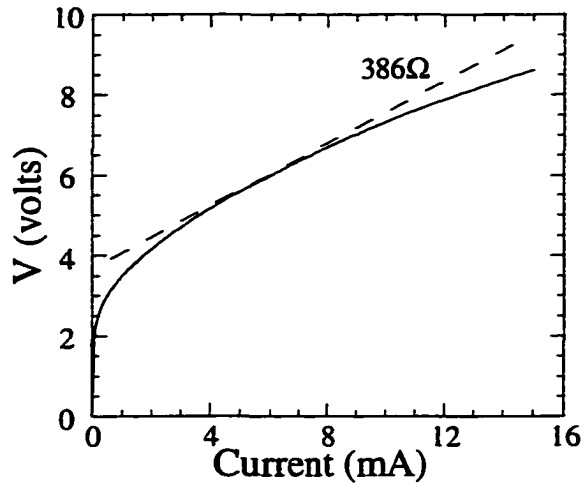
Figure 4.2 IV-characteristics of the tunable VCSEL with a 5μm aperture
The forward-biased pn-junction has a differential resistance of ~400Ω, a typical
value for an intracavity contacted VCSEL.

Shown in figure 4.2 above is the current-voltage (IV-) characteristic of this

device under CW operation. Electrical properties such as the bandgap of the pn-

junction and the device's series resistance can be deduced from the plot. From figure

4.2, we find the differential series resistance of the gain junction to be ~400Ω, a

typical value for VCSELs with an intracavity contact.[4-6] This is so because

included in the current path are a long lateral path (>10μm) through a heavily doped

narrow channel (~1000Å deep), and a short vertical path (~0.5μm) through a lightly

doped region, (see figure 3.5(c)). The resultant resistance can cause significant heating

in the junction, which affects device performance through the narrowing of the

bandgap and the subsequent shifting of the gain peak. How this specifically affects

our device performance is discussed at the end of this section.

Other than a diode laser's IV-characteristic, which indicates the electrical

properties of the device, the light-current (LI-) characteristic summarizes the device's

optical properties. Information ranging from threshold current and output power to

mirror loss in the cavity can be deduced from a laser's LI-curve. Shown in figure 4.3

are the LI-curves of this 5μm laser at various tuning voltages (and thus various

wavelengths) under CW operation. As the tuning bias increases, the threshold current

increases and the slope of the curve beyond threshold begins to decrease. This slope is

called the differential quantum efficiency (DQE) of the laser and is defined as the

number of extra photons out of the cavity for each additional electron-hole pair

injected into the cavity.
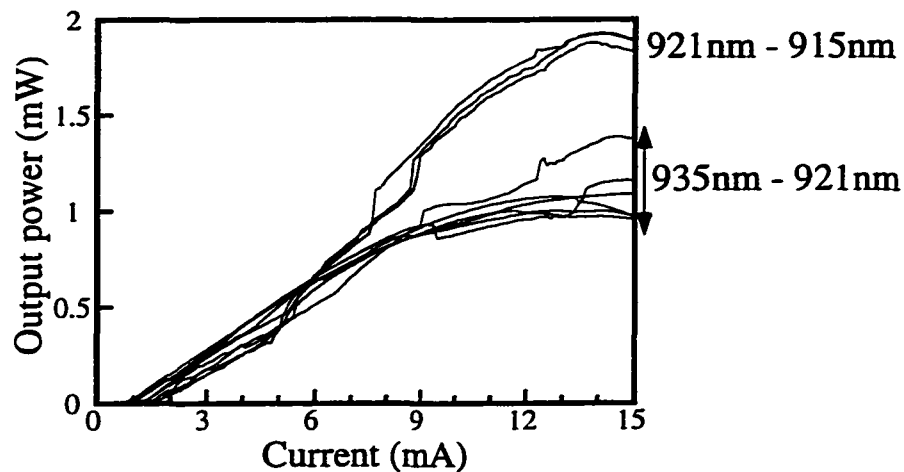
Figure 4.3 LI-characteristics of the 5μm tunable VCSEL under CW operation at room temperature
The increase in the output power around 8mA towards the blue end of the tuning spectrum (λ<921nm) is attributed to the increase of the available gain (in the redder part of the spectrum) as the gain junction heats up through the increased injection current. This tunable laser perform best, i.e. has high output power, when the FP-wavelength is bluer than the gain peak wavelength at low current levels.

Summarized in figure 4.4 below are the CW threshold current and differential

quantum efficiency of the device across its tuning spectrum.
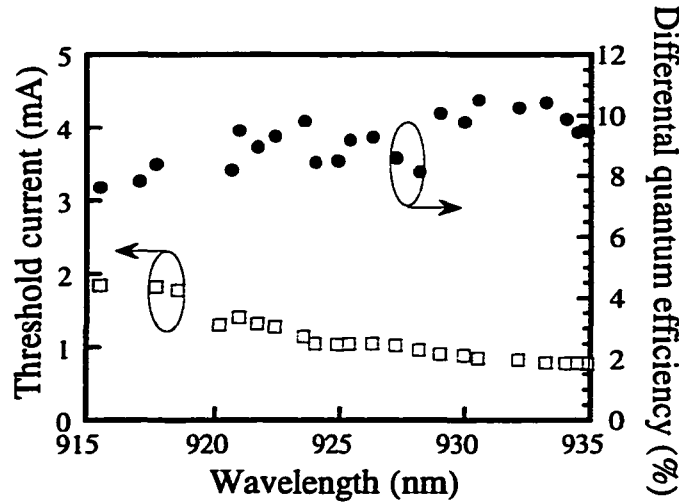
Figure 4.4 Summary of CW threshold current and differential quantum efficiency across the tuning range of the 5μm tunable VCSEL
Open squares indicate threshold current and solid circles show the differential quantum efficiency across the tuning range. Uniform characteristics across the 20nm of wavelength coverage are achieved. As discussed in the following section, this is a result of a happy coincidence between the relative positions of the gain peak wavelength and the wavelength at which the top DBR has its maximum reflectivity.

From figure 4.4 above, we see that both the threshold current and differential quantum efficiency are quite uniform across the 20nm tuning range of this device. This result is actually a happy coincidence of two separate cavity issues. The gain peak happens to be spectrally located where the reflectivity of the top DBR begins to roll off. To illustrate this point, let us examine the definitions of threshold gain g_{th} and differential quantum efficiency η_{diff}:

$$\eta_{diff}(\lambda) \equiv \eta_i \frac{\alpha_{top}(\lambda)}{\alpha_{total}(\lambda)}; \text{and} \tag{4.1}$$

$$g_{th}(\lambda) \equiv \alpha_{total}(\lambda); \text{where} \tag{4.2}$$

$$\alpha_{total}(\lambda) = \alpha_{top}(\lambda) + \alpha_{bottom}(\lambda) + \alpha_{internal}(\lambda). \tag{4.3}$$

In (4.1) η_i is the internal injection efficiency of the gain region, α_{top} the optical loss through the top DBR, and α_{total} the optical loss through the rest of the structure. The latter includes internal cavity loss as well as the mirror losses through both the top and

81

the bottom DBRs, as explicitly stated in (4.3). To find the relationship between the injection current and threshold gain in a cavity, we need an empirical relationship between gain (g) and carrier density (N). This is expressed as the following [7]:

$$g(\lambda) = g_0(\lambda) \ln \frac{N}{N_{tr}(\lambda)}, \qquad (4.4)$$

where N_{tr} is the transparency carrier density and g_0 an empirically-derived gain coefficient. The wavelength dependencies of these parameters have been explicitly stated in (4.4) also. Substituting (4.2) into (4.4) we arrive at the empirical expression for the threshold carrier density in the active region as a function of wavelength:

$$N_{th}(\lambda) = N_{tr}(\lambda) e^{\frac{\alpha_{total}(\lambda)}{g_0(\lambda)}}. \qquad (4.5)$$

Since the injection current is proportional to carrier density, we can safely express the threshold current as the following:

$$I_{th}(\lambda) = I_{tr}(\lambda) e^{\frac{\alpha_{total}(\lambda)}{g_0(\lambda)}}. \qquad (4.6)$$

As we can see from (4.6), it is no simple feat to theoretically deduce the exact dependence of the threshold current on wavelength. One would need a good knowledge of the phenomenological parameters in the active region such as $I_{tr}(\lambda)$ and $g_0(\lambda)$ in addition to those for the cavity such as $\alpha_{total}(\lambda)$, the combined optical losses in one roundtrip.

Fortunately, we can find the relative alignment of α_{top} and gain peak wavelength with figures 4.1, 4.3, and 4.4 above. From the definition of η_{diff} in (4.1) and the data shown in figure 4.4, we can deduce that the fractional optical loss through the top DBR, $\alpha_{top}/\alpha_{total}$, increases towards the red end of the tuning spectrum. Since

we expect both η_i and the $\alpha_{internal}(\lambda)$ component of $\alpha_{total}(\lambda)$ in (4.1) to be constant across these 20nm, we can safely attribute the increase of $\alpha_{top}/\alpha_{total}$ towards the red end of the spectrum to the increase of α_{top} alone.

The location of the gain peak can be roughly deduced from figure 4.1. At 2.5mA of constant current, the gain peak is near 927nm. As it is known that the gain peak in the InGaAs and AlGaAs systems red-shifts at 3Å/K [8], we can reasonably expect that the gain peak of the quantum wells in the absence of any heating occurs at a slightly bluer wavelength. Given a thermal resistance ~1200K/W [9] for GaAs in a 5μm aperture device, biasing our VCSEL at 2.5mA (and 4.4V from figure 4.2 above) yields an increase of 13.2K. This translates into ~40Å wavelength shift to the red. Thus the gain peak without any pumping is around 923nm. This also explains the abrupt increase in output power at ~8mA (see figure 4.3 above) when the initial emission wavelength is less than 923nm.

If the gain peak and the reflectivity peak of the DBRs had been aligned perfectly to each other, one would expect the minimum for both I_{th} and differential quantum efficiency to occur at the aligned wavelength and that both would monotonically increase as the wavelength deviates from the center. A more flattened I_{th} and DQE relationship against wavelength would be expected if the gain peak and the peak reflectivity of the top DBR were slightly misaligned. This is the case here. From the rough calculations in the previous paragraph, our inferred gain peak is at 923nm whereas the DQE data points in figure 4.4 imply that the top DBR reflectivity peak is at a shorter wavelength. Therefore, especially for the tunable VCSEL, uniform

lasing characteristics across the tuning range requires careful consideration of the relative alignment between the gain and cavity in both design and practice.

II   10μm aperture device

The performance of a tunable VCSEL with a larger oxide aperture of 10μm in diameter is discussed in this section. This device demonstrates continuous tuning across 31.6nm. To the best of our knowledge, this remains a record tuning range for a monolithic VCSEL to date. The cantilever for this laser is 150μm long by 5μm wide.

Shown in figure 4.5 below is a plot of the tuning spectra demonstrated by this 10μm wide device at 1.2 times threshold current under CW operation at room temperature. At zero tuning bias, lasing occurs at 931nm. As the tuning voltage increases, blue-shifting of the wavelength is observed as expected. This trend continues until the emission wavelength reaches a minimum at 919.1nm. An increase in the tuning bias at this point causes the emission wavelength to make a single hop from the blue end all the way to the red end at 950.7nm. A further increase in the tuning bias again causes further blue-shifting of the wavelength until it wraps around completely to the original starting wavelength. All wavelengths within the entire 31.6nm are accessible with 27 volts of tuning bias.
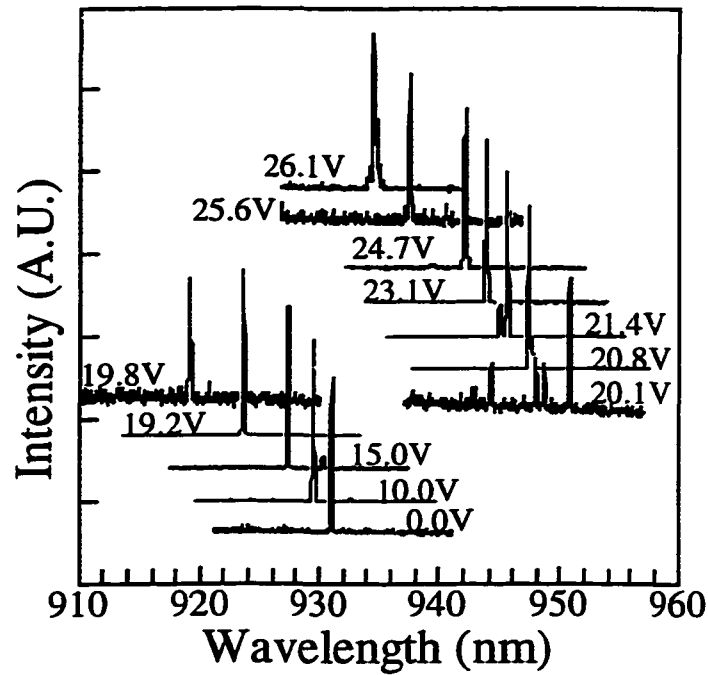
Figure 4.5 CW tuning spectra of a 10μm VCSEL at room temperature
This device demonstrates continuous coverage of 31.6nm in 27V. There is one jump
in the emission wavelength at ~20V. This discrete hop is explained in the following
section.

Upon first look at figure 4.5, the one discrete hop from the blue end of the

spectrum to the red might be baffling. To explain this, let us take a look at figure 4.6

below. In this plot, the calculated FP-wavelength of the tunable VCSEL structure as a

function of the air gap thickness in the top DBR is plotted. Because the air gap

thickness is always decreasing with increasing tuning bias V, the x-axis is plotted in

reverse scale below.

85
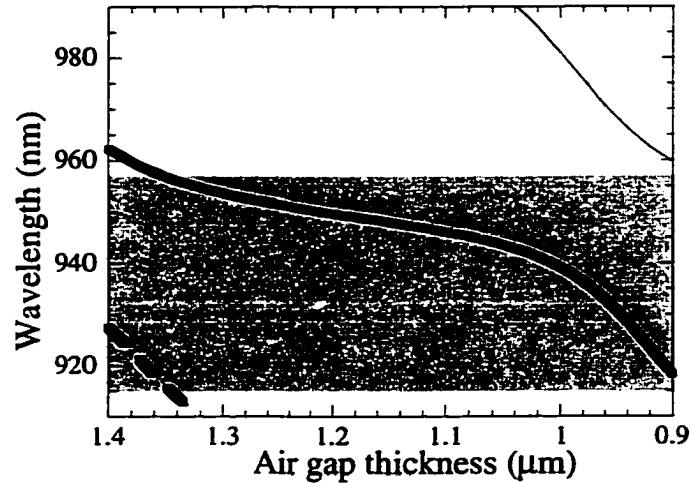
Figure 4.6 Calculated FP-wavelength as a function of the air gap thickness for the tunable VCSEL the tuning spectra of which are shown in figure 4.5
Three longitudinal modes exist in this range of air gap thickness. The gray box indicates the spectral region across which gain is available.

In the range of the air gap thickness plotted, there are three longitudinal modes.

The lasing mode is the one that sees the most gain. In this case, we can infer from

figure 4.1 that the gain peak of this structure is located near 927nm. The spectral

regime in which sufficient gain exists has been marked in a light gray box for ease of

illustration. Due to the location of highest order of the three longitudinal modes (the

dashed curve in figure 4.6) is closest to the gain peak, this mode would lase first. An

increase in the tuning voltage causes the air gap to shrink and the FP-wavelength to

blue-shift along this longitudinal mode. This continues until the air gap thickness has

reduced to a point where the next lower order longitudinal mode (the thick solid curve

in figure 4.6) sees more gain than the original mode. Then, the lasing wavelength

would make the jump to that longitudinal mode. Further decrease in the air gap

thickness allows the lasing wavelength to blue-shift along this new longitudinal mode.

It should be noted that had the gain peak been situated in the middle of the thick solid

curve, continuous tuning without any wavelength jumps would be possible.
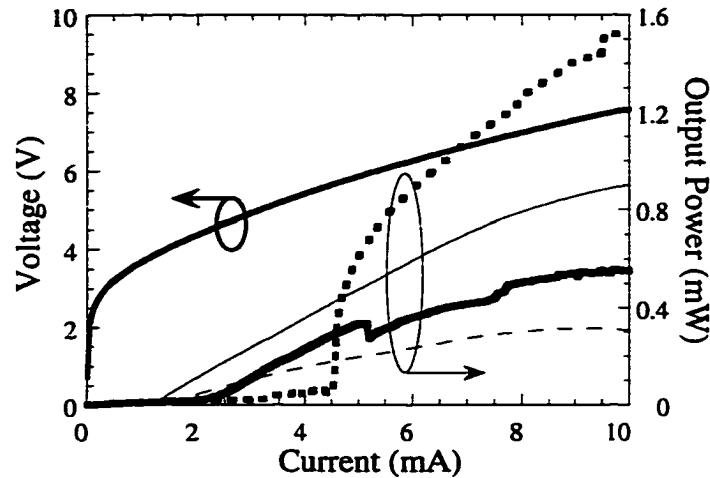
Figure 4.7 LI- and IV- characteristics of the 10μm aperture VCSEL across its tuning range
The left vertical axis refers to the IV-curve. The set of four LI-curves is read off with the vertical axis on the right. The legends are as follows: The thin solid line shows the LI-characteristic for the device under no tuning bias (931nm); the thick solid line is the device at the bluest end of the tuning spectrum (919nm); the thick dotted line is the device after its discrete hop to the reddest end of the spectrum (951nm); and the thin dashed line shows the LI when the emission wavelength has wrapped around once in the spectrum.

Shown in figure 4.7 above are the CW IV- and LI- characteristics for this 10μm

aperture VCSEL. The four different LI- curves represent the device at four different

tuning biases. The thin solid line is the LI-curve without any tuning bias. The thin

dashed line is the LI-curve after the lasing wavelength has wrapped once around the

31.6nm back to the starting wavelength. Since the lasing wavelengths are the same for

these two LI-curves, the difference in the slope efficiencies between them stems from

the extra loss added to the cavity due to the tilt in the top DBR. The light-current

characteristics for the device in the bluest part of the tuning spectrum is shown in the

thick solid line while the thick dotted line shows the device's output power in the

reddest part of the tuning spectrum. At the red end of the tuning spectrum, abrupt

turn-on of the laser is observed. This is attributed to the heating of the active region

that sufficient gain at the FP-wavelength is suddenly made available for lasing in the

red to occur.
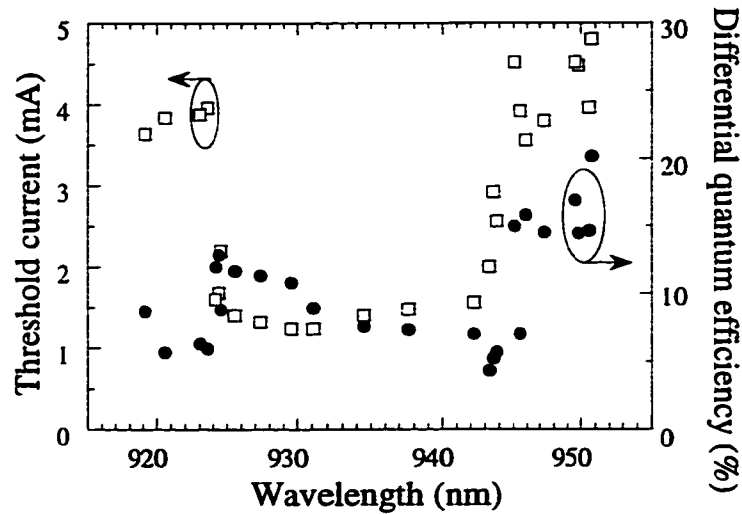
Figure 4.8 CW threshold current and differential quantum efficiency for the 10μm tunable VCSEL

Open squares indicate threshold current while solid circles show the differential quantum efficiency at each wavelength. Refer to the section below for a thorough discussion on the data in this figure.

The CW threshold current and differential quantum efficiency (DQE) across

this device's tuning spectrum are summarized in figure 4.8 above. The discrete jump

in both these figures of merit at 921nm is due to a spatial mode change of the output

that can be observed on the video camera. The more gradual increase in both the

threshold current and differential quantum efficiency on the red end of the spectrum is

attributed to the top DBR's roll-off from its maximum reflectivity. This is confirmed

when we measure this device under pulsed operation, the results of which is shown in

figure 4.9 below. In pulsed mode, the laser exhibits the same general trend near the

red end of the tuning spectrum. An interesting note here is that the tuning range under

pulsed operation is shorter than that obtained under CW operation by approximately

88

5nm. This is attributed to the lack of gain in the red end of the spectrum when there is no constant injected current to heat up the junction.
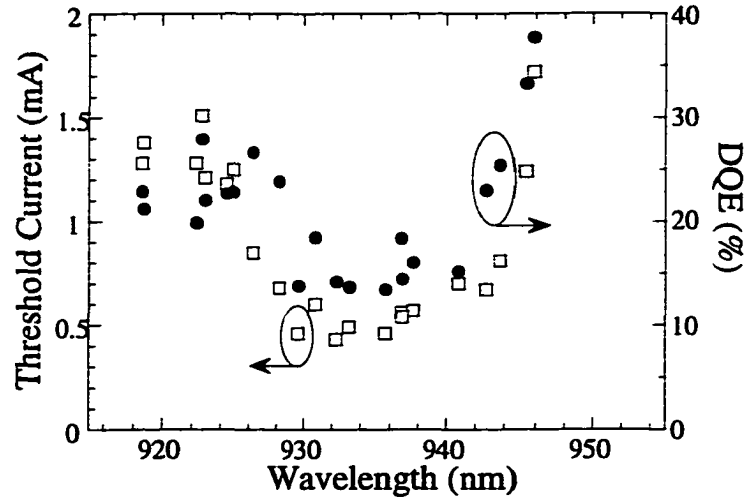
Figure 4.9 Pulsed threshold current and differential quantum efficiency (DQE) for the 10μm tunable VCSEL
The VCSEL is pumped with current pulses at 10kHz and 0.5% duty cycle at room temperature. Open squares indicate peak (not average) threshold current while the solid circles show the differential quantum efficiency of the LI-curves in pulsed operation.

III Application

An immediate application for a tunable VCSEL is to utilize this tunability to actively stabilize the lasing wavelength. This is an attractive feature especially in light of the temperature- and operation condition-dependent wavelength shift in the conventional VCSEL. This is because the emission wavelength is coupled with the temperature dependent refractive index of the VCSEL through equation (2.2). With this in mind, one can see that unlike its non-tunable cousin, the tunable VCSEL's emission wavelength can be decoupled from all that in its operation. The output wavelength can be actively controlled and monitored so that it remains steady over a broad range of operating temperatures. In this section, we will explain and discuss the

89

temperature-dependent wavelength shift our tunable VCSELs experience. Preliminary results are presented to show that indeed temperature-independent wavelength can be achieved through active feedback and control of the tuning bias.

A Emission wavelength dependence on temperature

It was found that the emission wavelength of conventional AlGaAs VCSELs red-shifts at 0.6Å/K.[8] This is because the refractive indices of the semiconductor materials that make up the VCSEL structure are not constant with temperature, causing the FP-wavelength of the entire AlGaAs structure to shift with temperature also.

Knowing this piece of information, it is easy to come to the conclusion that a tunable VCSEL naturally lases at a fixed wavelength because it has an air-filled cavity. We know that the refractive index of air does not change much with temperature[2]. Therefore, an air-filled semiconductor laser would naturally have the added advantage of a fixed output wavelength, independent of the operating temperature.[3] And the need for any active wavelength control in a tunable VCSEL can be dispensed with.

As it turns out, this line of reasoning is not too far off the mark, although the output wavelength from a tunable VCSEL is not exactly constant, either. Shown in figure 4.10 below is the FP-wavelength of a tunable VCSEL with a small aperture (~4μm in diameter) at constant tuning bias (V_{tune}) and injection (I_{gain}) level measured under pulsed operation (10kHz, 0.25% duty cycle) across a broad range of substrate

---

[2] According to the CRC Handbook of Chemistry and Physics, the index of refraction of dry air at STP (1 atmosphere and 0°C) and at $\lambda = 1\mu m$ decreases at a rate of ~9e-7/°C.

[3] Of course, this is assuming that the mirror separation does not depend on the temperature and that there is no bimorphic effect arising from the difference in the thermal expansion coefficients of the layers in the cantilever.

temperatures. A small device was chosen such that the number of transverse modes is minimized and a precise wavelength measurement could be made. The VCSEL's output beam is collected with a 125μm core optical fiber, and its wavelength is measured with a Hewlett-Packard Optical Spectrum Analyzer (HP70951A) set at a wavelength resolution of 5Å. The use of a relatively broad resolution bandwidth is so that enough of the pulsed signal can be measured on the spectrum analyzer running in the averaging mode.
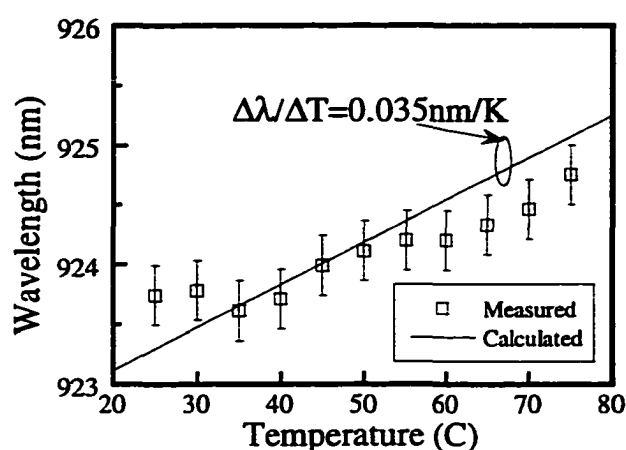
Figure 4.10 Calculated and measured wavelength shift with substrate temperature for a 4μm diameter tunable VCSEL
The open squares indicate the measured wavelength of a 4μm wide tunable VCSEL. A linear fit indicates that the measured wavelength shifts at 0.20Å/K. The error bars show the resolution bandwidth of the measurement.

Also shown in figure 4.10 is the calculated temperature-dependent wavelength shift of the same structure. This calculation is done through the inclusion of the temperature-dependent refractive indices of AlGaAs.[10] It is assumed that the entire structure is thermally connected to the same heat reservoir that the entire structure from cantilever to substrate is at the same temperature. While the calculations give us a rate of wavelength shift with temperature at 0.35Å/K, our measurement shows that the actual wavelength shift is only about 0.20Å/K.

These two results were initially baffling to us. First of all, why would the air-filled VCSEL see less shift than a regular VCSEL reported in [8]? Secondly, how is it that an actual device exhibits a wavelength shift that is half the calculated rate? Upon closer examination, the answer to the first question may be quite straightforward: Because a VCSEL's cavity is distributed in nature, its internal energy extends beyond the physical boundaries of the cavity into the DBRs on each side.[11] If we consider the actual cavity length to include this extension of the energy into the mirrors, then the air gap's temperature-insensitive refractive index would only matter if it is within the "extended" cavity. If the air gap lies outside of this extended cavity in which a significant amount of the internal energy exists, a tunable VCSEL would not behave any differently from a regular VCSEL. Reference [11] shows that the energy penetration distance into an AlAs/GaAs DBR is on the order of one wavelength. So if our air gap lies within one wavelength of the cavity, the wavelength-shift with temperature would be less than 0.6Å/K. However, if our air gap lies beyond one wavelength of the cavity, we would not expect to see any difference in the rate of shift from a regular AlGaAs VCSEL's. Since our structure contains a short p-DBR stack with 4 pairs of AlGaAs low-contrast layers between the air gap and the cavity, we would expect that our VCSEL would then behave more like the latter. But then, you might ask, why is the wavelength shift significantly lower than 0.6Å/K, the expected value?

There is one minor fact that we have overlooked. In both [8] and [11], the VCSEL structure under consideration is completely resonant, i.e. all the DBR layers are quarter wavelength thick. In our case, however, the air gap thickness is not an odd

multiple of λ/4 but much closer to 3λ/2, the anti-resonant situation shown in figure 2.17(b).[4] The phase of the FP-wavelength is so detuned in the structure that, as evident in figure 2.17(b), the penetration of the standing wave into the air gap is more significant than in the resonant case in figure 2.17(a). This is why we would see a large disparity in our measured rate of wavelength here with temperature than what others have quoted. Of course, we also realize that near resonance, i.e. when the air gap is an odd multiple of λ/4 thick, the wavelength shift with temperature would be closer to 0.6Å/K. Our calculations have confirmed this.

It should be noted especially that a tunable VCSEL's relative temperature-insensitivity in its emission wavelength goes hand in hand with its tuning range because both stem from the same cause. If the air gap is at the resonant thickness, the closer it is to the cavity, the more internal field can penetrate into the air gap. Significant amounts of internal field in the air gap can enhance tuning efficiency (i.e. larger change in FP-wavelength for the same change in air gap thickness). Moreover, the air gap's relative temperature-independent index of refraction can have a heightened effect to give the FP-wavelength some immunity to temperature change. It should also be stressed that detuning the air gap from the resonant condition also helps to improve the temperature insensitivity of the emission wavelength, albeit at the price of a reduced modal gain and mirror reflectivity, as discussed in chapter two.

The second question at hand now is why a real tunable VCSEL would shift at only half the rate of the calculated value. Although it may seem obvious, we should point out an important assumption in our calculation, which is that every layer

---

[4] We can tell just by looking at the FP-wavelength being around 923nm rather than 950nm.

throughout the entire VCSEL structure would be at the same temperature. In our experiment, the device is placed on a thermoelectric cooler/heater, so that temperature control is primarily through the substrate. Therefore, while we had a good idea about the substrate temperature, the temperature at which the rest of the VCSEL sits is not so clear. The AlGaAs material system has good thermal conductance (from 0.09-2.3W/cm/K[10]) compared to air that one can expect the VCSEL structure from the p-DBR down to the substrate would experience the same temperature. The same cannot be said for the air gap and the cantilever, however. Air, as we know, is a terrific heat insulator. Therefore, we would expect the cantilever to be at the ambient temperature, no matter what the substrate temperature is. With this in mind, we would then expect a weaker dependence of the emission wavelength with the substrate temperature. Figure 4.11 below shows the results of our calculations when the cantilever is at the ambient room temperature while the rest of the structure's temperature is changed. We see that the rate of cavity FP-wavelength shift with substrate temperature is reduced.

94
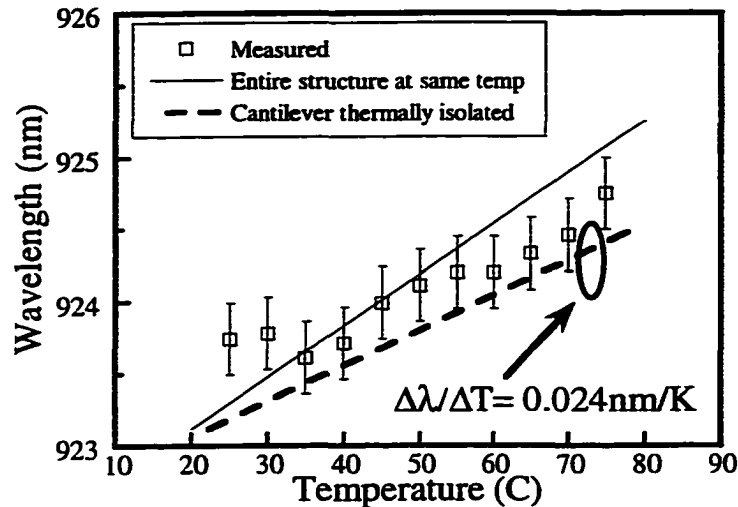
Figure 4.11 FP-wavelength as a function of substrate temperature for the 4μm wide VCSEL, measurement and calculation for the two scenarios explained in the legends of the plot.

As in figure 4.10, the measured data are included in this plot. Two cases are analyzed here. The solid line still represents the case in which the cantilever is at the same temperature as the substrate, as in figure 4.10. The dashed line shows the calculated results when the cantilever is thermally isolated from the substrate and at an ambient room temperature of 15°C.

With the cantilever thermally isolated from the substrate, our calculations show that the wavelength shift with substrate temperature is reduced to 0.24Å/K. This rate is much closer to our observed value of about 0.20Å/K.

B   Active stabilization of emission wavelength

From the foregoing discussion we discovered that tunable VCSELs could experience a wavelength shift with temperature at a lower rate than that observed for conventional AlGaAs VCSELs. In addition, wavelength tunability allows for active wavelength adjustments to keep the emission wavelength steady over a broad range of operating temperatures. This is an important feature inaccessible to regular VCSELs.

With the device discussed in section II, we set out to show that active stabilization of emission wavelength over a broad tuning range is possible for a tunable VCSEL. The laser is placed on a thermoelectric cooler/heater so that the

95

substrate temperature can be controlled. In our experiment, three arbitrary target

wavelengths spaced 10nm apart are set to be 927nm, 937nm and 947nm. As the

substrate temperature varies, the bias voltage is changed so that the emission

wavelength is inside a 1nm window about the target wavelengths. Shown in figure

4.12 is the required tuning bias plotted against the substrate temperature from 25°C to

60°C for the three target wavelengths. The two data points above 50°C for 927nm are

missing because the quantum wells cannot provide sufficient gain to support lasing at

those temperatures.
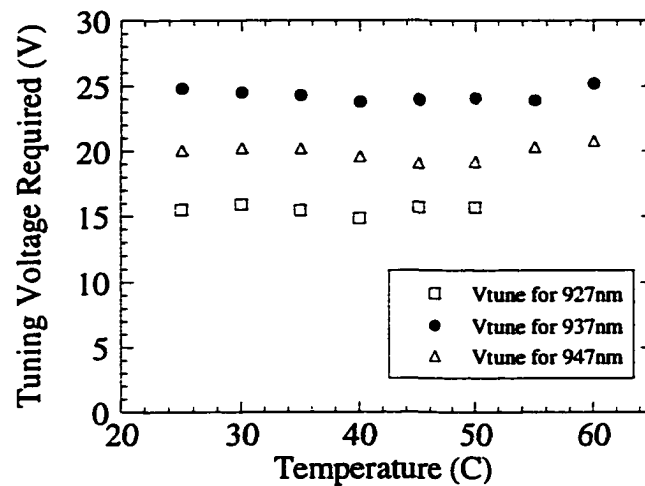
Figure 4.12 Tuning voltage required to maintain the emission wavelength at the three "channels"
The three target channels are at 927nm, 937nm, and 947nm. Ideally, a monotonically decreasing tuning voltage would be seen as the substrate temperature increases. However, competition between the multiple transverse modes in this large area VCSEL keeps the tuning voltage behavior for increasing temperature from being monotonic.

One might wonder why the bias voltage does not monotonically decrease as the

substrate temperature increases. We should keep in mind that this device in particular

has a large aperture, thus many transverse modes. The relative strengths of these

transverse modes change as the temperature, tuning or pump conditions vary. The

temperature behavior of the tuning bias is not monotonic simply because the same

transverse mode does not stay dominant throughout the experiment. Incidentally, the coarse channel spacing (10nm) chosen for this experiment can be used as a local area network WDM standard for optical data link applications in the near IR (850nm).[12]

The LI-curves in figure 4.13 summarize this same VCSEL at the three channels as the substrate temperature increases. In figure 4.13(a), both threshold current and DQE degrade as the substrate temperature increases, as expected of a device in which the emission wavelength is on the blue side of the gain peak. At the 937nm channel in figure 4.13(b), the LI-plots follow roughly the same trend as at 927nm, although the degradation is not as dramatic. This is because the gain peak and the emission wavelength are better matched in this case. At 947nm, the LI-curves in figure 4.13(c) are characterized by vertical slopes at threshold. Because the gain peak here is always bluer than the emission wavelength, we conjecture that the vertical slope at turn-on is a result of gain at 947nm suddenly made available through sufficient heating of the junction with the injection current. This is corroborated by the LI-characteristics at 55°C and 60°C, for which case the turn-on is more gradual. This implies that sufficient gain at 947nm is provided by the substrate temperature rather than by the injected current.
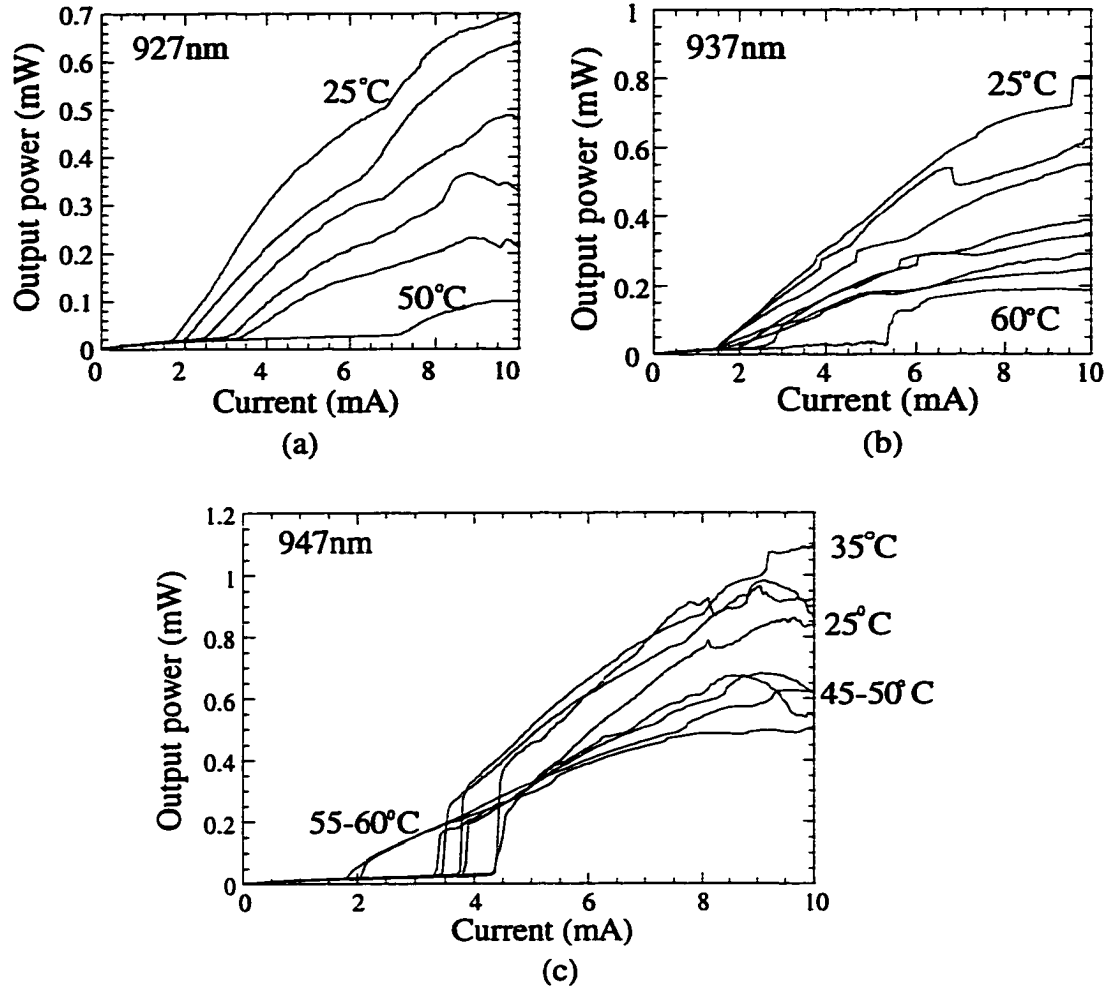
Figure 4.13 CW LI-curves of the tunable VCSEL in section II at the three target wavelengths and different substrate temperatures
(a) 927nm; (b) 937nm; and (c) 947nm.

IV   Summary

In this chapter, we have discussed and highlighted the performance characteristics of a few tunable VCSELs. The first top-emitting VCSEL has a smaller aperture (~5μm in diameter) and demonstrated continuous wavelength coverage across 20nm. Uniform CW threshold currents and output powers on the order of 1mA and 1mW, respectively, are obtained at room temperature. This is the result of a fortunate

slight misalignment between the quantum wells' gain peak wavelength and the maximum reflectivity wavelength of the top DBR.

In addition, we have also demonstrated continuous tuning across 31.6nm in a device with a larger aperture ($\sim$10μm diameter) under CW operation. A single hop from the blue end of the tuning spectrum to the red end is due to a mismatch between the gain peak and the designed longitudinal mode. To the best of our knowledge, this is the widest continuous tuning range demonstrated by a monolithic VCSEL to date. As a result of the 50% wider tuning range, this laser's threshold current and differential quantum efficiency across its wavelength span is not as uniform as the other smaller device. However, good CW threshold currents (<5mA) and output powers (>0.8mW) are still observed across its entire tuning range.

In addition, the rate at which the emission wavelength shifts with the substrate temperature has been measured and compared with results from our analysis in this chapter. We have found that this rate for a tunable VCSEL can be less than that in a conventional AlGaAs VCSEL. This is attributed more to the thermally insulating property of the air gap than to the thermally insensitive refractive index of air.

Moreover, we have shown the feasibility of a tunable VCSEL in an active wavelength stabilization scheme. A stable output wavelength is maintained to within ±5Å across 35°C of temperature change. This is a promising result when compared to a regular VCSEL whose emission wavelength would shift 21Å over the same amount of change in substrate temperature.

The tunable VCSEL is a very promising laser source for coarse WDM data links in a local area network (LAN), especially since we had used the *same* VCSEL

99

throughout this experiment. Three major benefits from using this source in such a network are its capabilities for: active channel stabilization, reconfigurable channel spacing, and cost-effective manufacturing. Not only can we actively stabilize the channel spacing in a LAN now, but we also have the added bonus that these channel spacings are reconfigurable![5] As new nodes (channels or wavelengths) are added into the network, none of the sources really need to be swapped out. The control system can simply bias each node to a different wavelength to accommodate the new node in the network. The tunable VCSEL, if manufactured en masse successfully, can reduce the overall costs of such a WDM system. It would no longer be necessary to handpick and sort laser sources according to their wavelengths, which is a time- and resource-consuming activity as well as the de facto practice in the WDM components industry today.

V   References

[1]   M. Y. Li, W. Yuen, G. S. Li, and C. J. Chang-Hasnain, "High performance continuously tunable top-emitting vertical cavity laser with 20 nm wavelength range," *Electronics Letters*, vol. 33, pp. 1051-2, 1997.

[2]   M. Y. Li, W. Yuen, G. S. Li, and C. J. Chang-Hasnain, "Top-emitting micromechanical VCSEL with a 31.6-nm tuning range," *IEEE Photonics Technology Letters*, vol. 10, pp. 18-20, 1998.

[3]   M. Y. Li, Y. Wupen, G. S. Li, and C. J. Chang-Hasnain, "Effect of process control in oxide-confined top-emitting lasers," presented at 15th IEEE International Semiconductor Laser Conference Cat. No.96CH35896 Conference Digest. 15th IEEE International Semiconductor Laser Conference, Haifa, Israel, 1996.

[4]   D. G. Deppe, D. L. Huffaker, O. Tchang-Hun, D. Hongyu, and D. Qing, "Low-threshold vertical-cavity surface-emitting lasers based on oxide-confinement

---

[5] This is, of course, assuming that the channel spacing is not so dense that inter-channel crosstalk arising from inter-modal dispersion in the fiber would cripple the network.

and high contrast distributed Bragg reflectors," *IEEE Journal of Selected Topics in Quantum Electronics*, vol. 3, pp. 893-904, 1997.

[5]   M. H. MacDougal, J. Geske, L. Chao-Kun, A. E. Bond, and P. D. Dapkus, "Low resistance intracavity-contacted oxide-aperture VCSELs," *IEEE Photonics Technology Letters*, vol. 10, pp. 9-11, 1998.

[6]   S. F. Lim, G. S. Li, W. Yuen, and C. J. Chang-Hasnain, "Intracavity resonant quantum-well photodetection of a vertical-cavity surface-emitting laser," *Electronics Letters*, vol. 33, pp. 597-8, 1997.

[7]   L. A. Coldren and S. W. Corzine, *Diode Lasers and Photonic Integrated Circuits*. New York: John Wiley & Sons, Inc., 1995.

[8]   G. Hasnain, K. Tai, L. Yang, Y. H. Wang, R. J. Fischer, J. D. Wynn, B. Weir, N. K. Dutta, and A. Y. Cho, "Performance of gain-guided surface emitting lasers with semiconductor distributed Bragg reflectors," *IEEE Journal of Quantum Electronics*, vol. 27, pp. 1377-85, 1991.

[9]   K. M. Lascola, W. Yuen, and C. J. Chang-Hasnain, "Structural dependence of the thermal resistance of VCSELs," presented at No.97TH8276 1997 Digest of the IEEE/LEOS Summer Topical Meeting: Vertical-Cavity Lasers/Technologies for a Global Information Infrastructure/WDM Components Technology/Advanced Semiconductor Lasers and Applications/Gallium Nitride Materials, Processing, and Devices Cat. No.97TH8276, Montreal, Que., Canada, 1997.

[10] S. Adachi, *GaAs and Related Materials*. New Jersey: World Scientific, 1994.

[11] D. I. Babic, Y. Chung, N. Dagli, and J. E. Bowers, "Modal Reflection of Quarter-Wave Mirrors in Vertical-Cavity Lasers," *IEEE Journal of Quantum Electronics*, vol. 29, pp. 1950-1962, 1993.

[12] G. S. Li, "Wavelength Selective Detectors for Fiber Optic Communications," in *Applied Physics*. Stanford, CA, USA: Stanford University, 1998, pp. 130.

Mechanical Analysis

Since the topic of this thesis is *micromechanical* lasers, it is imperative that we establish an understanding of the electromechanical behavior of our devices. In section IV C of chapter two, we examined the physical limit to the tuning range of an electrostatically actuated structure. The one-third air gap tuning limit was arrived at in (2.14) without specifying the exact geometry of the movable structure. For reasons of practicality in fabrication, we have chosen the cantilever for the movable structure in our device, though we have only disclosed the dimensions of the cantilever beams in passing without elaborating on how these are arrived. This latter topic will be a major focus in this chapter.

Three mechanical models are offered in this chapter, with each successive one in progressing sophistication. First, lumping the force associated with the capacitance of the cantilever head into a single point load, the beam profile under any tuning bias is analytically derived. Then, distributive forces along the lever arm are taken into account to numerically obtain the beam profile. Results from these two models are compared. The resultant beam profiles for several aspect ratios (varying beam lengths, widths, or thicknesses) are shown. Finally, fringing fields from the parallel plate capacitor are considered and included in the distributed load model. Beam

102

profiles that include these fringing fields will be shown and compared with results from the first two scenarios. To show the validity of our models, these analytical results are compared to the experimental data from our tunable VCSELs.

I   Analysis

In section IV C of chapter two, the one-third rule was derived without any consideration for the dimensions of the arm.[1] For us to develop a feel for the workable dimensions of the cantilever beams and their tradeoffs, we should venture briefly into the world of static mechanics.

The forces and moments associated with a cantilever beam in static mechanics [1] are depicted in figure 5.1 below. We have also included in the figure the relevant coordinate axes to clarify the discussions later on. Table 5.1 outlines the important variables and gives a detailed explanation for them.
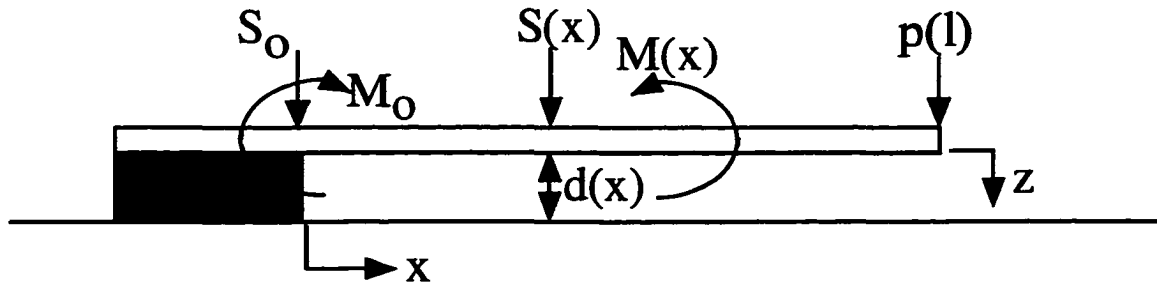
Figure 5.1 Diagram showing the forces and moments in a cantilever beam
The explanations for these variables as well as those relevant to the ensuing discussion are given in the table below.

---

[1] Recalling from figure 2.16, the dimensions of the lever arm were all lumped into the spring constant k in the plots. Although we have found that the one-third rule is independent of the value of k, it has never been discussed here how k is related to the lever arm dimensions.

Variable	Definition/Explanation
S_o	Total force (along z-direction) at the anchor (x=0)
M_o	Total moment (clockwise) at the anchor
p(x)	Force (along z-direction) per unit length
M(x)	Moment (counter clockwise) along length of cantilever
S(x)	Force (along z-direction)
d(x)	Separation of the two capacitor plates along length of cantilever
w(x)	Width of capacitor plate (in y-direction) along length of cantilever
X, Y, Z	Displacement of beam in the three directions
l	Length of beam
t	Thickness of beam (in z-direction), constant with x
I	Cross sectional (in yz-plane) moment of inertia
E	Young's modulus[2] (i.e. the spring constant in Hooke's law for materials)

Table 5.1 Legends of the variables in figure 5.1
Listed in the table are the relevant variables associated with the dimensions of the lever arm. This is to ease the mathematical formulation below.

From figure 5.1, two equilibrium equations can be written:

$$S_o + \int_0^l p(x)dx = 0; \text{and} \tag{5.1a}$$

$$-M_o + \int_0^l xp(x)dx = 0. \tag{5.1b}$$

While (5.1a) states that there is no net force acting on the system, (5.1b) dictates that there is no net moment acting on the cantilever beam, either. (Otherwise the beam would be freely rotating at equilibrium!) Also from figure 5.1, we can deduce the two continuity relations below:

$$\frac{dS(x)}{dx} \equiv p(x); \text{and} \tag{5.2a}$$

$$\frac{dM(x)}{dx} \equiv S(x). \tag{5.2b}$$

---

[2] The Young's modulus for GaAs in the <110> direction on the (100) plane is $121GPa = 1.21e11 \ Nm^{-2}$. [2] This is the value used throughout our analysis.

Together with (5.1a) and (5.1b) and the known boundary conditions, (5.2a) and (5.2b)

give us S(x) and M(x) anywhere along the cantilever beam once p(x) is known. In our

case, p(x) is simply (2.12) divided by the incremental length along the lever arm.

Knowing S(x) and M(x), we need to link the vertical displacement of the beam

Z(x) to either one of them. For that we have to digress from our course and delve into

solid mechanics and elasticity momentarily.

Figure 5.2(a) depicts a uniform prismatic beam undergoing pure bending from

both ends. Figure 5.2(b) shows an enlarged version of a slice of the beam. The x-axis

is defined as the axis of symmetry along the length of the beam.

(a)   (b)
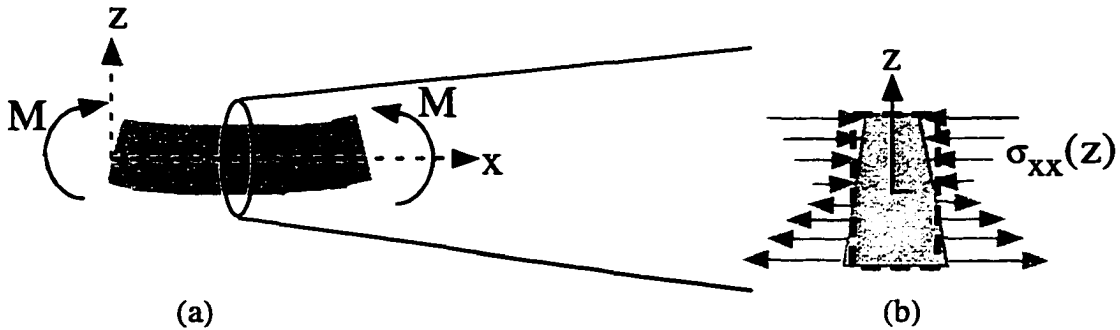
Figure 5.2 A uniform prismatic beam undergoing pure bending
(a) Schematic of the prismatic beam when two equal and opposite moments are
applied at its ends about an axis of symmetry; (b) The enlarged view of one slice
along the beam. In (b), the dashed box is the slice without any bending. The gray
trapezoid is the shape of the deformed slice as a result of the applied stress, denoted
by $\sigma_{xx}(z)$, caused by the externally applied bending moment M at the ends. Note that
$\sigma_{xx}(z)$ is linearly proportional to z.

Equilibrium conditions dictate that the interior stresses and moments at the end

surfaces of the beam be equal in magnitude and opposite in sense to the applied

moment about the z-axis, i.e.

$$M = -\iint (\sigma_{xx} z) dA,$$
(5.3)

where σ_{xx} is the stress in the x-direction caused by a force applied in the same

direction. From figure 5.2(b), σ_{xx} is proportional to z. Letting this proportionality

105

constant be C and substituting the resultant expression for σ_{xx} into (5.3) we have the following:

$$M = -\iint Cz^2 dA = -C\iint z^2 dA \equiv -IC, \tag{5.4}$$

where I is the cross section moment of inertia with respect to the x-axis. Substituting C of (5.4) back into the expression for σ_{xx} we have:

$$\sigma_{xx} = Cz = -\frac{Mz}{I}. \tag{5.5}$$

In an isotropic material with σ_{xx} as the only component in the entire stress tensor, Hooke's law gives the strain components as follows:

$$\gamma_{xx} = \frac{\sigma_{xx}}{E} = -\frac{Mz}{EI}; \tag{5.6a}$$

$$\gamma_{yy} = \gamma_{zz} = -\frac{\upsilon\sigma_{xx}}{E} = \frac{\upsilon Mz}{EI}; \text{and} \tag{5.6b}$$

$$\gamma_{xy} = \gamma_{yz} = \gamma_{xz} = 0; \tag{5.6c}$$

where γ_{ij} is defined as a solid element's fractional displacement in the i-direction relative to its equilibrium length in the j-direction, E the Young's modulus and v the Poisson's ratio of the material. We can explicitly express the definitions of these strain components, and in particular γ_{xx} and γ_{xz}, as below:

$$\frac{\partial X}{\partial x} \equiv \gamma_{xx} = -\frac{Mz}{EI}; \text{and} \tag{5.7a}$$

$$\frac{1}{2}\left(\frac{\partial X}{\partial z} + \frac{\partial Z}{\partial x}\right) \equiv \gamma_{xz} = 0; \tag{5.7b}$$

Integrating (5.7a), we obtain

$$X(x) = -\frac{Mxz}{EI} + X_0(y,z); \tag{5.8}$$

where X_o satisfies the boundary condition of the beam in the other two directions. Using the results in (5.8) and (5.7b) to get

$$\frac{\partial Z}{\partial x} = -\frac{\partial X}{\partial z} = -\frac{\partial}{\partial z}\left(-\frac{Mxz}{EI} + X_o(y,z)\right) = \frac{Mx}{EI} - \frac{\partial X_o(y,z)}{\partial z}; \qquad (5.9)$$

and differentiating (5.9) once with respect to x, we will arrive at our important result below:

$$\frac{\partial^2 Z}{\partial x^2} = \frac{M}{EI}. \qquad (5.10)$$

Incidentally, from calculus the curvature of a given function y=f(x) is given by:

$$\frac{1}{\rho} = \frac{\frac{d^2 f}{dx^2}}{\left[1 + \left(\frac{df}{dx}\right)^2\right]^{\frac{3}{2}}}. \qquad (5.11)$$

If the magnitude of (df/dx) is small compared to unity, the curvature of f(x) is essentially the numerator in (5.11). For deformed beams, the same approximation can be made. Therefore the left-hand side of (5.10) is simply the curvature of the deformed beam.

Equations (2.12), (5.1), (5.2) and (5.10) together with the knowledge of Young's modulus in the relevant crystal orientation would give us the necessary information to formulate the relationship between the applied voltage and the bending profile of any arbitrary cantilever. From these beam profiles, we will be able to determine the bias voltage dependence for both the air layer thickness and the amount of tilt in the movable section of the top DBR. Information about the latter is especially important for us in the optical analysis undertaken in chapter six.

Building upon the foundation in the foregoing discussion, we will now examine three specific cases of the applied load $p(x)$: concentrated load, distributed load with uniform field lines, and distributed load including fringing fields. Calculated results for the three cases will be compared.

II   Concentrated load

First, let's tackle the simplest scenario in which all of the downward electrostatic force associated with the cantilever head can be lumped as a point force applied at the end of a lever arm of fixed width and thickness. In order to solve this problem analytically, we neglect the functional dependence of the plate separation $d(x)$ with the applied tuning voltage. Referring to figure 5.3 and letting this point force be applied at $x=l$, we have the following for the force per unit length, $p(x)$:

$$p(x) = -\frac{\varepsilon V^2}{2d_o^2}[w + A\delta(x - l)]$$ (5.12)

where w is the width of the cantilever, and A is the area of the cantilever head, its resultant electrostatic force is applied as a point source at $x=l$, expressed as a delta function above.
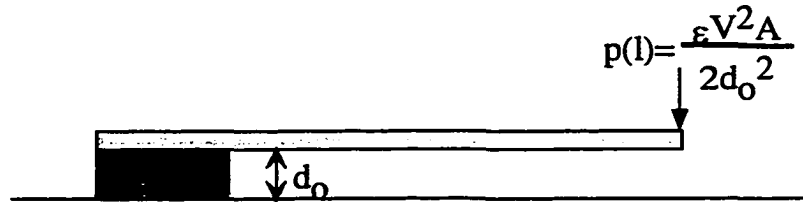

Figure 5.3 Schematic of a cantilever beam under a concentrated load
The concentrated load lumps all of the electrostatic forces associated with the cantilever head together. It is applied at the free end of the lever.

Following the procedure outlined in equation (5.1) to find S_0 and M_0, the total force and moment at the anchor respectively, we arrive at the following:

108

$$S_o = -\int_0^l p(x)dx = \frac{\varepsilon V^2}{2d_o^2}(wl + A); \qquad (5.13a)$$

$$M_o = \int_0^l xp(x)dx = -\frac{\varepsilon V^2}{2d_o^2}\left(\frac{wl^2}{2} + Al\right). \qquad (5.13b)$$

Using the relationship between p(x), S(x) and M(x) in (5.2) we arrive at expressions for S(x) and M(x), respectively the force and moment as a function of position along the cantilever:

$$S(x) = S_o + \int_0^x p(x')dx' = \frac{\varepsilon V^2}{2d_o^2}[w(l-x) + A]; \qquad (5.14a)$$

$$M(x) = M_o + \int_0^x S(x')dx' = \frac{\varepsilon V^2}{2d_o^2}\left[A(x-l) + wl(x-\frac{1}{2}) - \frac{wx^2}{2}\right]. \qquad (5.14b)$$

The expression for M(x) in (5.14b) can be substituted in (5.10) to find the curvature of the cantilever. Integrating the resulting expressions twice with respect to x and using the boundary conditions that the slope and the displacement of the cantilever at the anchor are both 0, we obtain the expression for displacement along the cantilever Z(x):

$$Z(x) = \frac{\varepsilon V^2}{2d_o^2(EI)}\left\{-\frac{x^2}{2}\left(Al + \frac{wl^2}{2}\right) + x^3\left(\frac{A+wl}{6}\right) - x^4\left(\frac{w}{24}\right)\right\}. \qquad (5.15)$$

The I-term in the denominator is the cross sectional moment of inertia for the beam.

For a beam with uniform width and thickness, $I = \frac{wt^3}{12}$. Substituting in x=l to get the displacement at the end of the cantilever, we have for Z(l):

$$Z(l) = -\frac{\varepsilon V^2}{2d_o^2(EI)}\left(\frac{Al^3}{3} + \frac{wl^4}{8}\right) = -\left(\frac{l^3}{Ewt^3}\right)\left(2A + \frac{3wl}{4}\right)\left(\frac{\varepsilon V^2}{d_o^2}\right) \qquad (5.16)$$

109

From the right side of (5.16) we can get a rough idea of how Z(l) depends on the applied voltage and geometry of the cantilever. If we re-cast (5.16) in the form of Hooke's law and substitute the expression for $F_\downarrow$ in (2.12), we have

$$Z(l) = \frac{F_\downarrow}{k_{effective}} = \frac{\left| -\left(\frac{\varepsilon V^2}{2d_0^2}\right)\left(A + \frac{3}{8}wl\right)\right|}{\left(\frac{Ewt^3}{4l^3}\right)}, \qquad (5.17)$$

We should clarify at this point that implicit in Hooke's law is that the restoring force is a consequence of some displacement from equilibrium. To the contrary, (5.17) states that the displacement is an effect of the applied downward force. Strictly speaking, this can be viewed as the linear term in the overall Taylor's expansion of Z(l) on $F_\downarrow$.

Nevertheless, (5.17) is instructive in highlighting two points. First, the effective area of the capacitor is now the sum of the original area of the head and 3/8 of the area of the arm. Not only does the tip see the point source force associated with the area A, it also sees a partial contribution from the arm. Secondly, the effective spring constant is the material's Young's modulus weighted with a geometry-dependent factor.

Moreover, this spring constant of the arm is dependent on $\left(\frac{t}{l}\right)^3$. This aspect ratio is a gauge of the stiffness of the cantilever. Therefore, a short and thick cantilever is more difficult to bend than a long and wiry one under the same force, which is just plain common sense.

The second important point we can derive from (5.17) is the tradeoff between the applied tuning bias, V, and the dimensions of the cantilever beam. For the sake of

110

comparison, let's suppose that the required displacement Z(l) is to remain the same for beams with flexible geometry. Rearranging (5.17), we have the following:

$$Z(l)\frac{\left|\frac{-2d_o^2}{\epsilon}\left(\frac{Ewt^3}{4l^3}\right)\right|}{\left(A+\frac{3}{8}wl\right)} = V^2.$$

$$(5.18)$$

Or, simply put, the voltage required to yield a displacement Z(l) at the tip of the cantilever arm under this approximation is:

$$V_{Z(l)} = \sqrt{Z(l)\frac{\left|\frac{-2d_o^2}{\epsilon}\left(\frac{Ewt^3}{4l^3}\right)\right|}{\left(A+\frac{3}{8}wl\right)}},$$

$$(5.19)$$

Implicit in (5.19) is that if a design constraint is placed on a ceiling for the tuning voltage, only a subset of aspect ratios for the cantilever beam can be used.

III   Distributed load with uniform field lines

In the previous section, we approximated all of the downward forces associated with the head of the cantilever as a point source and analytically solved the five solid mechanics equations using the assumption that d_o in the denominator does not change when V varies. This, of course, is incorrect as the one-third rule found in section IV C in chapter two informs us. Once d_o is allowed to vary with the tuning voltage however, there is no analytical way to arrive at the functional form of the displacement Z(x). We thus have to obtain the displacement profile Z(x) numerically. In the model discussed here, not only is the separation distance between the two capacitor-plates allowed to vary with voltage, but the downward force from the

111

cantilever head is also distributed along the lever length. In other words, the area of

each slice along the length of the cantilever A(x) is taken into account for $F_\perp(x)$ as

well as the separation $d_0 - Z(x)$ of the cantilever from the substrate. See figure 5.4

below for a schematic of this model. Uniform electric field lines are assumed inside

each capacitor slice that (2.12) still hold for the downward electrostatic force.
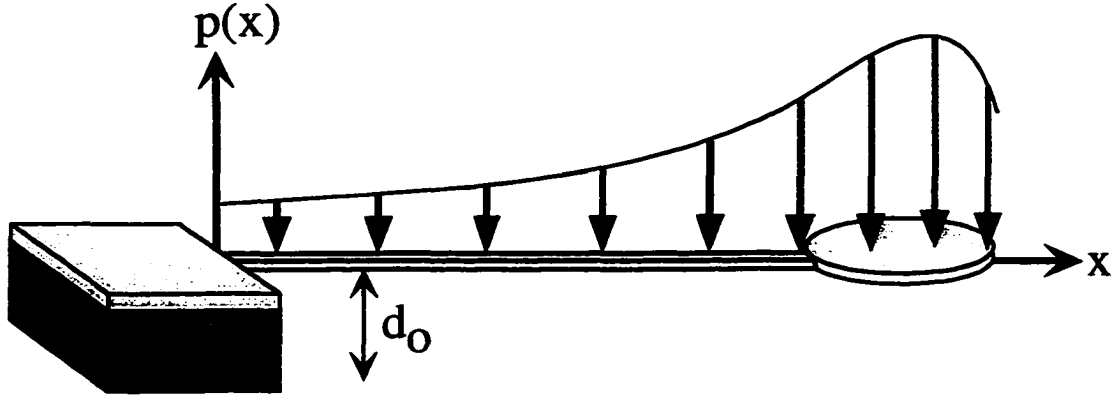
Figure 5.4 Schematic of a cantilever beam under distributed load
Sketched in this figure is the distributed load applied along the length of the beam
(whose axis coincides with the x-axis). p(x) is a function of the beam area, applied
voltage and plate separation, as shown in equation (5.20) below.

The same set of equations (5.1), (5.2) and (5.10) is used as before in our

analytical derivation. However, the correct Z(x) is arrived at through iteration. Let us

detail the steps through this process. First, an applied voltage V_{tune} is assumed and

p(x) along the beam is derived using (2.12):

$$p(x) = -\frac{\varepsilon V_{tune}^2}{2}\left(\frac{w(x)}{(d_0 - Z(x))^2}\right), \tag{5.20}$$

where w(x) is the width of the incremental slice of the capacitor along the beam at x.

Z(x), initially assumed to be zero, is the displacement of the beam at x. (5.20) is then

plugged into the equilibrium equations (5.13a) and (5.13b) to find S_0 and M_0, the total

force and moment at the anchor, respectively. Once S_0 and M_0 are known, equations

(5.14a) and (5.14b) can be used to determine S(x) and M(x) all along the beam.

112

Finally, $M(x)$ is substituted into (5.10) and integrated twice to give us $Z(x)$, with the two boundary conditions again being that both the slope and displacement at the anchor are zero. This concludes one cycle in the iteration.

To determine whether this $Z(x)$ is the steady state solution at V_{tune}, the displacement at the tip of the beam, $Z(l)$, is checked against its value from the previous iteration. If so, we are done. If not, $Z(x)$ is stored and $p(x)$ is re-evaluated in (5.20) using the new $Z(x)$ values until $Z(l)$ stabilizes from one iteration to the next. This numerical approach is shown graphically in a flowchart below in figure 5.5.
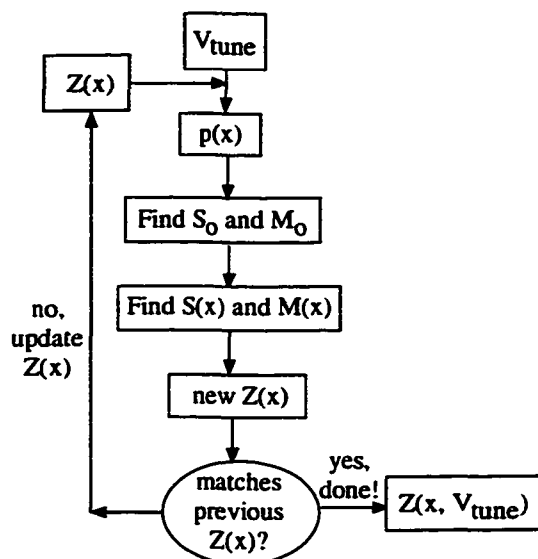
Figure 5.5 Flowchart showing the iterative method used to arrive at the beam profile
This details how the steady state beam profile is arrived at under a bias tuning voltage V_{tune} in the distributive load model

From this analysis, we can determine the beam profile, $Z(x)$, for any V_{tune} at which the beam is stable. Not only can we determine the air gap thickness as V_{tune} varies, but we can also find out the critical voltage V_c, i.e. V_{tune} at which the beam becomes unstable.[3] Shown in figure 5.6 below is the calculated V_c for beams of

---

[3] The instability is easily detected. The value of $Z(l)$ increases with each iteration without bounds. After a couple trips around the flowchart, $Z(x=l)$ can be greater than the original air gap thickness, d_o!

various lengths and three widths: 2, 4, and 8μm. The lever beam is 3μm thick with

the head being a 20μm wide circle.
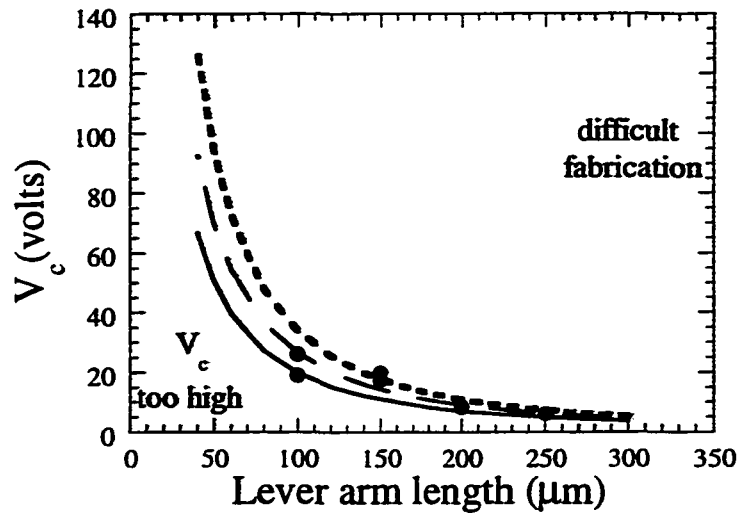
Figure 5.6 V_c for various cantilever beam dimensions: Calculation and experiment
The solid line shows the calculated critical voltage (V_c) for a 2μm wide lever arm. Shown in the thin dashed curve is V_c for a 4μm wide lever arm and in the thick dotted line, V_c for a 8μm wide lever. The black dots show the observed values of V_c from fabricated lasers. The annotated gray areas are not suitable designs, as explained in the paragraph below.

From figure 5.6 shows the magnitude of V_c as the beam geometry is varied.

For beam lengths shorter than 100μm, V_c is greater than 40V. V_c in this regime is not

practical because the tuning junction may suffer reverse breakdown from avalanche

multiplication before then.[4] For beam lengths longer than 250μm, the beams are

unwieldy to fabricate although electrical breakdown of the tuning junction poses no

concern. We therefore have established a range of lengths over which we can design

our practicable cantilevers. The widths are chosen such that standard

photolithography does not pose any serious difficulties, which often means that they

---

[4] For instance, a 1.5μm thick "intrinsic" GaAs region with a background doping of 10^{15}/cm^3 sandwiched in a pn-junction with each doped to 10^{18}/cm^3 would be completely depleted with a reverse bias of 50V. See [3], pp.96-108, especially figure 32.

114

be wider than 3µm across.

Another set of results this analysis provides is the profiles of any cantilever beam at any tuning bias that offers a stable solution, i.e. for $V_{tune} < V_c$. For example, shown in figure 5.7 below is a set of beam profiles under tuning bias close to the point of instability ($V \sim V_c$). Nine different beam geometries are calculated, including three lengths (50µm, 100µm, and 200µm) and three widths (2µm, 4µm, and 8µm). As before, the heads of these 3µm thick levers are 20µm wide circles in these calculations. The original air gap is 1.5µm thick.
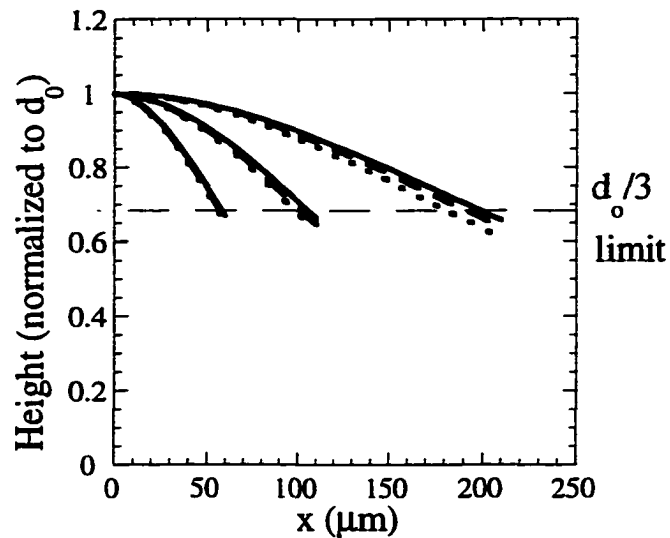
Figure 5.7 Profiles of various beam dimensions near V_c, plotted as a function of distance from the anchor
Profiles of nine beams including three lever lengths (50, 100, and 200µm) and three widths (2, 4, and 8µm) are shown above. The solid lines represent the 2µm wide beams; the dashed lines, the 4µm wide beams; and the dotted lines, the 8µm wide beams. Note that they all break the one-third rule derived in chapter two.

An immediate noticeable result from this figure is that the ends of these cantilever beams all exceed the one-third rule we derived in chapter two, section IV C.

This is an expected result once we realize the assumptions made in arriving at the rule:

Neither the dimensions of the lever nor its contribution to the (downward) electrostatic attractive force was considered. The effects of the arm had been lumped into an

115

arbitrary spring constant k that only contributes to the (upward) restoring mechanical force. The opposing electrostatic attractive force was considered only with the contribution from the head of the cantilever. Furthermore, the entire downward force was applied at the center of mass of the head. Compared to the earlier simplistic model, the distributive load model discussed in this section considers the downward force contribution all along the beam, from both the arm and the head. Comparing the "center-of-mass" at which the downward force is applied from these two different considerations, that from the distributive load model is further back towards the anchor than that from the lumped load model because of all the extra force contributions due to the arm. Consequently, when the center of mass from the distributive load model has been displaced one third of the original air gap, the actual head actually would exceed that one-third limit. Therefore, a cantilever could have a maximum displacement that exceeds the one-third limit (albeit only by a little[5]). Ultimately the tradeoff for this advantage is the tilt associated with the mirror.

Finally, to compare the results between this model and its concentrated load predecessor described in section 5.2, we show in figure 5.8 the relationship between the applied tuning voltage and the air gap thickness under the mirror. We can see that the concentrated load model in general overestimates the voltage needed to actuate the lever. In some cases, the estimate is quite crude.

---

[5] We can see that the center-of-mass for the cantilever in the distributed load model is not as far back as we thought if we actually carried out the integral over the whole length of the beam. This is because the electrostatic attractive force per unit area (pressure) is not constant along the beam. Since the tip of the head is closer to the "ground" capacitor plate than the part of the arm near the anchor, the head experiences a greater electrostatic pressure than the part of the arm near the anchor. This differential pressure actually gives the cantilever head more weight than the arm.

116
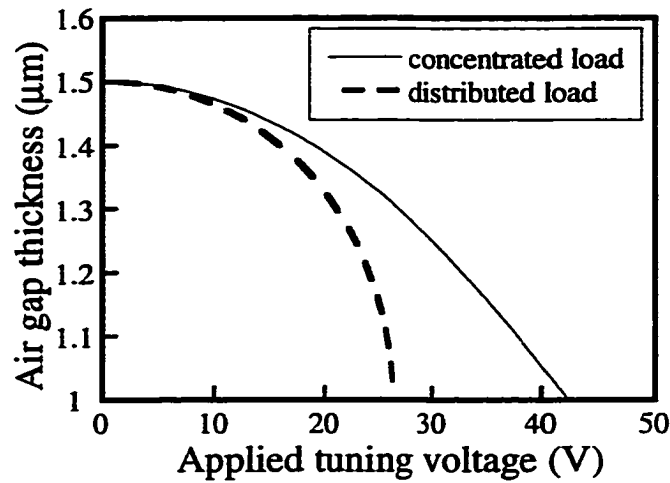
Figure 5.8 Air gap thickness under the cantilever head as a function of the applied tuning voltage for the two models discussed thus far

The specific parameters used for this calculation: $w=4\mu m$, $l=100\mu m$, $t=3\mu m$, $d_o=1.5\mu m$, circular head diameter = $20\mu m$.

IV Distributed force model with fringe field

Although the distributed load model discussed in the previous section is a significant refinement to its lumped load predecessor, one more improvement is necessary to make the model realistic. One important assumption in the last model lies in the use of a large area parallel-plate capacitor in calculating the electrostatic downward force. Consequently, uniform electric field lines between the plates are assumed. This is depicted in figure 5.9(a).

(a)   **(b)**
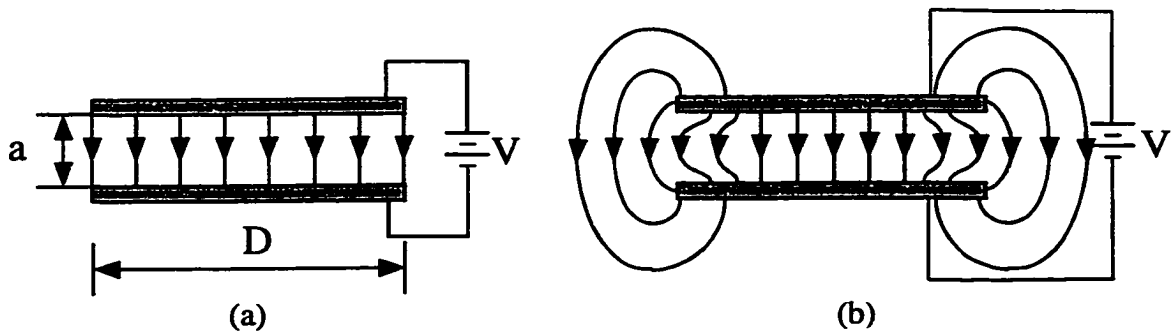
Figure 5.9 E-field lines in parallel plate capacitors

(a) A parallel-plate capacitor with uniform E-field lines; and (b) a parallel-plate capacitor with fringing fields.

117

Of course, if the dimensions for the parallel-plate capacitor are such that the separation between the plates (a in figure 5.9) is not much smaller than one side of the plates (D in figure 5.9), fringing fields on the ends of the plates would contribute additional force. This is shown in figure 5.9(b).[4] In this section, we shall examine in detail how strong an effect this fringing field has on the electrostatic force and how much of a correction is necessary to take the fringing field into account properly.

The treatment in securing analytic solutions of electrostatic field/potential problems with straight-line boundaries requires conformal mapping, specifically the Schwarz transform.[5] Essentially, the Schwarz transformation maps the interior of a polygon in one complex plane (z-plane in figure 5.10(c) below) to the upper half of another complex plane (w-plane in figure 5.10(d) below). The mathematical definition of the Schwarz transform is given as follows:

$$w - w_i = A(z - z_i)^n,$$ (5.21)

where $\infty > n \geq 0.5$ for a unique one-to-one mapping between these two planes. As we can see in figure 5.10(d), the vertices of the polygon in the z-plane are transformed to lie on the real-axis of the w-plane. The beauty of this transform is that some of the more difficult vertices can be cleverly transformed to lie at infinity on the u-axis to ease calculation difficulties.

Since this section is focused on the effect of the fringing field on the distributed load model in our cantilever, we shall only summarize results from using the Schwarz transform to find the electric field for our specific geometry. For a detailed discussion and explanation, the reader should consult [6] for a complete treatment of this problem.

118
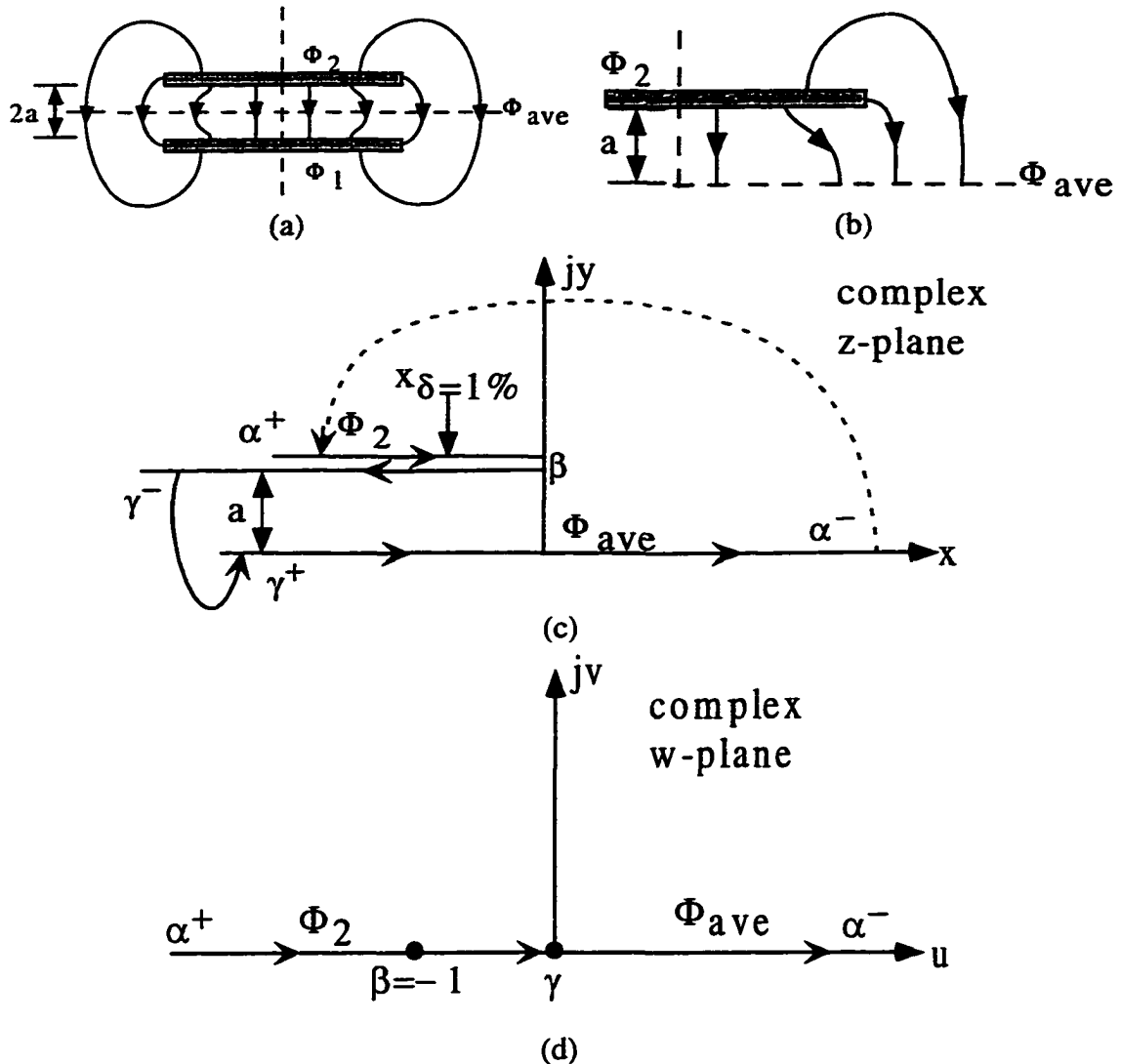
Figure 5.10 Mapping a parallel plate capacitor using the Schwarz transform
(a) A parallel plate capacitor. (b) Because of symmetry, only a quarter of the problem is necessary to solve for the electric field everywhere. (c) The convex polygon (triangle in this case) in the complex z-plane represents the capacitor in (b). The three vertices (α, β, γ) and the paths are labeled. In (d), the transformed version of this geometry is shown with the corresponding vertices labeled. In the w-plane, vertex α has been conveniently pushed off to $\pm \infty$ on the real axis while vertex β is at w = -1, and γ is located at the origin.

Figure 5.10 above shows the evolution of a parallel-plate capacitor from its physical form into a "convex" polygon on the z-plane and eventually into the Schwarz transformed geometry. Notice that under this arrangement, the entire negative real axis (u-axis) in the w-plane is at potential Φ_2 while the positive u-axis sits at potential

119

$\Phi_{ave} = \dfrac{\Phi_1 + \Phi_2}{2}$. The mapping function between the two planes, after substituting

the location of the vertices to ensure a unique one-to-one correspondence, is:

$$z = \frac{a}{\pi}(1 + w + \ln w). \tag{5.22}$$

The boundary conditions of the potential profile in figure 5.10(d) form a popular textbook problem in electromagnetics. The magnetostatic potential due to a line current or, alternatively, the electrostatic field between two coplanar potential surfaces with an infinitesimal gap in-between can be represented by the complex function [6]:

$$P = -\frac{j}{\pi}(\Phi_2 - \Phi_{Ave})\ln w + \Phi_{Ave}. \tag{5.23}$$

The electric field vector is then found by differentiating (5.23) with respect to z:[6]

$$E = -\overline{\left(\frac{dP}{dz}\right)} = -\overline{\left(\frac{\dfrac{dP}{dw}}{\dfrac{dw}{dz}}\right)} = -j\frac{\Phi_2 - \Phi_{Ave}}{a}\overline{\left(\frac{1}{1+w}\right)} \equiv -j\frac{E_o}{(1+w)}. \tag{5.24}$$

E_o is the field strength between the parallel plates under the assumption of uniform field lines. Note that from (5.24), the electric field is purely parallel to the imaginary axis. Along the negative real axis up until u=-1, E is positive. For u>-1, E is negative. At u=-1 (vertex β), E is infinite, as in any convex corner of a polygon. We can also use (5.24) to determine the location in the parallel-plate capacitor at which the practical limit of uniform field is reached.

---

[6] This is a special property of quantities like the complex electric field strength and potential, which are harmonic conjugate functions satisfying the Laplacian differential equation.

To proceed, suppose that we would like to know where along the plate the electric field is $\delta\%$ above E_0. Substituting this value of E on the left-hand side of (5.24), we have:

$$\left(1+\frac{\delta}{100}\right)E_0 = -\left|j\frac{E_0}{1+u_\delta}\right|. \tag{5.25}$$

For $\delta/100 \ll 1$, we can approximate the quantity inside the parentheses on the left hand

side as $\dfrac{1}{1-\dfrac{\delta}{100}}$ and solve for u_δ:

$$u_\delta = -\frac{\delta}{100}. \tag{5.26}$$

Note that u_δ is negative because we are considering the position along the underside of the top capacitor plate (between β and γ in figure 5.10(c).) Substituting $w = u_\delta$ in (5.22) to find the corresponding location in the z-plane we have the following:

$$z_\delta = \frac{a}{\pi}\left[1-\frac{\delta}{100}+\left(\ln\frac{\delta}{100}+j\pi\right)\right] = ja - \frac{a}{\pi}\left[\ln 100 + \frac{\delta}{100} - (1+\ln\delta)\right]. \tag{5.27}$$

For a 1% increase in field strength from the uniform field case, $z_\delta = x_\delta + ja$. See figure 5.10(c) and its correspondence to figure 5.10(b). We find that $x_{\delta=1\%}=1.151a$. In general, the fringing field encroaches into the homogeneous field region by roughly the same order as the gap size.

Now we are ready to solve for the problem originally posed at the beginning of this section. What is the effect of the fringing field on the attractive electrostatic force? We need to find the extra dielectric flux due to the fringing field and relate this flux to the downward force in our model.

To start off, we can use the imaginary part of the complex potential solution in (5.23), which is the dielectric flux. The total dielectric flux between where the uniform field stops, assuming this to be at the value of $u_{\delta=1\%}$ found in equation (5.26) for the present, and the image of vertex β in the w-plane, $u_\beta=-1$ is:

$$\Psi\Big|_{u_\beta}^{u_\delta} = -\varepsilon\frac{\Phi_2 - \Phi_{Ave}}{\pi}\big[\ln u_\delta - \ln u_\beta\big] = \varepsilon\frac{\Phi_2 - \Phi_{Ave}}{\pi}\ln\frac{1}{|u_\delta|}$$
$$= \frac{\varepsilon(\Phi_2 - \Phi_{Ave})}{\pi}\ln\frac{100}{\delta}.$$
(5.28)

If we compare (5.28) to what one would get in the case of a uniform field from $z_{\delta=1\%}$ to β in figure 5.10(c), we have:

$$\Psi_{uniform}\Big|_\beta^{z_\delta} = |x_\delta||E_o| = \frac{\varepsilon(\Phi_2 - \Phi_{Ave})}{\pi}\left[\ln 100 + \frac{\delta}{100} - (1 + \ln\delta)\right].$$
(5.29)

The difference between (5.28) and (5.29) is the extra dielectric flux due to fringing field. This correction is very simple:

$$\Delta\Psi_{fringe}\Big|_\beta^{z_\delta} = \frac{\varepsilon(\Phi_2 - \Phi_{Ave})}{\pi}\left(1 - \frac{\delta}{100}\right).$$
(5.30)

The fractional increase of the dielectric flux due to this fringing field over the case of uniform field lines is:

$$\frac{\Delta\Psi_{fringe}}{\Psi_{uniform}}\Bigg|_{edge}^{z_\delta} = \frac{1 - \dfrac{\delta}{100}}{\ln 100 + \dfrac{\delta}{100} - (1 + \ln\delta)}.$$
(5.31)

Shown in figure 5.11 below is this fractional increase of the flux plotted against δ. For $\delta=0.1\%$, this increase amounts to almost 17% increase in the dielectric flux! Another useful quantity $|x_\delta|/a$ from (5.27) is also plotted on the second y-axis in figure 5.11. For $|x_\delta|=a$, $\delta=1.62\%$ and the fractional increase in the dielectric flux is 31.6%! This is shown in figure 5.11 with a dotted line to guide the eye.

122
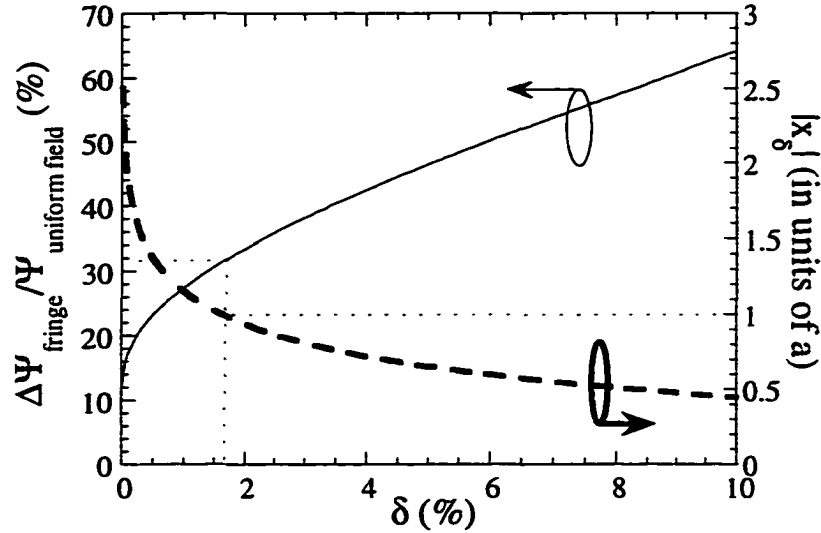
Figure 5.11 $\dfrac{\Delta\Psi_{fringe}}{\Psi_{uniform}}\bigg|_{edge}^{z_\delta}$ in equation (5.31) and x_δ in equation (5.27) as a

function of δ

The additional dielectric flux due to fringing fields encroaching into the side of the parallel plate by an amount equal to the plate separation is about 32% of the uniform field case.

The only task that remains is to relate this extra flux to the capacitance. This is readily rendered through the definition of capacitance and the use of Gauss' law since the electric flux on a surface is just the total charge enclosed! We now know that the extra electric flux from the edge of the plate with a width that is equal to the gap is 32%. The cross section of our cantilever can be modeled as three capacitors in parallel as shown in figure 5.12.

(a)   (b)
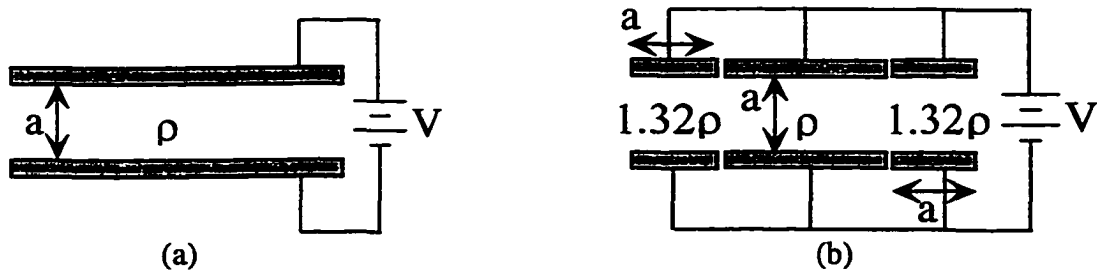
Figure 5.12 Cross section view of a slice along our cantilever beam
When fringing field is considered, the (a) original parallel plate capacitor becomes (b) three capacitors in a parallel configuration. The two on the side have widths equal to the gap distance and a higher effective charge density (1.316 times) than the middle capacitor.

123

Using this model to account for the fringing field, we can expect that the required tuning voltage to actuate the cantilever by a fixed distance is smaller than what both of the previous models gave. The fringing field provides extra attraction between the cantilever head and the ground plane. Simply put, if one considers the fringing field, the charge density per unit length along the beam is larger for the same tuning bias. Shown in figure 5.13 below is a comparison between this model and the two in figure 5.8.
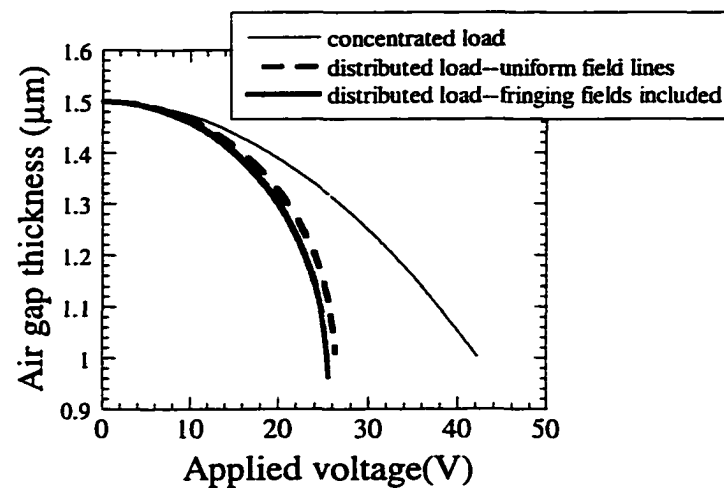
Figure 5.13 Air gap thickness under the cantilever head as a function of the applied tuning voltage for the three cases discussed in this chapter
Dimensions for the cantilever are the same as those used in figure 5.8: l=100μm, w=4μm, t=3μm and the circular head has a 20μm diameter. Including the fringing field does not affect the outcome of the distributed load model much.

Comparing results from the two distributed load models, the tuning voltage only differs by ~1V for the beam dimension that we use above. The same comparison has been made with other beam lengths and widths. We find that the maximum difference in the tuning voltages between the two distributed load models amounts to only about 4%. This may be smaller than we previously thought, since the 31.6% figure three paragraphs ago sounds pretty high. However, because fringing effects only extend into roughly the same distance as the height of the gap, a large correction

124

would result only if the width of the capacitor is on the order of the gap size. In our case, the head of the cantilever has the largest area and thus contributes most of the downward force. The width of the head is roughly 10 times that of the air gap distance, therefore the fringing field doesn't yield much correction. The narrower width of the arm can cause the effect of the fringing field to seem larger. Fortunately, the arm is farther from the substrate than the head, so its contribution of the total electrostatic force is not large anyway.

V   Experimental verification

Three different mechanical models have been discussed to understand how cantilever beams of different geometry behave under various tuning biases. The ultimate test, though, is to compare our calculated results with experimental data. Shown in figure 5.14 is the observed wavelength as a function of tuning voltage from a tunable VCSEL with a single transverse mode. Also plotted in figure 5.14 is the calculated FP-wavelength of the VCSEL structure as a function of V_{tune}. The air gap thickness has already been incorporated into the VCSEL structure to determine the appropriate FP-wavelength. A good match is found. The cantilever here is 100μm long by 3μm wide and 3μm thick. The original air gap thickness is 1.4μm. No fitting parameter is used. The good match found between experimental data and calculations shows that our electrostatic-mechanical model is sufficiently accurate.
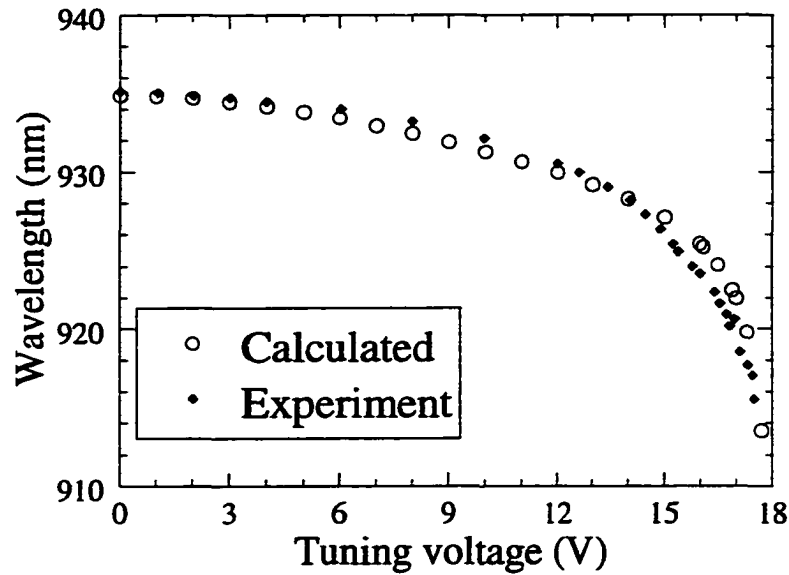
Figure 5.14 Experimental verification of our micromechanical analysis
The FP-wavelength is calculated from the air gap thickness under the lever head as the tuning voltage is varied. No fitting parameter has been used. Good agreement is found between our calculations and experimental results.

VI Summary

The preceding sections have focused on the mechanical analysis of the forces in an electrostatically tuned cantilever structure. Of course, shapes other than the cantilever structure can be used as well. One notable conclusion should be made here. Because it has a free end, the cantilever requires less force to displace than other equivalent mechanical structures (having the same thickness and area) with multiple supports. This is because no internal forces can exist at the free end of the cantilever to counter the applied tuning force, unlike the case for multiply-supported mechanical structures.

In this chapter, we have analyzed the electrostatic-mechanical properties of a cantilever beam. Three models were introduced. First we lumped all of the electrostatic force from the head into a point source applied at the end of a uniform cantilever beam. Assuming small displacements, i.e. the air gap size doesn't change

126

much, we were able to derive an analytical expression for the displacement at the end of the beam and from it, preliminary design rules for the workable dimensions of the lever arm.

This model is then refined by letting the air gap size vary along the lever length. It subsequently evolves into a distributed load model. The beam is sliced along its length and uniform electric field lines (the case for a large area parallel-plate capacitor with a small separation between the plates) are assumed under each slice. This model is further improved on when fringing fields from the edge of these slices are considered. Notice that this model is equally valid for a parallel plate capacitor that has an infinite bottom plate as in figure 5.10(b). This is close to the physical scenario for our cantilever head, which hovers over a much bigger mesa plane.[7] Furthermore, adding the fringing field correction only lowers the tuning voltage by at most 4% in our distributed load analysis. Calculated results are compared against the experimentally observed emission wavelength as a function of the tuning bias. Good agreement is observed between our data and the distributed load model.

At this point, we should briefly consider one more issue. In all of our analyses so far, it was assumed that all the space charge of either polarity is located in one plane, i.e. no distributed space charges like those inside the depletion region of a reverse-biased junction. A quick back-of-an-envelope calculation reveals that the total depletion width into the p- and n-sides of the junction at thermal equilibrium under no tuning bias is on the order of 56nm ($N_a = N_d = 1e18cm^{-3}$ in GaAs), which is miniscule compared to the ~1μm air gap thickness. Even when we consider a high applied bias

---

[7] The reader is referred to the scanning electron micrograph at the end of chapter four for verification.

127

voltage of 30V, the total depletion width would still be only ~0.26μm. Does this mean then that we need to adjust the plate separation in our calculations by adding the depletion widths on either side of the tuning junction to the physical thickness of the intrinsic region? Here I offer a picture to argue that it is not necessary to adjust the plate separation from the physical thickness of the air gap. Shown in figure 5.15(a) below is a picture of our tuning junction under reverse-bias. The distributed space charges are depicted pictorially. The resultant electric field lines are shown schematically also.

(a)   (b)
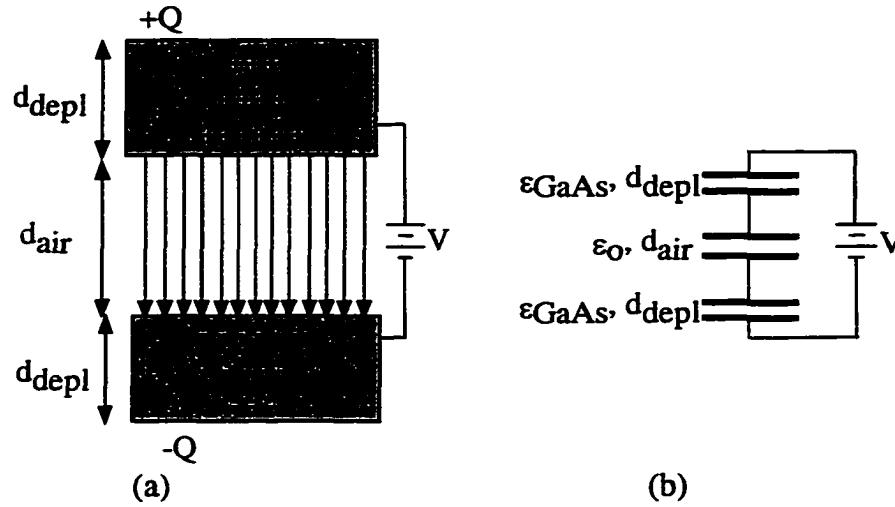
Figure 5.15 Space charge considerations: Capacitor separation
Shown in (a) is our reverse-biased junction with depletion region on either side of the air gap. (b) Equivalent circuit model.

In figure 5.15(b), we have an equivalent circuit for the scenario in part (a), which consists of three capacitors in series. The equivalent capacitance is:

$$C_{equ} = \frac{1}{\dfrac{2}{C_{GaAs}} + \dfrac{1}{C_{air}}} = \frac{1}{2\dfrac{d_{GaAs}}{\varepsilon_{rGaAs}\varepsilon_o A} + \dfrac{d_{air}}{\varepsilon_o A}} = \frac{\varepsilon_o A}{2\dfrac{d_{GaAs}}{\varepsilon_{rGaAs}} + d_{air}}$$

$$= \frac{\varepsilon_o A}{d_{effective}} \sim \frac{\varepsilon_o A}{2\left(\dfrac{0.13\mu m}{13}\right) + 1\mu m}. \tag{5.32}$$

128

The equivalent capacitance in (5.32) is dominated by the smallest capacitor of the three, which is the air capacitor in the middle. Physically this is because most of the reverse voltage is dropped across the air gap. Therefore, we can safely neglect the depletion widths into both ends of the p-i-n tuning junction.

Lastly, the reader may ask why we would want to go through so much material just to match one set of experimental data with theory? There is actually another motivation for deriving the profiles of a specific cantilever beam as it is tuned. Through these calculations, we can quantify the exact tilt in the movable mirror across a VCSEL structure's tuning range and understand what, if any, the tilt limits are. In the next chapter, we will use the tilt from the profiles we calculate here to quantify optical losses due to this tilt in our cantilever structure.

VII References

[1]   R. L. Bisplinghoff, J. W. Mar, and T. H. H. Pian, *Statics of Deformable Solids*. New York: Dover Publications, Inc., 1965.

[2]   S. Adachi, *GaAs and Related Materials*. New Jersey: World Scientific, 1994.

[3]   S. M. Sze, *Physics of Semiconductor Devices*, Second ed. New York: John Wiley & Sons, 1981.

[4]   S. Ramo, J. R. Whinnery, and T. V. Duzer, *Fields and Waves in Communication Electronics*, Second ed. New York: John Wiley & Sons, 1984.

[5]   R. V. Churchill and J. W. Brown, *Complex Variables and Applications*, Fifth ed. San Francisco: McGraw-Hill Publishing Company, 1990.

[6]   E. Weber, *Electromagnetic Fields: Theory and Applications, Volume 1 -- Mapping of Fields*, vol. 1. New York: John Wiley & Sons, Inc., 1950.

Optical Modal Analysis

A detailed mechanical analysis of the tunable VCSEL has been given in the last chapter. An equally important aspect of the tunable VCSEL is its optical properties. Specifically, there are three questions we would like answered. First of all, at what cost has tunability come in our device? Does it suffer more optical loss than a regular VCSEL? If so, how much extra loss? Secondly, what is the optical loss for the tunable VCSEL across its tuning range? Third, our use of a cantilever as the micromechanical structure has raised much speculation about the viability of such a VCSEL. As the cantilever beam is lowered when tuned, tilt is introduced into the top mirror of the VCSEL. It has been thought that the optical loss due to this tilt would keep a tunable VCSEL from lasing. Therefore, one needs to know the amount of tilt loss in this structure. These questions will be addressed in this chapter.

Before we proceed, the formalism with which we begin to tackle these questions is introduced. A general overview of our scheme is first given. Each individual component within the framework of our approach will be described in detail subsequently. Calculation results are then presented and physical explanations are given. Finally, experimentally derived data are to be compared with results from our numerical analyses.

130

I Diffraction formalism

The ultimate questions we intend to address in this chapter have to do with optical losses in our tunable VCSEL structure. Contributing to the total optical loss in a VCSEL are the losses through the mirrors, either by absorption or external coupling, and diffraction of the optical mode throughout the structure. We expect the mirror loss component to vary as the lasing wavelength is tuned. This was briefly discussed in section II of chapter two. Figure 2.7 showed how a typical DBR's reflectivity varied as a function of wavelength and air gap thickness. It is important to note that figure 2.7 was calculated using only normal incident plane waves. Therefore, an additional component that constitutes optical loss for a cavity mode, i.e. that due to diffraction, was not included in figure 2.7. For a more accurate picture, we must include plane wave components that make up the cavity mode other than just the normal-incident plane wave when analyzing the optical loss. We shall briefly discuss the background of the formalism in this section.
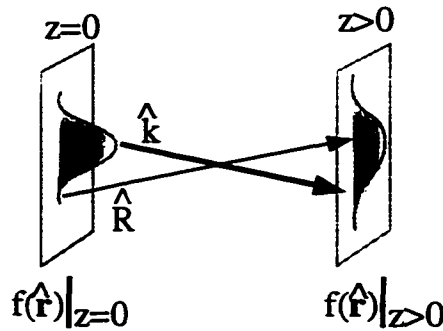
Figure 6.1 Propagation of an optical mode between two planes
If the beam profile at the z=0 plane is known, its field strength at a plane distance z away can be completely described by the Rayleigh-Sommerfeld diffraction formula. After references [1] and [2].

As shown in figure 6.1 above, propagation of a monochromatic beam with wave vector $\bar{k}$ and a known two-dimensional field distribution $f\left(\hat{r}\big|_{z=0}\right)$ at an arbitrary

plane z=0 will result in a field distribution $f\left(\vec{r}\big|_{z>0}\right)$ that can be arrived at using the

Rayleigh-Sommerfeld diffraction formula over the entire z=0 plane [1],[2]:

$$f\left(\vec{r}\Big|_{z>0}\right) = \frac{k}{i2\pi}\iint f\left(\vec{\rho}\Big|_{z=0}\right)\frac{e^{i(k|\vec{R}|)}}{|\vec{R}|}\cos\left(\vec{z}\cdot\vec{R}\right)d\vec{\rho}. \tag{6.1}$$

The wave vector of the beam, $\vec{k}$, can be decomposed into $\vec{k}_r + \vec{k}_z$, where the z-axis is

in the direction of propagation of the optical beam and the r-vector is in the plane

perpendicular to the z-axis. At the plane distance z away from the origin, wave vector

$\vec{k}$ would have undergone $\vec{k}\cdot\vec{R}$ of phase shift, where $\vec{R}$ is the vector from each starting

point on the z=0 plane to all possible destination points on the z>0 plane (thus the 2-D

integral).

Reference [2] explains the formulation of scalar diffraction in a framework

based on linear filter theory. In essence, the complex field distribution across any

plane can be Fourier-analyzed with the various Fourier components identified as plane

waves travelling in different directions. Thus, the complex field amplitude at any

point can be calculated by adding the contributions of these plane waves, taking due

account of the phase shifts undergone by each in propagating to the point of interest.

Therefore, the propagation phenomenon can be regarded as a linear spatial filter, a

result guaranteed by the linearity and superposition of the wave equation.

In the paraxial limit, i.e. $\left|\vec{k}_r\right| << \left|\vec{k}_z\right|$ and $\vec{R} \approx \vec{z}$, the phase change for each

plane wave would be:

132

$$\vec{k} \cdot \left|\vec{R}\right| \approx k_z z = z\sqrt{\left(k^2 - k_r^2\right)} = kz\sqrt{1 - \left(\frac{k_r}{k}\right)^2}$$

$$\approx kz\left(1 - \frac{k_r^2}{2k^2}\right) = kz - \frac{k_r^2}{2k}z. \tag{6.2}$$

Thus the linear transfer function to the propagation phenomenon in the paraxial limit is the exponentiation of the phase factor in (6.2):

$$H(k_r) = e^{i(k - \frac{k_r^2}{2k})z}. \tag{6.3}$$

Note that implicit in this derivation is the propagation of plane waves over the distance of several wavelengths. This is so that contributions of any evanescent waves may be safely neglected. In Fourier space, the complex field content of the two planes z=0 and z>0 then have the following simple relationship:

$$F\left(k_r\big|_{z>0}\right) = H(k_r)F(k_r). \tag{6.4}$$

Equation (6.4) is an important result upon which we base our analysis in the subsequent sections in this chapter.

II   Modal reflection off a DBR

Using equation (6.4), the authors of reference [3] have developed a methodology with which diffraction loss in the DBR structure of a VCSEL is formulated. Specifically they were interested in the reflectivity of an optical mode from the DBR. In that case, a known two-dimensional spatial field distribution is assumed. This mode is then decomposed into its plane wave components that upon reflection from the DBR structure, each would experience a reflected amplitude and phase appropriate to its incident angle. For example, shown in figure 6.2 is the complex reflectivity of a 30.5 pair thick AlAs/GaAs DBR as a function of the plane

133

wave incident angle for both transverse-electric (TE) and transverse-magnetic (TM)

polarizations. This reflectivity is calculated using a transmission matrix method

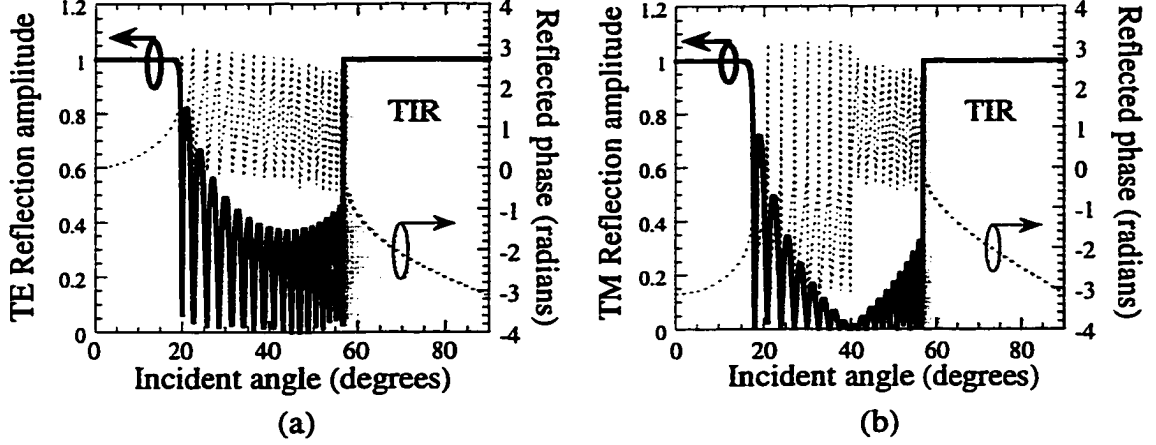commonly used for multi-layered media. [4],[5]

(a)   (b)

Figure 6.2 Reflection amplitude and phase for a DBR as a function of incident angle for both TE and TM polarizations
Reflection amplitude (thick solid line) and phase (thin dashed line) vs. incident angle for a (a) transverse electric and (b) transverse magnetic plane wave at the design wavelength of 950nm. The DBR is a 30.5 pair thick GaAs/AlAs with both incident and exit media being GaAs. Total internal reflection (TIR) is shown as the gray region above 56.7° (where |R| = 1).

For an optical mode $f_{inc}(\vec{r})$ impinging on a DBR structure, the effective

reflectivity of the reflector for that mode, i.e. the DBR's modal reflectivity, is defined

in [3] as the overlap integral between itself and its reflected reincarnation $f_{ref}(\vec{r})$:

$$\kappa = \frac{< f_{inc}(\vec{r}) | f_{ref}(\vec{r}) >}{< f_{inc}(\vec{r}) | f_{inc}(\vec{r}) >} \equiv \frac{\int f_{ref}(\vec{r}) f_{inc}^{*}(\vec{r}) d\vec{r}}{\int f_{inc}^{*}(\vec{r}) f_{inc}(\vec{r}) d\vec{r}}, \tag{6.5a}$$

which, according to (6.4) is the following in the Fourier domain:

$$\kappa = \frac{\int F_{ref}(k_r) F_{inc}^{*}(k_r) e^{i(k-\frac{k_r^2}{2k})z} dk_r}{\int | F_{inc}(k_r) |^2 dk_r}. \tag{6.5b}$$

We can evaluate (6.5b) at the plane where the DBR structure physically "begins" such

that the beam propagation through the penetration depth z/2 of the mirror and the

134

subsequent reflection are taken into account. This is depicted in schematic form in figure 6.3 below.
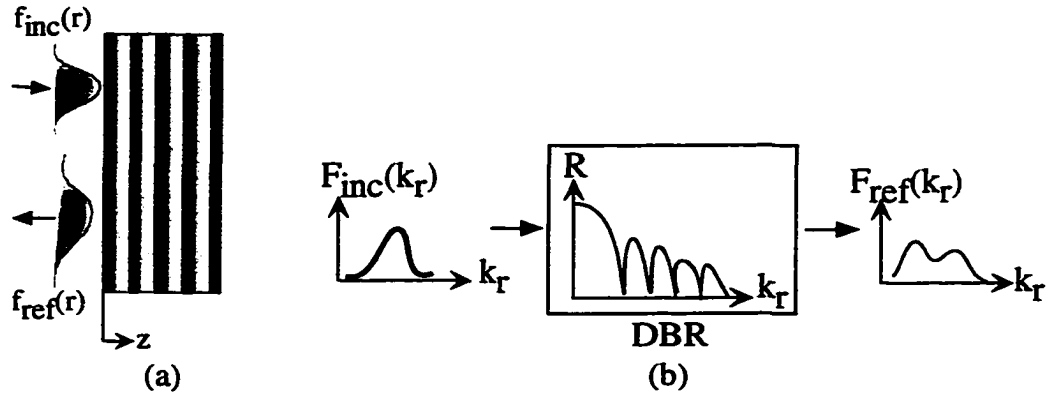
Figure 6.3 Reflection of an optical mode off a DBR
(a) Physical picture, and (b) the schematic showing our numerical approach suggested by equation (6.4).

In this scenario, the reflected complex field amplitude is simply the complex product of the DBR reflectivity and the incident mode in Fourier-space:

$$F_{ref}(k_r) = R(k_r)F_{inc}(k_r).$$

(6.6)

We can see from figure 6.2 that the reflectance across the stop band (near normal incidence) of a nominal DBR structure is fairly constant. Therefore, if we have a well-behaved paraxial beam (half angle < 5.7°), $R(k_r)$ can be approximated as a constant with the value of the normal incident plane wave reflectivity, r_{norm}. Equation (6.6) could then be simplified to (6.7):

$$F_{ref}(k_r) = r_{norm}F_{inc}(k_r),$$

(6.7)

such that (6.5b) is now the following:

$$\kappa = r_{norm}e^{ikz}\frac{\int |F_{inc}(k_r)|^2 e^{-i\frac{k_r^2}{2k}z}dk_r}{\int |F_{inc}(k_r)|^2 dk_r} \equiv r_{norm}e^{ikz}\gamma_{inc};$$

(6.8)

where

135

$$\gamma_{inc} \equiv \frac{\int \left| F_{inc}(k_r) \right|^2 e^{-i\frac{k_r^2}{2k}z} dk_r}{\int \left| F_{inc}(k_r) \right|^2 dk_r}. \tag{6.9}$$

In essence, γ_{inc} on the right hand side of (6.8) embodies the diffraction properties of the optical mode $f_{inc}(\vec{r})$ through the penetration depth into the DBR and back.

In general, κ is very close to unity for an eigenmode of a laser cavity due to the high finesse (>300) necessary for lasing to occur. It is thus easier to define coupling loss [3] as a figure of merit. Our definition for this coupling loss is:

$$\alpha_{coupling} = 1 - |\kappa|^2. \tag{6.10}$$

A   Validity of our analysis

In [3], the complex reflectance of the DBR is arrived at analytically because the DBRs considered are made up of exactly quarter-wave thick layers. We have chosen to calculate the DBR complex reflectance numerically to allow for more freedom in our calculations later on[1]. Before we move on to solve the more complex problems, the first issue at hand is to ensure that our method produces results that agree with those published and shown to be correct. This agreement is shown in figure 6.4(b) [3]. κ for a DBR consisting of varying number of AlAs/GaAs layers centered at 0.98μm is calculated for a TEM_{00} mode that emerges from air-clad waveguides 5μm and 10μm across as shown in figure 6.4(a).

---

[1] Our tuning range can take the FP-wavelength of the structure significantly away from the center wavelength of the DBR. Recall that the thickness of the air layer in the top DBR can vary from ~1.0μm to 1.5μm! Thus, analytical solutions for the complex reflectance of these DBRs then would become extremely complicated. What we have done is a lot simpler: We calculate the complex reflectance of each DBR at the wavelength of interest using the transmission matrix method and create a look-up table that holds its reflectivity as a function of the incident angle. This table is then referred to when necessary in our calculations.
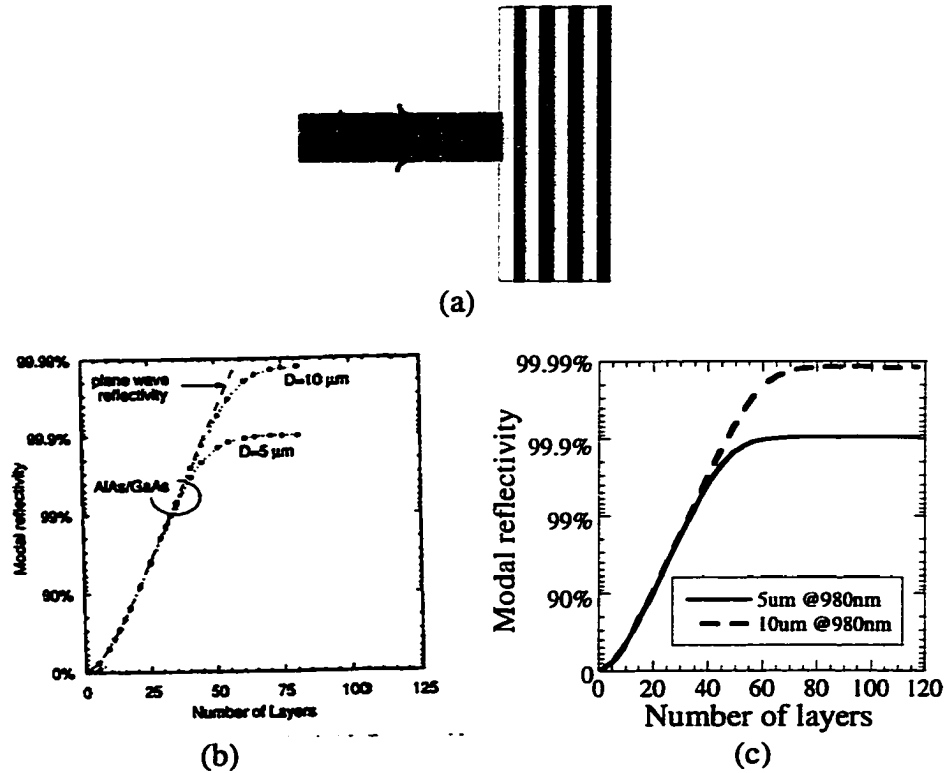
136

(a)

(b)

(c)

Figure 6.4 DBR modal reflection analysis
a) Schematic for a TEM_{00} mode that emerges from an air-clad GaAs waveguide reflecting off an AlAs/GaAs DBR. b) Figure 6 in reference [3]; c) Our results using equation (6.15) below to convert our 1D calculation into comparable 2D results.

As expected, the modal reflectivity of the TEM_{00} mode initially increases when layers are added to the DBR structure. However, after a certain number of layers, κ actually saturates no matter how many more layers get piled onto the DBR structure! It turns out that the additional layers do not contribute much to the peak reflectivity of the DBR, i.e. r_{norm} in (6.8), because it approaches unity asymptotically. However, the additional thickness of the DBR structure causes the non-normal incident plane wave components of the incident TEM_{00} mode to diffract away. Upon reflection, these non-normal incident plane wave components do not reconstitute a reflected mode holding an increasing semblance of the incident mode as more layers get piled onto the DBR.

Another important point to make from figure 6.4(b) is that the TEM_{00} mode emerging from a larger waveguide sees a κ that saturates at a higher reflectivity level

137

than a smaller mode. This is attributed to the fact that a larger spatial mode has a smaller divergence angle, which allows it to experience less diffraction loss through thicker DBR structures.

Our own calculation results are shown in figure 6.4(c). It should be noted that our results were calculated using one-dimensional TE_0 and TM_0 modes of air-clad GaAs waveguides with 5μm and 10μm widths. It took a little ingenuity to convert our 1D-κ's into the 2D-κ reported in [3]. And since this conversion is not obvious, we will digress slightly and take the following section to explain this.

From the definition of κ in (6.5), it is tempting to state that the two-dimensional κ, i.e. $\kappa_{TEM_{00}}$, is simply the product of the two one-dimensional κ's:

$$\kappa_{TEM_{00}} = \kappa_{TE_0} \kappa_{TM_0}.$$ (6.11)

Equation (6.11) seems deceptively straightforward. Upon closer examination of (6.8) however, we realize that it is not quite so simple. If we rewrite the one- and two-dimensional modal reflectivities in the manner of (6.8), i.e. under the paraxial limit, we would have the following:

$$\kappa_{1D} = r_{norm}e^{ikz}\gamma_{inc,1D}$$
$$\kappa_{2D} = r_{norm}e^{ikz}\gamma_{inc,2D}$$ (6.12)

It is important to note that the normal incident DBR reflectivity is the same regardless of the dimensionality of the plane wave in question. In the definition of coupling loss in (6.10), only the amplitude of κ matters; we thus can safely discard the complex phase term in (6.12) in future discussions.

The main difference between the two κ's in (6.12) lies in the γ terms on the right hand side. Once we figure out the relationship between γ_{1D} and γ_{2D}, we would be

138

able to relate κ_{1D} and κ_{2D}. It is thus our present goal to seek the relationship between γ_{1D} and γ_{2D}.

The simplest optical mode for which analytical answers for γ_{1D} and γ_{2D} can be sought is a Gaussian beam $f(r) \sim e^{-\frac{r^2}{w^2}}$, w being the half width of the beam waist. It is also handy that the angular spectrum of Gaussian beams is well understood. Plugging the one dimensional Fourier transform of the Gaussian f(r) into (6.9) and carrying out the integral gives us the following for the one-dimensional γ of a Gaussian:

$$\gamma_{1D-Gaussian} = \frac{1}{\sqrt{1+i\dfrac{1}{4\pi N}}}. \qquad (6.13a)$$

Here N is the Fresnel number characterizing scalable modes, $N = nw^2/(\lambda z)$, where n is the refractive index of the incident medium, w the half Gaussian beam waist, λ the wavelength in free space and z the roundtrip distance penetrated into the DBR structure. An otherwise similar but two-dimensional Fourier transform of f(r), a 2D Gaussian, gives us:

$$\gamma_{2D-Gaussian} = \frac{1}{1+i\dfrac{1}{4\pi N}}. \qquad (6.13b)$$

We can see that $\gamma_{2D-Gaussian}$ is simply the product of two $\gamma_{1D-Gaussian}$'s. This answer is not surprising in itself. Any radially symmetric field can be converted from the variable r^2 into x^2+y^2. The integral in (6.9) can then be broken down into two independent integrals or solved through substitution of variables as in the case of the 1D- and 2D-Gaussians.

Having thus established the relationship between the 1D- and 2D-γ's for radially symmetric modes, we can find κ_{2D} in terms of κ_{1D} using (6.12). From (6.12) and (6.13), we see that:

$$\kappa_{TEM} = \kappa_{2D} = r_{norm}e^{ikz}(\gamma_{1D})^2 \approx r_{norm}e^{ikz}\gamma_{1D,TE}\gamma_{1D,TM}$$

$$= r_{norm}e^{ikz}\left(\frac{\kappa_{1D,TE}}{r_{norm}e^{ikz}}\right)\left(\frac{\kappa_{1D,TM}}{r_{norm}e^{ikz}}\right) = \frac{(\kappa_{1D,TE})(\kappa_{1D,TM})}{r_{norm}e^{ikz}}; \qquad (6.14)$$

so that

$$|\kappa_{2D}|^2 = \frac{|\kappa_{1D,TE}\kappa_{1D,TM}|^2}{|r_{norm}|^2}. \qquad (6.15)$$

We argue that the approximation taken on the right hand side in the first line of (6.14) is valid because the beam is paraxial so that γ_{1D} is the geometric mean of γ_{TE} and γ_{TM}. Comparing figure 6.4(c) to figure 6.4(b), the results agree very well and we are confident that our approximations have been reasonable.

B Modal reflectivity (κ) of DBRs at detuned wavelengths

Now that we have a reliable method to find the modal reflectivity for the TEM$_{00}$ mode impinging on any arbitrary DBR structure, we can use this method to our advantage to figure out the penalties involved should there be any "mishaps". For example, what if the emission wavelength is *not* at the design wavelength of the DBR?[2] Does the modal reflectivity for the same TEM$_{00}$ beam degrade much if the DBR is grown slightly off? In addition, our little modal reflection calculator here can help us find the "perfect" DBR for a VCSEL. This latter point will be discussed in the

---

[2] This circumstance happens more frequently than not actually, at least in my experience as a graduate student!

140

next section. Meanwhile, we will concentrate on solving the first question in this section. How much does the modal reflectivity of a DBR degrade if the wavelength of the beam deviates from the DBR's center wavelength?

More often than not, the emission wavelength of a VCSEL is shifted from the design wavelength of the mirrors. Intuitively we expect that the modal reflectivity of such a mirror would be lowered due to the non-optimal condition. The only question is how much lower. Shown in figure 6.5 below is the same set of curves as those in figure 6.4(c), the modal reflectivity of the monochromatic TEM_{00} beam at the center wavelength of the AlAs/GaAs DBR. Additional in figure 6.5 are other sets of coupling loss curves for the same TEM_{00} mode but at a wavelength offset from the center wavelength of the DBR ($\Delta\lambda$ = 10nm, 20nm and 30nm).
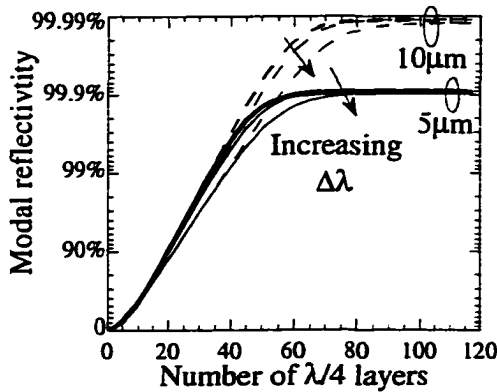

Figure 6.5 Modal reflectivity of an AlAs/GaAs DBR for the TEM_{00} mode emerging from a 5μm and 10μm wide waveguide
Modal reflectivity for a TEM_{00} mode plotted against the number of layers in the DBR as the wavelength of the mode varies ($\Delta\lambda$ = 10nm, 20nm, 30nm). The solid lines indicate κ for a 5μm wide waveguide and the dashed lines represent κ for a 10μm wide waveguide. Both incident and exit media are GaAs.

We can see that κ does not significantly decrease as the wavelength deviates from the design wavelength of the DBR, as long as enough layers are piled onto the structure. This exercise also serves to give us the insight that in the design of our tunable structure, enough layers should be piled into both the top and bottom DBR's

141

to compensate for their lowered modal reflectivities from the wavelength deviation caused by intentional wavelength-detuning. While this conclusion can be drawn simply from the consideration of the normal incident plane wave reflectance of the DBRs alone, we now have a more precise idea of how κ varies across the tuning range of our VCSELs for any given mode.

C κ of DBRs with different contrast values (Δn)

In our previous discussion in chapter 2, it was briefly mentioned that the larger the contrast in the refractive indices of layers that make up the DBR, the fewer layers necessary to reach a target peak reflectivity. If the mirror contrast is large, the penetration depth into such a DBR would be short and consequently the effective cavity length would be short compared to that with DBR's made of smaller mirror contrasts. In fact, many groups [6],[7] have demonstrated ultra low threshold micro-cavity VCSELs using dielectric mirrors. Again, with this DBR modal reflection tool that we have developed, we can examine the modal reflectivity of DBRs consisting of different dielectric mirror contrasts. Shown in figure 6.6 is, once again, the coupling loss of our TEM_{00} beam as a function of layers in the DBR. The monochromatic beam is at the center wavelength of the DBR, but DBR structures with different mirror contrasts (Δn) are considered.
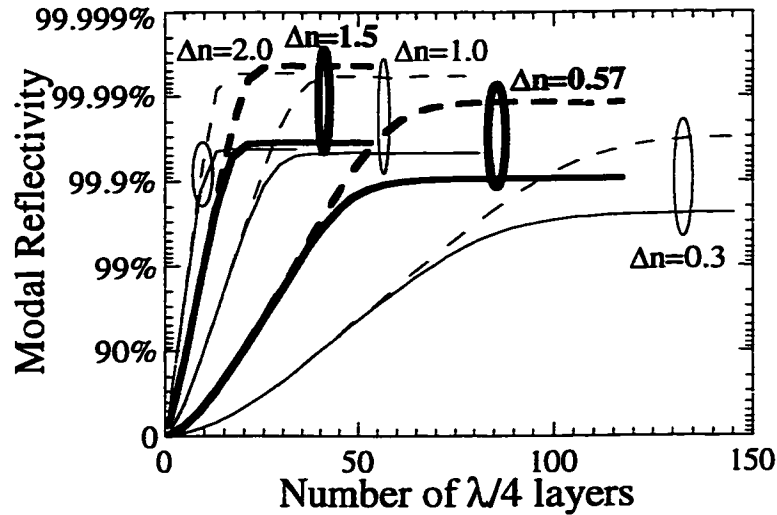
Figure 6.6 Modal reflectivity of DBR structures for 5μm and 10μm TEM$_{00}$ modes
Here κ is plotted as a function of the number of layers in the DBR. Dashed lines indicate κ for the 10μm TEM$_{00}$ mode and solid lines show that for the 5μm TEM$_{00}$ mode. Data with increasing Δn values are displayed in alternating thin and thick lines for ease of identification. As a reference, Δn=0.57 for GaAs/AlAs at 980nm. The higher index material in the DBR for these calculations is always GaAs (n~3.52 at 980nm).

As expected, an increase in Δn implies that fewer layers are necessary to reach saturation level for κ. Additionally, we would have expected that as Δn increases, the saturated modal reflectivity (κ) level would increase monotonically. This latter trend holds for Δn up to about 1.5, beyond which we can see that the saturated κ level starts to decrease as Δn increases. This result can be puzzling at first. We can begin to understand why this is so once we take a look at the angular reflectivity of these DBRs, shown in figure 6.7(a) below, to compare with the one-dimensional TE$_0$ or TM$_0$ spectrum of a 5μm mode, which is shown in figure 6.7(b).

143

(a)

(b)
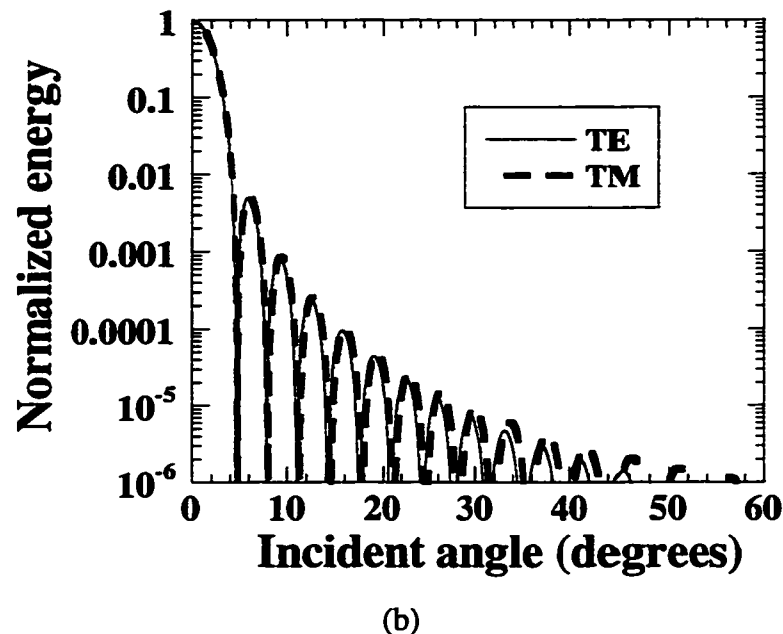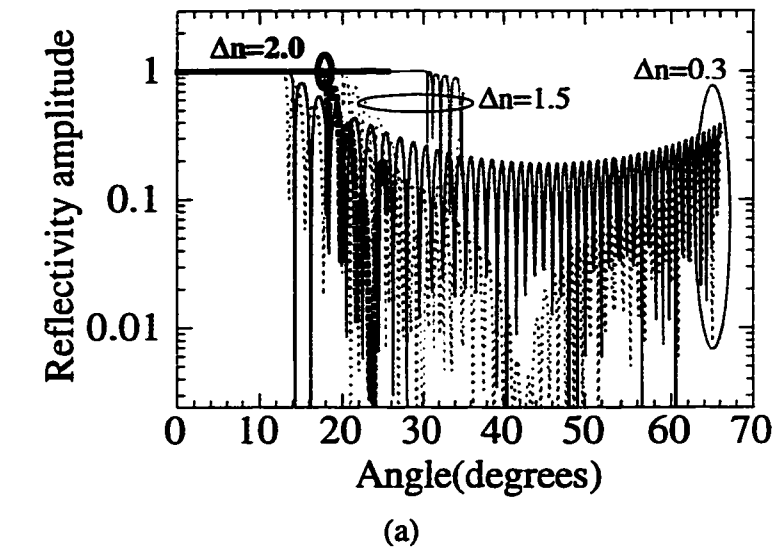
Figure 6.7 Explanation for the decrease of the saturated level of κ as Δn increases beyond 1.5

(a) Reflectivity of DBRs with Δn = 0.3, 1.5 and 2.0 as a function of incident angle of TE and TM polarized plane waves. Dashed line represent TM polarization and solid lines show the reflection coefficient for TE polarization. For clarity, the case for Δn = 2.0 is shown in the thick solid line. (b) Shown here is the angular spectrum of a 5μm wide TE_0 and TM_0 beam.

In figure 6.7(a), the reflectivity of the DBR is shown for incident angles from

normal incidence up until the angle at which total internal reflection (TIR) occurs,

dictated by Snell's law:

$$\theta_{TIR} = \sin^{-1}\left(\frac{n_{low}}{n_{high}}\right) = \sin^{-1}\left(1 - \frac{\Delta n}{n_{high}}\right). \qquad (6.16)$$

Since plane waves that are incident upon the DBR stack beyond θ_{TIR} do not contribute to any useful optical output of the cavity[3], they are not considered when we calculate the modal reflectivity of the DBR. From equation (6.16), an increasing Δn reduces θ_{TIR}, and more of the TEM$_{00}$ spectrum is not usefully reflected back. Thus for any given optical mode, the modal reflection would saturate at a maximum level for an optimal Δn, which we call Δn_{opt} here. Increasing Δn beyond Δn_{opt} would lower the maximum achievable modal reflectivity due to the filtered spectrum of the incident mode. In our case Δn_{opt} happens to be 1.5, and TIR occurs at 35°. From figure 6.7(b), the energy spectrum of the 5μm TEM$_{00}$ mode at 35° is more than five orders of magnitude below the normal incident plane wave. This example illustrates how sensitive κ is to the presence of oblique angular components in any given optical mode.

In many ways, this is an important discovery. Contrary to popular beliefs (that includes only normal incident considerations) in our field, a micro-cavity laser using large Δn mirror stacks (like semiconductor-air layers) may not be conducive to supporting the lowest order mode in both the transverse and longitudinal directions. It is equally important to note that θ_{TIR} is a function of both Δn and n_{high}. While Δn has to be high enough to achieve a wide stopband, $\Delta n/n_{high}$ should be low enough that θ_{TIR} in (6.16) is as close to 90° as possible to preserve the spectrum of the incident mode. Of course these two requirements are always at odds with each other. A compromise

---

[3] TIR rays simply cannot escape the cavity!

has to be reached between the desired mode profile and a practical DBR that supports it.

III   Iterative method for finding diffraction loss

After having established an accurate model for the reflection of optical modes from DBRs, we can incorporate this model into the overall framework with which we will answer the major questions outlined at the beginning of this chapter, the first of which we will discuss immediately. Our objective is to assess the "penalty" paid to obtain wavelength tunability in our VCSEL.

A   Formalism

We first have to find the extra loss (per round trip) the lowest order mode in our tunable structure sees beyond that which a similar mode suffers in the regular VCSEL. Our goal in this section, then, is to compare the optical losses for a particular mode in a tunable VCSEL to those of a regular VCSEL. To render a fair comparison, mirrors with similar peak plane wave reflectance are used. Figure 6.8 below shows the two VCSEL structures to be compared. The rest of this sub-section is devoted to establishing the general building blocks we need to evaluate the loss for any VCSEL structure.
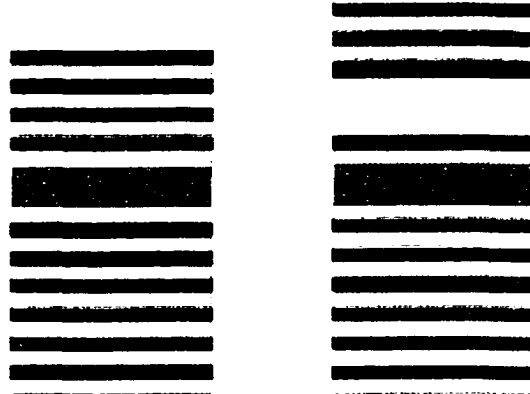
146

Figure 6.8 Schematic showing two VCSEL structures to be compared
On the left is a regular VCSEL while on the right is an equivalent tunable VCSEL with an air gap. The mirror reflection coefficients have been adjusted to be equal in both structures.
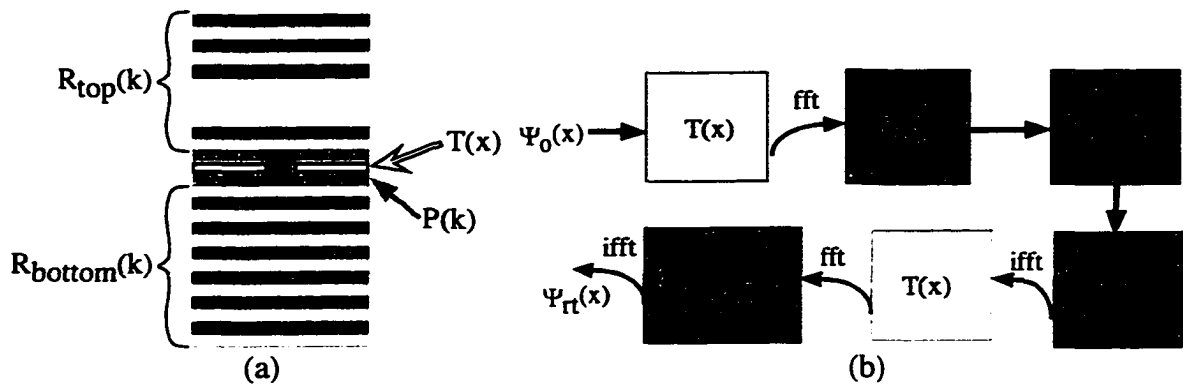

Figure 6.9 Steps taken in one roundtrip around a VCSEL cavity
a) Schematic of the (tunable) VCSEL and b) a flow chart of the optical processes seen by the optical mode $\psi(x)$ as it traverses one round trip around the cavity. The light gray boxes are optical processes handled in real space. The darker boxes are those handled in k-space. Transition from one kind of boxes to the other requires a fast Fourier transform (fft) or an inverse fft (ifft).

First, the lowest order eigenmode in each structure has to be determined. Shown in figure 6.9(a) above is the schematic of our VCSEL with several optical processes labeled separately. The FP-wavelength of the entire structure is determined first. For both the top and bottom DBRs, the complex reflectance as a function of incident angles is calculated, as in the example shown in figure 6.2. Propagation through the spacer region is denoted with P(k). This is the same process as in (6.4). The complex phase undergone by each plane wave component is taken due account. Lastly, T(x) represents the gain "aperturing" in our VCSEL for mode definition in the

147

transverse direction. As gain is a physically spatial process, we shall handle it in real space. Through this gain aperture function T(x) we set boundary conditions for the optical mode. Every time the spatial mode $\psi(x)$ passes through T(x), $\psi(x)$ would be modified according to T(x). In the simplest case, T(x) is a top hat transmission function:

$$T(x) = \begin{cases} 1, |x| \le \dfrac{a}{2} \\ 0, |x| > \dfrac{a}{2} \end{cases} ; \qquad (6.17)$$

where a is the aperture size. The accompanying flow chart with these functions as individual blocks is shown in figure 6.9(b).

Our method is very similar to that undertaken in [8]. A mode $\psi_0(x)$ is first initialized[4] and sent around the cavity through the different blocks in figure 6.9(b). As it passes through the gain aperture T(x), its spatial profile is modified. A simple fast Fourier transform (fft) of $\psi(x)$ gives its spectrum, which would be duly modified by propagation through the spacer as well as reflection off both mirrors. An inverse fast Fourier transform (ifft) converts the mode back into its spatial distribution before its shape is reinforced by T(x) again. After one such roundtrip the resultant mode, $\psi_{rt}(x)$, is compared with the initial mode $\psi_0(x)$. Unless $\psi_0(x)$ is the eigenmode of the VCSEL cavity as defined by the characteristics of the two mirrors, the spacer region, and the aperture function, $\psi_{rt}(x)$ would be different from $\psi_0(x)$[5]. The overlap integral between

---

[4] It doesn't matter what the initial mode looks like. The lowest order eigenstate would be reached eventually through enough iterations/roundtrips. This is not surprising because nature works the same way!

[5] If $\psi_0(x)$ were an eigenmode of the cavity, then $\psi_{rt}(x)$ and $\psi_0(x)$ would only be off by a complex amplitude, which is the eigenvalue of the propagation constant that describes the entire roundtrip process.

148

the two is found using equation (6.5a) to obtain the appropriate modal reflectivity κ_i, where i denotes the i-th roundtrip. κ_i is then compared to κ_{i-1}. If κ_i has converged, it is the eigenvalue for the roundtrip propagation constant of the eigenmode in the cavity, $\psi_0(x)$. If κ_i has not converged, then $\psi_n(x)$ is first normalized and bounced around the cavity again just as $\psi_0(x)$ in the previous roundtrip. This process continues until convergence of the propagation constant occurs.

B   Loss comparison between tunable and regular VCSELs

With all of the major building blocks in place, we can now consider the first question posed at the beginning of this chapter: What is the cost for tunability in the tunable VCSEL structure? Referring to figure 6.8 from the previous section, the two VCSEL structures whose κ are compared are our existing tunable VCSEL and a regular VCSEL. Again, reflectance in the mirrors is similar for the two structures. Since κ is nominally very close to unity, we shall compare the coupling loss, defined as $1-|\kappa|^2$, hereafter in our discussion for clarity.

Figure 6.10 below shows the results of our calculations for the two structures, where the coupling loss is plotted in log scale against the aperture size, also in log scale. The solid line is the result for the regular VCSEL structure. The dashed lines are results for the tunable structure, with three different air gap sizes. The thicker the air gap, the more coupling loss $\psi(x)$ suffers. Because of the one-third limit for the tunable cantilever, the realistic working regime is the dashed curve showing the most loss (air gap = $5\lambda/4$.) Thus, the difference between this uppermost loss curve and the solid line is the extra loss our tunable device sees. Using T(x) as indicated in (6.17), a $5\mu m$ device with an opaque aperture sees 40% extra loss over that in a regular

VCSEL. Needless to say, this penalty is quite significant. A consolation is that this air gap penalty decreases fairly quickly as the aperture size of the device increases. As seen in figure 6.10 below for a 10μm aperture, the mode in the tunable structure sees only marginally more loss than that of a regular VCSEL (~11%).
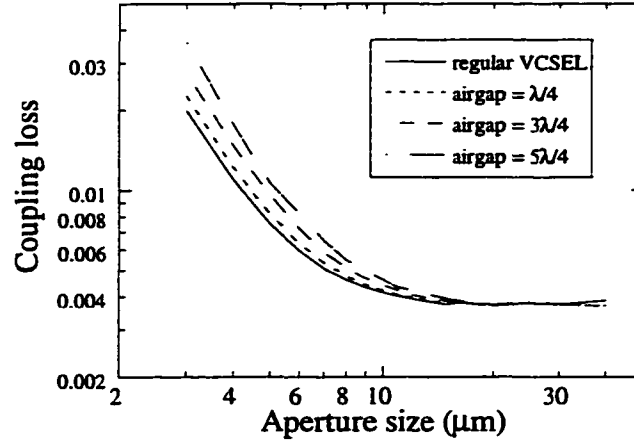

Figure 6.10 Optical loss due to the presence of an air gap: opaque aperture
Coupling loss is defined as $1-|t|^2$. Shown here is the case for an opaque aperture with a top hat transmission function shown in equation (6.17).

The form of T(x) used in (6.17) is only the simplest of approximations. In our devices, however, the physical definition of the transverse dimension in our VCSEL does not render our aperture opaque at all. As discussed in chapter 3, the transverse dimension in our devices is defined through phase (rather than amplitude) apertures by the conversion of an AlAs layer in the structure into aluminum oxide (Al_xO_y). Therefore in this approximation, T(x) assumes the following form:

$$T(x) = \begin{cases} e^{i\phi_{AlAs}}, |x| \le \dfrac{a}{2} \\ te^{i\phi_{Al_xO_y}}, |x| > \dfrac{a}{2} \end{cases} ; \tag{6.18}$$

where ϕ_{AlAs} and $\phi_{Al_xO_y}$ represent the phase accumulated by the optical mode in traversing through the thickness of the AlAs and Al_xO_y layers, respectively, and t is

150

the transmission coefficient of the incident beam from the AlGaAs spacer layer into the oxide layer:

$$t = \sqrt{1 - \left(\frac{n_{AlGaAs} - n_{ox}}{n_{AlGaAs} + n_{ox}} \right)^2} .$$
(6.19)

Following the same scheme outlined in the previous section using an opaque aperture, we arrive at the structures' roundtrip loss again, but with phase apertures this time. The results are shown in figure 6.11 below.
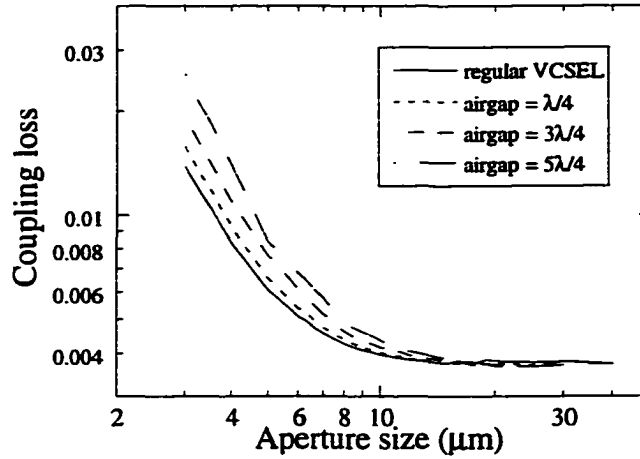

Figure 6.11 Optical loss due to the presence of an air gap: phase aperture
Coupling loss is defined as $1-|t|^2$. Shown here is the case for a phase aperture as shown in equation (6.18). The thickness of the AlAs/Al$_x$O$_y$ layer is 300Å.

In this case, the optical coupling loss is slightly lower than comparable structures with opaque apertures shown in figure 6.10. The penalty of having an air gap in this case is smaller: For a device 5µm in diameter, the roundtrip loss due to the air gap is only about 20% higher than that in a regular VCSEL. As the device increases in size to 10µm in diameter, the air gap causes only about 7% additional loss to that already present in the regular VCSEL structure.

The first trend we see from both figures 6.10 and 6.11 is that the penalty for tunability is quite steep at small device sizes. As the aperture size decreases, the

151

spectral content of the high frequency components for the mode increases. The TIR

condition imposed by the large change in the index of refraction at the air-

semiconductor interface (θ_{TIR} ~18°) is not particularly forgiving in propagating these

high frequency components. (For comparison's sake, θ_{TIR} for an AlAs/GaAs interface

is 56.7° whereas for a GaAs-air interface θ_{TIR} is only about 16.1°.) Consequently,

modes emerging from small apertures experience dramatically high losses.

An additional necessary comment here concerns the extra coupling loss for an

opaque aperture compared to that associated with an oxide aperture. This is attributed

to the high frequency components in $\psi(x)$ introduced through the abrupt amplitude

aperture in (6.17). A phase aperture such as (6.18), in contrast, introduces more

gradual changes to $\psi(x)$. A 300Å thick AlAs/Al$_x$O$_y$ layer causes only about 16° of

phase shift per pass between the oxidized perimeter and the unoxidized AlAs center of

the device. In addition, the transmission coefficient t in (6.19) is on the order of 94%

per pass. Neither the amplitude nor the phase change of the mode through T(x) is

abrupt enough to cause the generation of substantial amounts of high frequency

components that would get filtered out by the air-semiconductor interface in the

structure. Simply put, a phase aperture such as T(x) in (6.18) provides significantly

stronger index guiding to the propagating mode than an abrupt aperture such as T(x) in

(6.17). The difference in the wave-guiding property between the two types of

apertures shows up more dramatically at small device sizes for the same reasons cited

in the discussion above. Only now devices with small *opaque* apertures are further

exasperated by the TIR filtering at the semiconductor-air interface. Realistically

speaking, T(x) in our tunable VCSELs is a combination of both (6.17) and (6.18).

152

While the transverse modes are defined through a lateral oxide aperture like that in (6.18), the injected current profile gives us a spatially limited gain profile resembling (6.17).[6] Therefore, it is safe to state that T(x) in (6.17) gives the upper limit of the optical loss in our VCSELs. It is also instructive to use the simplest aperture possible to calculate the other losses in the tunable structure.

C   A few words on the limits of this model

So far, our methodology has been discussed without any mention of the approximations involved. It is important that we mention the validity of our model so that its limitations as well as its domain of validity are understood.

Due to the linearity and superposition properties of Maxwell's equation, the propagation of wavefronts and their reflection from DBR structures are completely represented through our mathematical manipulations in k-space. Our method is identical to those in [8], considered one of the seminal papers in the field of maser/laser cavities. The only addition to our model is the thin intracavity aperture. Diffraction of the internal wavefronts from this aperture represents the only approximation in our model. Other authors have used similar models to deduce scaling laws of gain-guided VCSELs [9] and scattering losses in oxide-apertured VCSELs [10], [11].

It is thus extremely important for us to realize the implicit limitation underlying our model. Diffraction of wavefronts from these apertures introduces evanescent waves not readily accounted for in the components described in figure 6.9(b). However, we can put forward an argument in favor of our approach in

---

[6] The gain profile in our VCSELs is *definitely not* a top hat function, however.

153

neglecting these evanescent waves in the model: These evanescent waves would suffer so much loss in a cavity that requires high Q's[7] that they do not contribute significantly towards the optical output anyway. Furthermore, propagating waves with incident angles greater than θ_{TIR} do not contribute to the useful, observable output of the VCSEL. Therefore, our calculated modal loss gives a good estimate to compare against our observed data.

D   Coupling loss across tuning range

Having assessed the extra optical loss caused by having an air gap inside the structure, the next question we would like answered is how this optical loss behaves across the tunable spectrum. The answer to this question will help us understand the laser's performance characteristics across its tuning range. This understanding is crucial for further improvement in engineering a better design of the tunable VCSEL.

Since the reflectivity of the two DBRs is not constant over the entire tuning range, the coupling loss defined in (6.10) is now consisted of two components: One is the modal propagation loss through the adjustable air gap while the other is the loss associated with the normal incident plane wave as this plane wave changes in wavelength. Both of these vary as the air gap thickness changes. Referring to (6.12), modal reflectivity loss across the wavelength spectrum for each mirror can be re-written as:

$$\kappa(\lambda) = e^{i\left(\frac{2\pi}{n\lambda}\right)z} r_{norm}(\lambda)\gamma(\lambda). \tag{6.20}$$

---

[7] Typical vertical cavities require Q>300.

154

Here, $\gamma(\lambda)$ is the figure we are after: It is simply the ratio of κ and r_{norm}. Since the roundtrip $\gamma(\lambda)$ is close to unity, we will plot $1-|\gamma(\lambda)|^2$ in figure 6.12 below. This expression is:

$$1-|\gamma(\lambda)|^2 = 1-\left|\frac{\kappa(\lambda)}{r_{norm}(\lambda)}\right|^2 = \frac{|r_{norm}(\lambda)|^2 - |\kappa(\lambda)|^2}{|r_{norm}(\lambda)|^2}. \qquad (6.21)$$

For $|r_{norm}(\lambda)|^2$ close to unity, the denominator in (6.21) can be assumed to be 1. Rearranging the terms of (6.21) we arrive at the following:

$$\alpha_{diffraction}(\lambda) \equiv 1-|\kappa(\lambda)|^2 \approx |r_{norm}(\lambda)|^2 - |\kappa(\lambda)|^2. \qquad (6.22)$$

Thus, for $|r_{norm}|^2$ close to unity (>0.99), the roundtrip coupling loss of the eigenmode can be simply approximated as the difference between the normal incident plane wave reflectivity of mirrors and the roundtrip modal reflectivity. Note that r_{norm} here is the product of the reflection coefficients of both the top and bottom DBRs in the VCSEL.
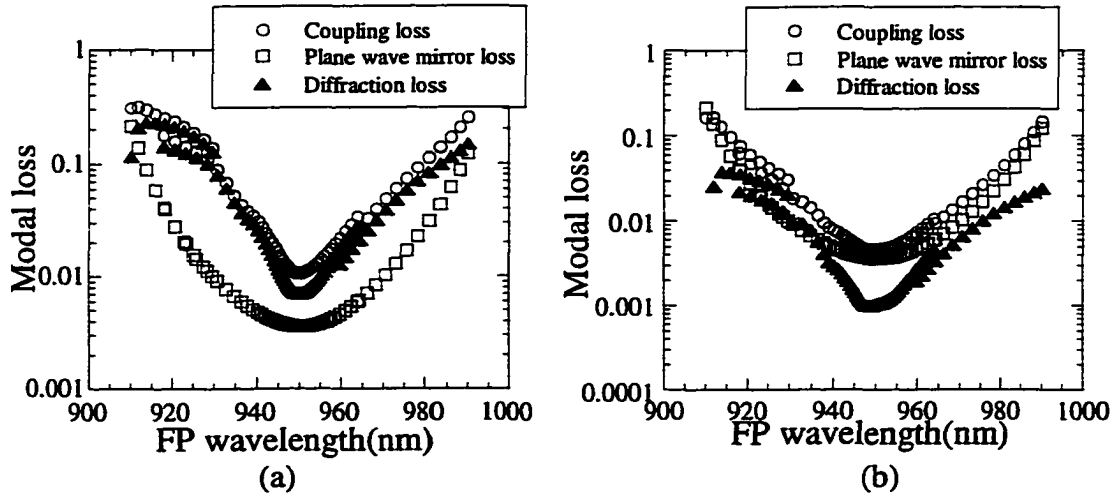

Figure 6.12 Modal loss across tuning spectrum: opaque aperture
Shown in (a) is the loss for a 5μm device, and in (b) is the loss for a 10μm device. Coupling loss, $1-|\kappa|^2$ in equation (6.10), is shown as open circles. The plane wave mirror loss, the $|r_{norm}|^2$ term in equation (6.22), is shown in open squares. The difference between the two is the eigenmode's diffraction loss through the tunable VCSEL, the $1-|\gamma|^2$ term in equation (6.21). This is shown in solid triangles.

155

Shown in figure 6.12 above is the calculated roundtrip optical loss across the tunable VCSEL's spectrum for two opaque apertures 5μm and 10μm in diameter. T(x) assumes the form in (6.17). The open circles represent $\alpha_{coupling}$ calculated with (6.10), while the open squares are $|r_{norm}(\lambda)|^2$. Diffraction loss through the air gap can be extracted using either (6.21) or (6.22) and is shown as solid triangles in figure 6.12. A dramatic difference between the two cases is observed for the diffraction loss. Optical loss in the 5μm device is dominated by this diffraction loss through the air gap, while in the 10μm device it is dominated by the non-unity plane wave mirror loss. For the smaller device, diffraction loss easily constitutes more than half (66%-93%) of the coupling loss. In contrast, diffraction loss for the larger sized device constitutes only 21%-70% of the total optical loss, the 70% accounts for diffraction loss at the edges of the tuning spectrum.

It is instructive to repeat the same calculations for a phase aperture such described in (6.18). The results are shown in figure 6.13 below. Again due to the better wave-guiding property of the phase aperture, coupling loss is smaller in this case than that with an opaque aperture. Since the plane wave mirror loss is independent of the kind of apertures used, the subsequent diffraction loss for a VCSEL with a phase aperture always constitutes a smaller fraction of the total loss than for an opaque aperture. Nevertheless, the difference between the two sizes follows the same trend in figure 6.12. Diffraction loss in the 5μm aperture devices make up 56%-85% of the total loss and only 19%-44% in the 10μm aperture devices.
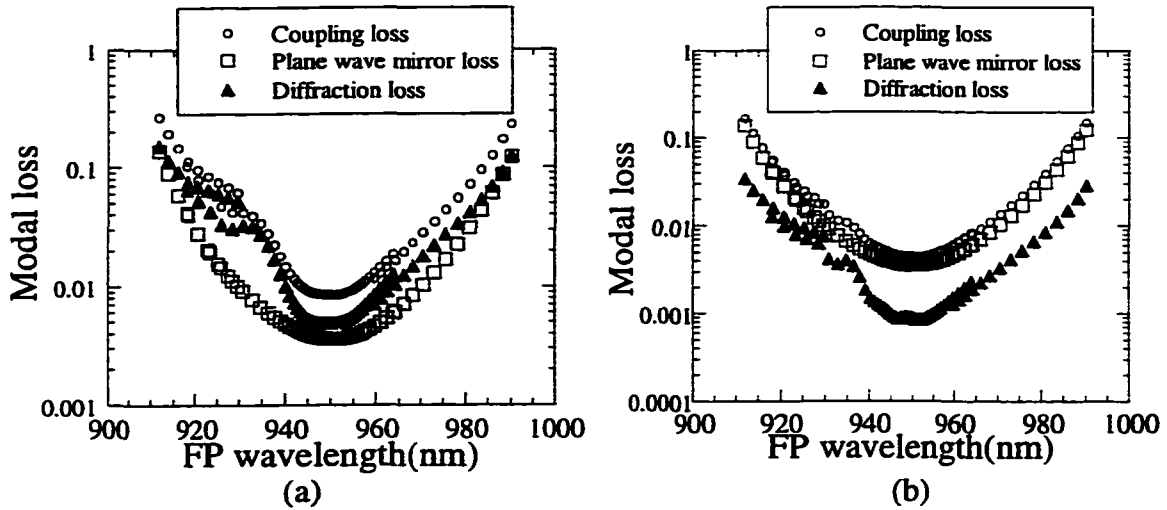
156

Figure 6.13 Modal loss across tuning spectrum: phase aperture
(a) 5μm diameter and (b) 10μm diameter: The symbols are the same as in figure 6.12. For the 5μm wide oxide aperture, diffraction loss still dominates, although to a smaller extent than the case depicted in figure 6.12(a). At 10μm, the non-unity reflectivity of the DBRs dominates the total loss.

We have thus answered the second question posed earlier and have established that regardless of the aperture model used, the diffraction loss due to the air gap in the tunable structure dominates for device sizes ≤5μm in diameter. The good news is that as the device size is increased to 10μm, optical loss due to the non-unity reflectivity of the two DBRs actually dominates the optical loss process.

IV   Tilt loss

Finally, the last question to be put to rest is concerned with the optical loss from the tilt of our mechanical mirror. Since the top mirror acts like a springboard, a commonly asked question is whether the tilt of this mirror introduces enough loss to keep the laser from achieving a sufficiently large tuning range. In this section, we would like to place a figure on this loss.

A   Formalism

The methodology used in calculating for the tilt loss is very similar to that for the "diffraction" loss in the last section. As the models for the other parameters in the VCSEL structure are the same, coming up with a model for the tilt in the top DBR is the only remaining task for this section. Of course, the first issue at hand is to find the amount of tilt in this mirror. Using the electromechanical model discussed in chapter five, we can deduce the amount of tilt in the top mirror as the applied tuning voltage is increased. Because of the one-third limit, the maximum amount of displacement for the cantilever beam from its original position is the same regardless of the geometry of the arm. Thus, the longer we make the arm, the smaller this tilt angle would be. Shown in figure 6.14 below is the calculated amount of tilt at the end of our cantilever beams as a function of the tuning voltage for three beam lengths: 100μm, 150μm, and 200μm.
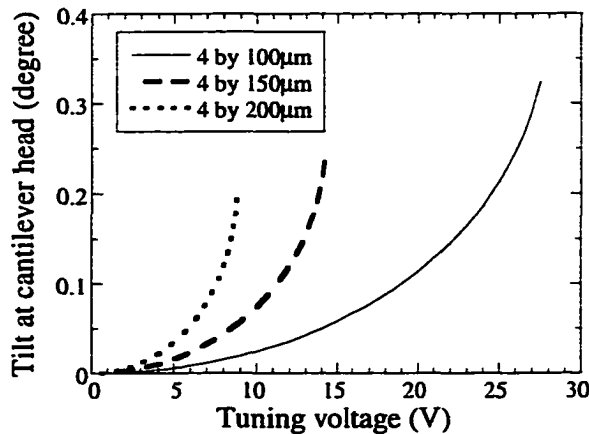

Figure 6.14 Tilt angle in the top mirror as a function of the tuning voltage
Because of the one-third rule, the shortest lever beams experience the largest amount of tilt. In our case, our shortest beams are 100μm long, which means that the maximum tilt in the top DBR is about 0.4°.

Since the shortest beams we have are 100μm long, these also experience the most tilt as they reach the tuning limit. From figure 6.14, we can see that the

158

maximum tilt angle is less than 0.4 degree! We shall use this figure to determine the

worst case estimate for tilt loss in our tunable structure.

Figure 6.15 Tunable VCSEL structure with a tilted top DBR
Other than the nonzero ϕ in the top mirror, this is exactly the same as the tunable structure in figure 6.8.

Figure 6.15 above shows the tunable VCSEL with a tilted top DBR. The

analytical steps taken for the optical processes seen by the optical mode in one

roundtrip around this cavity is completely analogous to that shown in figure 6.9(b),

with the exception that additional steps have to take into account for the tilt in the top

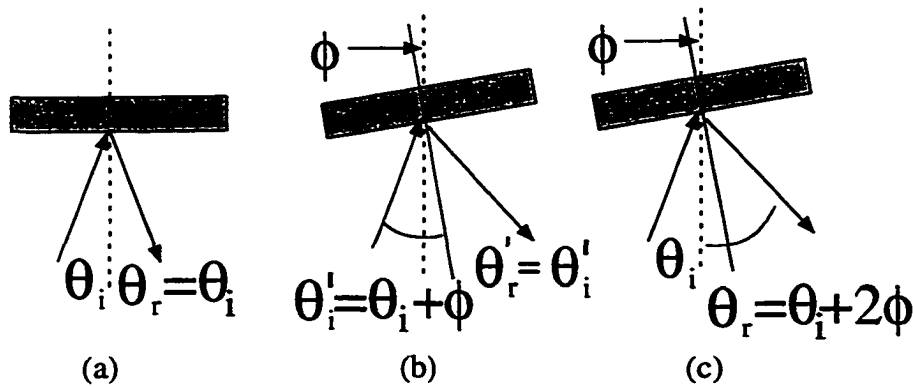mirror. We shall discuss these additional steps immediately.

(a) $\theta_i \quad \theta_r = \theta_i$

(b) $\theta_i' = \theta_i + \phi \quad \theta_r' = \theta_i'$

(c) $\theta_r = \theta_i + 2\phi$

Figure 6.16 Reference frames used to figure out how to handle plane wave reflection off a tilted mirror
Given a ray incident at θ_i (from a referenced set of axes denoted in the dashed vertical line), shown in (a) is the specular reflection off a mirror in this "rest" frame. When the frame axes are rotated with the mirror as in (b), where all the angles in this rotated frame are denoted with apostrophes, the same specularly reflected ray comes off the mirror at θ_r'. In (c), we relate the reflected angle from the rotated frame in (b) to the rest frame in (a).

159

Referring to figure 6.16 above, the tilt angle of the DBR contributes itself twice to the incident angle in the case of a specular reflection in the rest frame. See figure 6.16(a). If the tilt angle of the DBR was ϕ, a ray incident at angle θ in the "rest" frame would have its reflection at $\theta+2\phi$ away from the z-axis.

This exercise helps us establish the sequence of steps necessary to accurately account for the plane wave contributions of an internal optical mode upon its reflection from a tilted DBR. For each plane wave component, its incident angle θ relative to the z-axis is first determined. The tilt angle ϕ of the DBR is then added to θ to obtain the effective incident angle (with respect to the DBR). The appropriate complex reflectance of this plane wave from the DBR is found through a look-up table such as that plotted in figure 6.2. The complex amplitude of this plane wave is then properly reflected with the appropriate complex reflectance. Afterwards, the reflected angle of this plane wave is adjusted to be $\theta+2\phi$ for the proper accounting in k-space such that propagation, gain aperturing, and reflection off the other DBR in the cavity can be readily accomplished in the same manner outlined in the previous section.

B   Results

Since the shortest cantilever beam has the largest tilt angle and subsequently the largest tilt loss, we shall find the tilt loss for a 100μm long lever, the shortest of our devices, to give an upper estimate for tilt loss in our VCSEL structure. As before, we will calculate the tilt loss in two different tunable VCSELs with aperture sizes of 5μm and 10μm in diameter. In either case, the tilt loss is deduced from the difference in modal reflectivity of the eigenmodes for the two cases where one includes tilt in the

top mirror and the other does not, i.e. *tilt loss = κ without tilt − κ with tilt*. For a

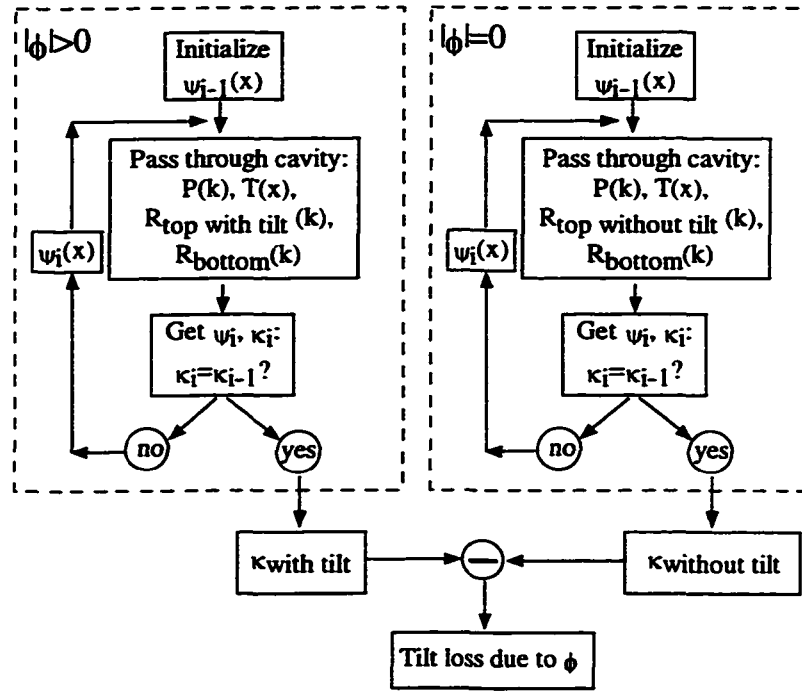detailed flow chart, the reader is referred to figure 6.17 below.

Figure 6.17 Flow chart detailing how tilt loss is determined
For both structures (one with a tilted top DBR and the other a parallel mirror), after
the lowest order eigenmode ($\psi(x)$) and its propagation constant (κ) are determined for
each, the difference between the κ's gives an estimate of the tilt loss.

The tilt loss for devices $5\mu m$ and $10\mu m$ in size is plotted in figure 6.18 below

as a function of the tilt angle in the top DBR. In the case of the smaller device, the

maximum tilt loss is approximately 0.1%, which is more than an order of magnitude

below the diffraction from the air gap (>1.1%) in figure 6.12(a) of section III D. In

contrast, the larger device suffers significantly more tilt loss (fractionally). The

maximum tilt loss is 0.6%, which is comparable to κ (>0.045%) from previous
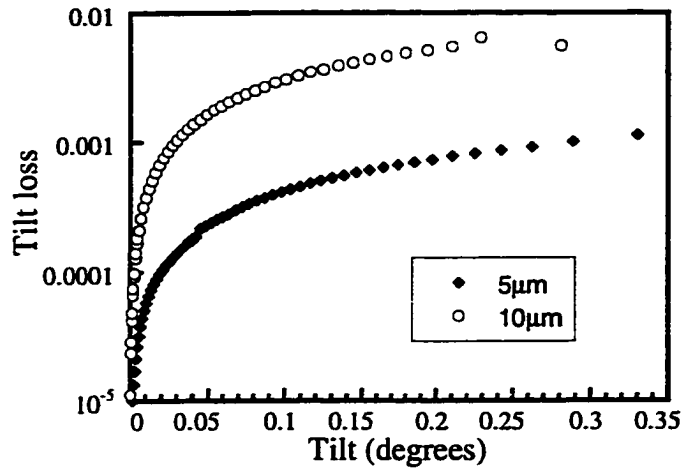
considerations in figure 6.12(b).

Figure 6.18 Tilt loss
For VCSELs with 5μm (solid diamonds) and 10μm (open circles) apertures

Since the tilt angle is the same for both device sizes, one might wonder why

the 10μm mode in figure 6.18 above sees more tilt loss. Refer to figure 6.19 below for
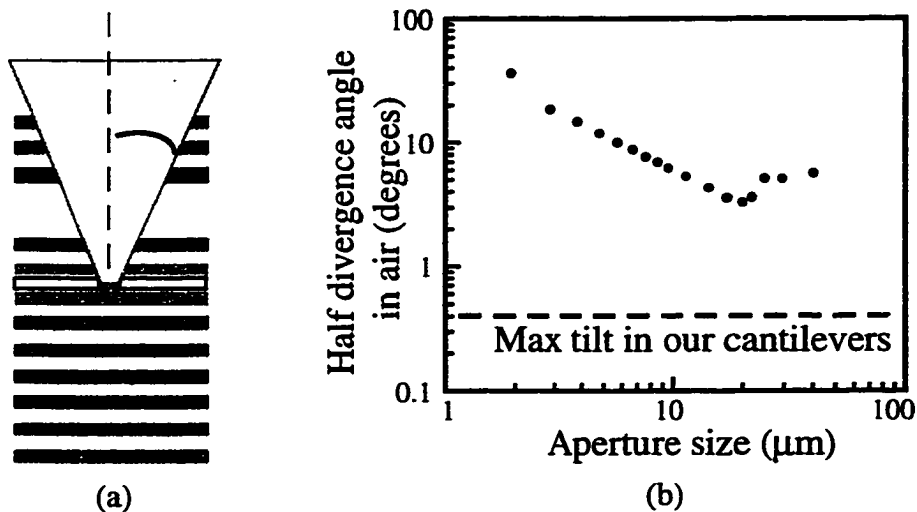
an explanation.

(a)   (b)

Figure 6.19 Divergence angle of different sized modes
Schematic of an optical mode emerging from a VCSEL is shown in (a). The half
divergence angle of the eigenmode is plotted in (b) as a function of aperture size.

Before we explain away the disparity in the tilt loss for the two device sizes,

some fundamental grounds should be covered first. An optical spatial mode can be

equivalently characterized by its mode profile in angular terms. Therefore, any band-

limited, scalable spatial profile can be described by its prescribed divergence angle.

162

Consequently, the lowest order eigenmode of a tunable VCSEL with increasing aperture size will have increasing full-width half-max spatial widths. In figure 6.19, the half divergence angle of each eigenmode is plotted against the width of the opaque aperture. As expected, the half divergence angle decreases as the aperture size increases.[8] As a reference point for comparison, a horizontal dashed line in figure 6.19(b) indicates the maximum possible amount of tilt present in the cantilever head. Since the smaller aperture device has a larger divergence angle, the maximum tilt of the mirror presents a smaller fraction of its divergence angle than that from a larger aperture device.

When reflected off a tilted DBR, every plane wave component of the mode experiences a shift in its angle or k-vector. Because of its broader angular spectrum, a small spatial mode readily accepts the newly shifted angular profile of the reflected mode. In other words, the smaller mode has a larger acceptance angle and is more tolerant of "stray" rays. Although this concept can be counter-intuitive at first, larger modes are actually easier to "walk off" because they resemble infinite plane waves. For an illustration demonstrating this graphically, the reader is referred to figure 6.20 below. This trend is also reflected in figure two of reference [8].

---

[8] The divergence angle bottoming out beyond $20\mu m$ is due to the calculation precision of the many Fourier and inverse Fourier transforms in our routine. Satellite peaks which are more than four orders of magnitude below the main lobe begin to contribute to the eigenmode's angular width, which is defined in figure 6.19(b) as: $\sigma_k = \sqrt{\langle\psi(k)\rangle^2 - \langle(\psi(k))^2\rangle}$.
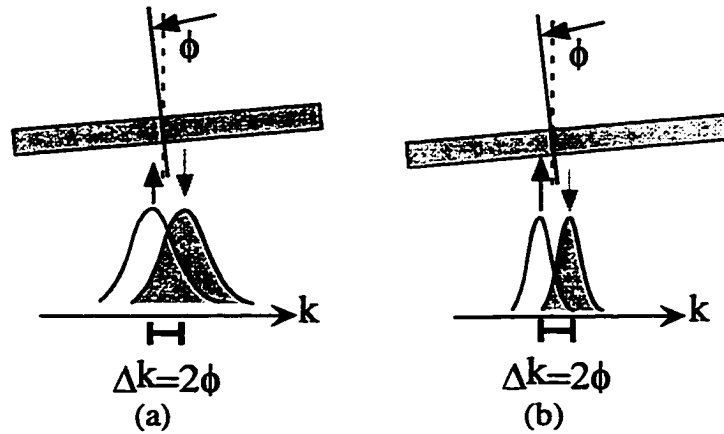
163

Figure 6.20 Larger spatial modes can walk-off more easily from a tilted mirror.
In (a), the incident spectrum of a small spatial mode (shown in black outline with an upward arrow to indicate propagation direction) and its reflection off a tilted mirror (shown with a gray background and a downward gray arrow) overlap significantly. For a larger spatial mode, the overlap is significantly smaller. This is shown in (b).

Having addressed the tilt loss question, we now can summarize our findings with the following conclusions. We have found that tilt loss affects larger devices more adversely. While tilt is not dominant in small tunable VCSELs, it can be comparable to optical losses (κ) already present in the tunable structure. There are ways to minimize this loss. First, the maximum tilt angle can be reduced by adjusting the length of the cantilever beam for a given aperture size. Second, if for some reason the cantilever arm cannot be lengthened (as in the case of a device comparable to 10μm in size), tilt loss can be made the dominant component in the total optical loss by increasing the DBRs' reflectivity so that the total loss is lessened. Lastly, we must live with the definite tradeoff between the tilt and diffraction losses for a given aperture size in a tunable VCSEL. While diffraction loss is the dominant component in a small tunable VCSEL, in a larger device one has to be concerned with this tilt loss. An overall minimized total optical loss requires a delicate balance between these two loss components.

C   Confirmation of our results

To ensure that our finding makes sense, it is compared against Fox and Li's paper on maser interferometers with tilted mirrors [8]. Shown in figure 6.21(b) below is a figure in their paper showing the additional power loss due to the tilt of the two mirrors of the maser resonator, whose configuration is shown in figure 6.21(b).
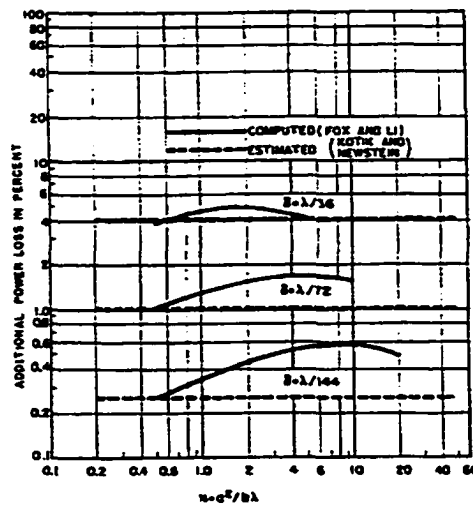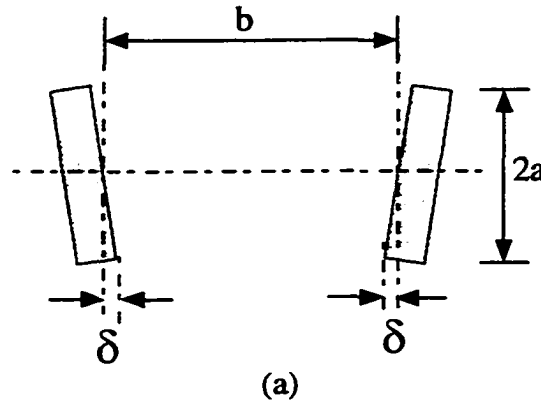

(a)

Fig. 3—Additional power loss per transit due to mirror tilt for the lowest-order TEM$_0$ mode—a comparison of our computed results with the estimated values of Kotik and Newstein.[1]

(b)

Figure 6.21 Results from Fox and Li's paper
(a) Configuration of maser resonator with tilted mirrors. The variables are labeled to ease conversion from the maser dimensions to Fresnel numbers. (b) Figure 3 in [8]. It shows the calculated power loss due to the tilt of the mirrors in the maser resonator.

The x-axis in figure 6.21(b) is in terms of the Fresnel number (N) of the resonator, which is defined by the radius of the mirrors a, the cavity length b, and

165

wavelength λ as $\dfrac{a^2}{b\lambda}$. Since the mirrors are distributed in our case, the length of the cavity can be estimated to be on the order of 3-4λ, a ~ 2.5λ for a 5μm device and 7.5λ for the other device with a 10μm aperture. Therefore, N~1.5 for the 5μm device and ~6 for the device with a 10μm aperture.

In order for us to compare our results against those in figure 6.21(b), we need to determine the applicable δ in our case. From figure 6.21(a), we can see that $\delta = a * \tan(\theta_{tilt})$, where θ_{tilt} is the tilt angle of each of the two mirrors. Comparing θ_{tilt} to the tilt angle applicable to our scenario in figure 6.15, one can see that θ_{tilt} is half of the tilt angle in our case because we have been enforcing tilt in only one mirror, resulting in an asymmetric cavity. Substituting the maximum tilt of 0.4 degree in figure 6.15 into the expression for δ above yields $\delta = \lambda/109$ for a = 2.5μm and $\delta = \lambda/54$ for a = 5μm. Following the $\delta = \lambda/144$ curve in figure 6.21(b) for the smaller device with N~1.5 gives us about 0.4% tilt loss (in power) while the larger device with an N~6 at an extrapolated curve of δ ~ $\lambda/54$ gives us a tilt loss of ~2.5%. In both cases, our estimated tilt loss is consistently smaller by factor of two from reference [8].[9]

This discrepancy is attributed to the difference in the construction of the resonators. While [8] dealt mainly with the classical resonator having discrete mirrors

---

[9] The definition of power loss in reference [8] is actually the square root of our definition for κ. The factor of 2 discussed here has taken this discrepancy in the definition into account.

a few times smaller than the cavity length[10], the VCSEL structure is simply the opposite, with the mirrors usually a few times longer than the cavity! We can argue that the remaining factor-of-two discrepancy arises from the difference in the geometry of our resonators. Intuitively, it makes sense that a shorter resonator would have lower loss than the longer resonator that has the same sized mirrors. We thus have good confidence in the validity of our model.

V   Confirmation with experiment

Lastly, we would like to confirm the validity of our model with experimentally derived data. Shown in figure 6.22(a) is the sum of the calculated diffraction and tilt losses for two devices with diameters of $5\mu m$ and $10\mu m$. Experimentally, we derive the roundtrip optical loss in our devices using the slope efficiency under pulsed operation and obtain the roundtrip losses plotted in figure 6.22(b). Good qualitative agreement is shown between the calculation and measurements in the general trend with wavelength as well as the relative loss levels between the two sizes. We thus believe that our model is well grounded and is useful towards predicting losses for other tunable VCSEL structures, perhaps in other wavelength regime or with other tilt features or characteristics in their construction.

---

[10] In [8], the requirement that $\dfrac{a^2}{b\lambda} << \left(\dfrac{b}{a}\right)^2$ has to be met for an integral equation in the analysis to be valid. That's why their results are confined to the more classical resonator dimensions.
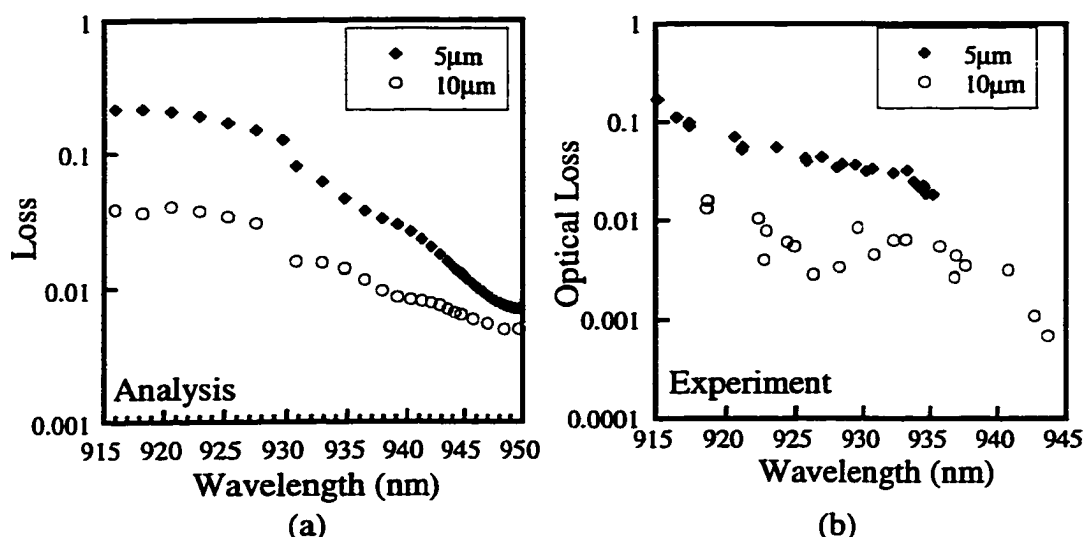
167

Figure 6.22 Comparison between our analytical results and experimentally-derived roundtrip losses in our tunable VCSELs
Roundtrip optical losses include tilt of the mirror: (a) Results from our calculations and (b) experimentally derived data.

VI   Summary and implications

It is important to realize that the pains in developing the mathematical methods discussed in this chapter are for answering the three main, frequently-asked questions mentioned at the beginning of this chapter: At what cost is tunability, how does optical loss vary across a device's tuning range, and finally, at what cost is the tilt in one mirror?   Each of these questions was answered in turn throughout this chapter by breaking up the components in a VCSEL cavity and solving the steady state roundtrip cavity eigenvalue problem with the boundary conditions set by the aperture.   We discover that compared to a regular VCSEL, a tunable VCSEL's air gap causes significant amounts of extra optical loss for small devices ($\sim 5\mu m$).   Fortunately, a larger aperture device ($\sim 10\mu m$) experiences only marginally more loss than a regular VCSEL.   We've also found that, as expected, index-guided tunable VCSELs suffer

168

less extra loss than their counterparts with opaque apertures when compared to the regular non-tunable VCSELs.

In section III D, the wavelength dependence of the roundtrip optical loss for the tunable VCSEL with two different kinds of apertures was discussed. The first is opaque while the other is a phase aperture. Parallel mirrors have been assumed. After taking due account of the non-uniform reflectance of the two mirrors across the tuning range, the wavelength-dependent diffraction loss is found. Also as expected, the shape of this loss is in the form of a "U," with the minimum loss occurring at the center wavelength, i.e. the wavelength at which the two DBRs have their peak reflectance. Monotonic increase of this loss away from the center wavelength is due mainly to the spread of the optical mode's spectrum, i.e. in k-space, overlapping with the "dips" defining the main reflectivity lobe of each DBR (see figure 2.2).

In section IV, we dealt with the component in the modal loss caused by the tilt in the cantilever head of the VCSEL. Remarkably, very little change needs to be introduced into our model to account for the tilt in one DBR mirror. We find that the amount of tilt loss is dramatically different for 5μm and 10μm wide devices. This difference is attributed to the fractional amount of tilt present relative to the optical mode's divergence angle. Finally, we have been able to confirm the validity of our calculations by comparing our results against Fox and Li's analysis as well as our own measured data.

Now we can finally revisit the two devices whose performance detailed back in chapter 4. Remember that the smaller device did not "wrap around" its tuning range like its larger counterpart? We can understand now that this would be the case

because the diffraction loss associated with such a small aperture simply cannot be overcome by the available gain on the red end! The device with the larger aperture also has a longer cantilever beam (150μm long versus 100μm for the smaller device). This effectively reduces the maximum tilt in the head to only about two thirds of the 0.4 degree value we saw back in figure 6.14.

Although instrumental for our understanding of the limitations present in our current VCSEL structure, the power of these analyses lies in their potential use to determine optical loss in other vertical cavity structures, tunable or otherwise. Would it help to use dielectric mirrors? What about mirrors from other wavelength regimes? Tilt doesn't seem to matter for devices with small apertures when the lever arm is at least 100μm long. What if we are restricted for some reason to have shorter lever arms? All these are interesting questions that can be answered qualitatively with the analyses discussed in this chapter. It would be a serious and unwarranted digression to delve into those questions as there is no way to confirm the calculated results here. We shall leave the answers to those questions to the curious reader in the future.

VII   References

[1]   E. Hecht and A. Zajac, *Optics*, Second ed. Menlo Park: Addison-Wesley, 1987.

[2]   J. W. Goodman, *Introduction to Fourier Optics*. San Francisco: McGraw-Hill, 1968.

[3]   D. I. Babic, Y. Chung, N. Dagli, and J. E. Bowers, "Modal Reflection of Quarter-Wave Mirrors in Vertical-Cavity Lasers," *IEEE Journal of Quantum Electronics*, vol. 29, pp. 1950-1962, 1993.

[4]   A. Yariv and P. Yeh, *Optical Waves in Crystals*. New York: John Wiley & Sons, 1984.

[5]   A. Thelen, *Design of Optical Interference Coatings*. San Francisco: McGraw-Hill Book Company, 1989.

[6]   D. G. Deppe, D. L. Huffaker, O. Tchang-Hun, D. Hongyu, and D. Qing, "Low-threshold vertical-cavity surface-emitting lasers based on oxide-confinement and high contrast distributed Bragg reflectors," *IEEE Journal of Selected Topics in Quantum Electronics*, vol. 3, pp. 893-904, 1997.

[7]   M. H. MacDougal, J. Geske, L. Chao-Kun, A. E. Bond, and P. D. Dapkus, "Low resistance intracavity-contacted oxide-aperture VCSELs," *IEEE Photonics Technology Letters*, vol. 10, pp. 9-11, 1998.

[8]   A. G. Fox and T. Li, "Modes in a Maser Interferometer with Curved and Tilted Mirrors," *Proceedings of the IEEE*, vol. 51, pp. 80-89, 1963.

[9]   D. I. Babic, R. J. Ram, and J. E. Bowers, "Scaling laws fro gain-guided vertical cavity lasers with distributed Bragg reflectors," *Applied Physics Letters*, vol. 64, pp. 1762-1764, 1994.

[10]   E. R. Hegblom, D. I. Babic, B. J. Thibeault, and L. A. Coldren, "Estimation of scattering losses in dielectrically apertured vertical cavity lasers," *Applied Physics letters*, vol. 68, pp. 1757-1759, 1996.

[11]   E. R. Hegblom, D. I. Babic, B. J. Thibeault, and L. A. Coldren, "Scattering losses from dielectric apertures in vertical-cavity lasers," *IEEE Journal of selected topics in quantum electronics*, vol. 3, pp. 379-389, 1997.

Conclusion

Micromechanical tunable VCSELs can have a large impact in providing continuous tuning across a wide wavelength range at competitive costs for optical and data communications. Only a single tuning contact is necessary, allowing the tuning scheme to be extremely simple. Furthermore, the use of a springboard-like mechanical structure has allowed complete laser tuning across 31.6nm, a record to date, in only 28V. Device processing is remarkably simple so that it could be manufactured at potentially low cost. Moreover, the two-dimensional geometry of the VCSEL renders it extremely easy and inexpensive to test and characterize in batches.

Among the topics of discussion in this thesis have been the design, performance, and analysis of these tunable VCSELs. Chapter two was mainly concerned with the design of the structure. Using simple plane wave analysis, the tradeoff between tuning range and practical fabrication yield issues was given. In addition, we have found that employing one dielectric mirror in the tunable VCSEL is not advantageous in enhancing the tuning range, as it is limited by the other mirror with the narrower reflectivity bandwidth. The one-third limit in the displacement of the cantilever head was readily derived. We can now understand that there is an inherent limit to the tuning range using an electrostatic-mechanical tuning scheme

such as ours. A larger initial air gap allows for larger displacement, but then the cavity length would be longer, narrowing the free spectral range across which continuous tuning can be achieved.

Fabrication of our tunable VCSELs is fairly straightforward. Important process steps were summarized in chapter three. Ingenuity in the use of in-situ etch monitors and mask designs has helped make device processing remarkably simple. The performance of some tunable VCSELs was highlighted in chapter four. Continuous tuning over 20nm was achieved in 17V with a 5μm wide tunable VCSEL that has a 3μm wide by 100μm long cantilever beam under CW operation at room temperature. A multimode, 10μm wide device with a 5μm wide by 150μm long cantilever demonstrated 31.6nm of continuous tuning under CW operation at room temperature. Performance figures of merit for these devices across their respective tuning ranges show that uniform light-current characteristics require careful design in the DBRs and the gain spectrum of the structure. Our devices have also shown that the tunable VCSEL can be less temperature sensitive than regular VCSELs, depending on the amount of internal field seen by the air gap. We have also actively stabilized the emission wavelength of a tunable VCSEL to within one nanometer over a broad range of operation temperature.

The more involved mechanical and optical analyses have been detailed in chapters five and six, respectively. Analytic design rules arising from first principles in solid mechanics guide us in the determination of the movable cantilever's geometry to meet tuning voltage specifications. Detailed numerical analysis shows that our tunable cantilever beams' electrostatic behavior agrees very well with calculations

using a distributed load analysis. Fringing field considerations only give a maximum correction factor of 4% in the tuning bias compared to the analysis that neglect these fringing electric fields. Chapter six sought to assess the penalty our devices suffer by being tunable as well as having a cavity with two unparallel mirrors. We found that larger spatial modes have smaller acceptance angles and therefore are more sensitive to the tilt in the top mirror. It was found that small devices ($\sim$5μm) pay a high price to be tunable while larger devices ($\sim$10μm) experience losses from the tilted top DBR. We realize that the smaller device in chapter four did not "wrap around" its tuning range because the diffraction loss associated with such a small aperture simply cannot be overcome by the available gain on the red end of its tuning spectrum. In addition, due to the difference in their arm lengths, the larger device in chapter four only experiences about two-thirds of the maximum tilt seen by the smaller device. The pieces of the puzzle that crop up during the measurement and characterization of our devices finally fall into place to help us understand and explain the respective demonstrated tuning ranges.

It is important to bear in mind that the work described in this thesis has only been part of the beginning of an exciting journey to make the tunable micromechanical VCSELs practicable enough to have an impact in our everyday lives. Much more thorough work is necessary to refine the design and resolve reliability issues. Among the first items on one's wish list would be a wider tuning range. Uniform performance characteristics across such a wide tuning range would also be extremely desirable. Necessary questions to be further addressed are: the electrical and mechanical cross-talk between the modulation of the cantilever beam and the laser itself, reliability of

the cantilever beam after many tuning operations over the lifetime of the device, and transverse mode suppression issues, just to name a few.

At this point in time, I can speculate on two of the issues above: cross-talk and increases in the tuning range. The electrical-mechanical cross-talk may not be a severe problem as the resonant frequencies of the mechanical structure and the laser are a few orders of magnitude apart.[1] Wider tuning ranges are achievable if the air gap can be used more efficiently. If the cantilever head can be displaced across the entire air gap, the tuning range is not compromised through a reduction of the free spectral range as it is in our case now. However, it would be necessary to work around the one-third rule. One simple tuning scheme that could work around this rule is to use charge (Q) instead of voltage (V) as the independent input variable. Referring to our derivation of the "one-third" rule back in chapter two from equations (2.11) through (2.16), it is easy to understand the difference of having Q as the independent variable by the simple equations below:

$$E_{cap} = \frac{CV^2}{2} = \frac{Q^2}{2C} = \frac{Q^2}{2} \frac{d_0 - z}{\varepsilon A} ; \qquad (7.1)$$

C = εA/z has been assumed for a parallel plate capacitor. Taking the derivative of (7.1) gives us the downward electrostatic force, as before in (2.11) and (2.12). This will give us the following:

$$F_\downarrow = \frac{\partial}{\partial z}(E_{cap}) = \frac{Q^2}{2\varepsilon A} . \qquad (7.2)$$

---

[1] The mechanical resonance in the shortest cantilever beams described in this thesis is on the order of 100kHz, while the laser's relaxation-oscillation is at least a few GHz. For data on the mechanical resonance of similar GaAs beams, the reader is referred to [1]. Incidentally, reducing a beam's air drag can also enhance the resonant frequencies of these microstructures, but that means some sort of vacuum packaging. The interested reader is referred to [2].

175

Notice that $F_\perp$ is no longer a function of z. Therefore, when we plot $F_\perp$ and the

restoring force, $F_\uparrow$ versus the displacement z in this case, as in figure 2.16, we would
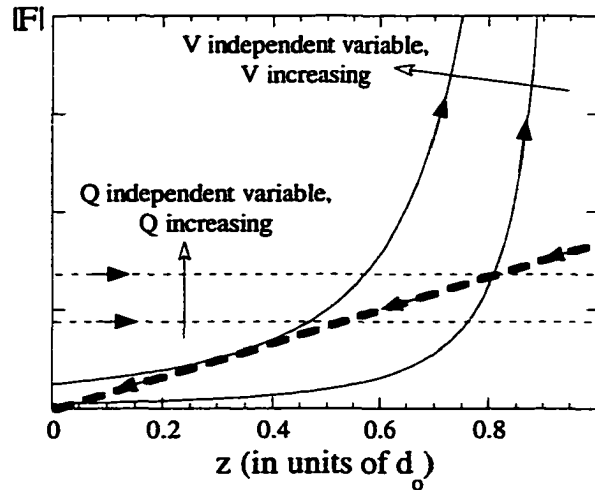
get two straight lines. See figure 7.1 below.

Figure 7.1 $F_\uparrow$ and $F_\perp$ **plotted against the displacement variable z**

This plot explains why the one-third rule goes away when we make Q the independent input variable (instead of V). The magnitude of the forces is plotted as a function of displacement z from the equilibrium point of the cantilever. Shown in the thick dashed line is the mechanical restoring force. The left pointing arrows on the line indicate that this force tends to return the cantilever head towards its equilibrium position, i.e. z=0. The thin solid lines indicate the magnitude of the downward electrostatic forces acting on the cantilever in the case of having the applied voltage as the independent variable. The right pointing arrows associated with these lines simply remind us that this force tend to act on the cantilever head to increase displacement z. Now, when charge is the independent input variable, the downward force takes the form of (7.2). Plotting (7.2) for two different values of Q gives us the thin dashed curves, also pointing to the right. Notice that in this case, a stable solution always exists through all valid values of z!

The electrostatic force is horizontal while the spring force has a slope equal to

the spring constant and an intercept at the origin. There is only one stable solution for

any Q. Thus the entire air gap is accessible to the cantilever head! Of course, nothing

would come for free. The tradeoff in having the entire air gap at our disposal is the

more-involved implementation. One would need a coulomb counter (see [3], for

example) and the necessary feedback circuits to control the amount of charge on the

tuning contact.

The discussion above merely touches the tip of a series of possible solutions to make the micromechanical tunable VCSEL a practical reality. I sincerely hope and believe that the 31.6nm of tuning range reported in these pages can be exceeded by factors of two with ease in the near future. Ingenious design and optimization would realize uniform performance characteristics across wide tuning ranges. Further understanding of other micromechanical structures can lead to less tilt loss and tunability penalty compared to the losses in a regular VCSEL.

References

[1]   E. C. Vail, "Micromechanical Tunable Vertical Cavity Surface Emitting Lasers," in *Electrical Engineering*. Stanford, CA, USA: Stanford University, 1997, pp. 177.

[2]   F. R. Blom, S. Bouwstra, M. Elwenspoek, and J. H. J. Fluitman, "Dependence of the quality factor of micromachined silicon beam resonators on pressure and geometry," *Journal of Vacuum Science and Technology B*, vol. 10, pp. 19-26, 1992.

[3]   P. Horowitz and W. Hill, *The Art of Electronics*. New York: Cambridge University Press, 1980.

IMAGE EVALUATION
TEST TARGET (QA-3)

150mm

6"
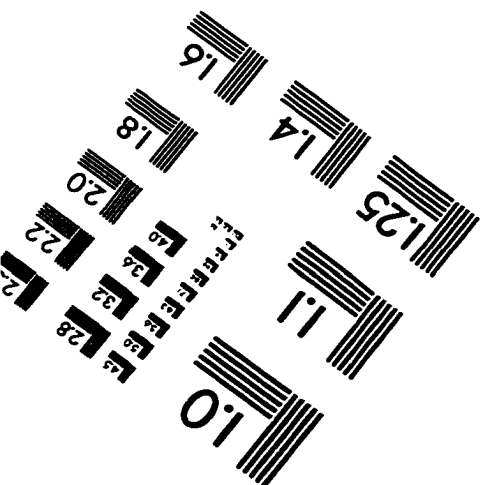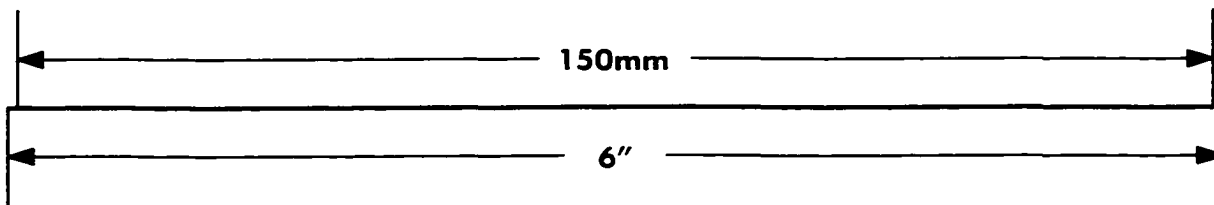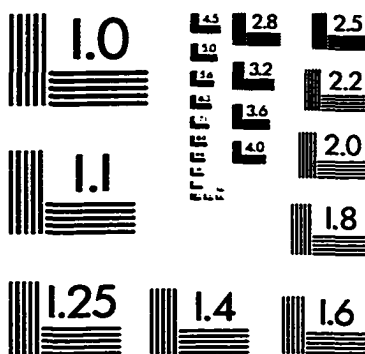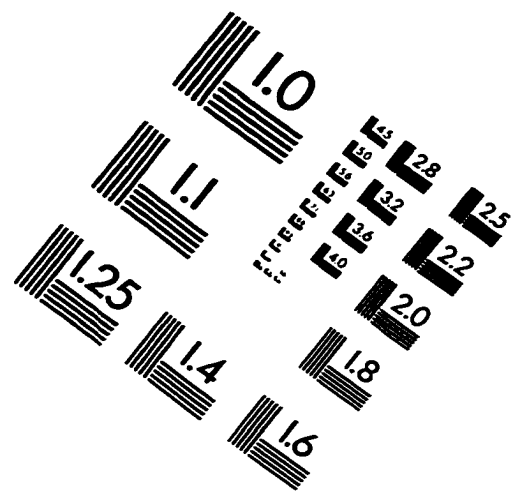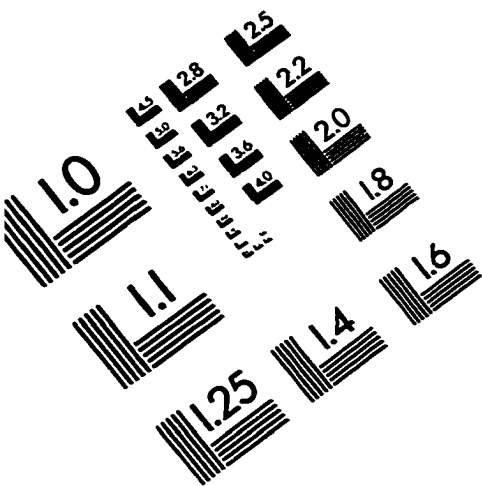
APPLIED IMAGE . Inc
1653 East Main Street
Rochester, NY 14609 USA
Phone: 716/482-0300
Fax: 716/288-5989